



TECHNISCHE
UNIVERSITÄT
WIEN

DISSERTATION

**Frequency measurements
testing Newton's Gravity Law
with the Rabi- q BOUNCE experiment**

Ausgeführt zum Zwecke der Erlangung des akademischen Grades eines
Doktors der Technischen Wissenschaften unter der Leitung von

Univ. Prof. Dr. Hartmut Abele

E141 - Atominstitut

eingereicht an der Technischen Universität Wien
Fakultät für Physik

von

Dipl.-Ing. Gunther Cronenberg

Matrikelnummer 0225298

Alpenlandstraße 2, A-2380 Perchtoldsdorf

Wien, am 16. Dezember 2015

Zusammenfassung

Im Rahmen dieser Arbeit wurde ein Aufbau zur Gravitations-Resonanz-Spektroskopie realisiert, um Newtons Gravitationsgesetz bei kleinen Abständen zu überprüfen. Mit dem Aufbau können gravitativ gebundene, diskrete Zustände ultrakalter Neutronen studiert werden, die sich oberhalb eines Neutronenspiegels im Gravitationsfeld der Erde ausbilden. Die Zustände haben Eigenenergien, welche im pico-eV Bereich liegen und nur von der lokalen Erdbeschleunigung, der Neutronenmasse sowie der Planckschen Konstante abhängig sind. Gravitations-Resonanz-Spektroskopie ist eine neue Form der Spektroskopie, welche keine elektromagnetische Wechselwirkungen verwendet. Der neue Aufbau, angepasst an die Gravitation, basiert auf Rabis Methode zur Messung von Energiedifferenzen einzelner Quantenzustände. In dieser Arbeit wurden resonante Übergänge zwischen den Zuständen durch kontrollierte mechanische Oszillationen der Randbedingung mit variabler Stärke und Frequenz induziert.

Der Aufbau besteht erstmals aus drei verschiedenen Regionen, wobei in der Wechselwirkungsregion auf einen oberen Spiegel verzichtet werden konnte, was ungestörte und damit systematisch reinere Zustände ermöglicht. Gleichzeitig konnte die Wechselwirkungszeit deutlich vergrößert werden, was sich in schmälere Übergängen manifestiert.

Mit diesem Aufbau konnte der Übergang zwischen dem Grund- und dem dritten Zustand sowie erstmals zwischen dem Grund- und dem vierten Zustand angeregt und mit einer Energiedifferenz $\Delta E_{13} = h \times (464.1_{-1.2}^{+1.1} \text{ Hz})$ bzw. $\Delta E_{14} = h \times (648.8_{-1.6}^{+1.5} \text{ Hz})$ beobachtet werden. Zum ersten Mal konnte auch die ursprüngliche Zustandsbesetzung bei Resonanz wieder hergestellt werden, nämlich bei dem Übergang zwischen Grund- und drittem Zustand. Dabei wurde keine Dekohärenz der Zustände beobachtet.

Da die Wellenfunktionen als Lösungen der Schrödingergleichung für das lineare Gravitationspotential eine vertikale Ausdehnung von einigen dutzend Mikrometern haben, ist das System äußerst sensitiv auf Abweichungen von Newtons Gravitationsgesetz bei diesen Längenskalen. Zahlreiche theoretische Modelle, welche das Standard Modell der Teilchenphysik erweitern sollen, sowie Dunkle Materie und Dunkle Energie erklären wollen, sagen solche Abweichungen vorher. Mit dem hier präsentierten Aufbau konnten Grenzen für die Existenz eines neuen Skalarfeldes abgeleitet werden. Dieses sogenannte Chamäleon-Feld wurde eingeführt, um Dunkle Energie zu erklären. Seine Existenz würde die Energieniveaus der Gravitationszustände und damit der Übergangsfrequenzen in bestimmter Weise beeinflussen. Des Weiteren wurden generische Abweichungen untersucht, welche durch Kräfte mit einer Yukawa-artigen Wechselwirkung herrühren. Da neue Kräfte sehr wahrscheinlich das Einsteinsche Äquivalenzprinzip verletzen, wird das Experiment auch als

Test des universellen freien Falls betrachtet.

Abstract

In this thesis a new experiment for Gravity Resonance Spectroscopy is presented to study Newton's inverse square law of gravitation at short distances. It allows to observe the gravitationally bound discrete states of ultra-cold neutrons which they form when confined above a mirror in the gravity potential of the Earth. The eigen energies which are in the pico-eV range, are functions of the local acceleration, the neutron mass and the Planck's constant. Gravity Resonance Spectroscopy is a new form of spectroscopy which does not use electromagnetic interaction. The new setup, adapted for gravitation, is based on Rabi's method gives access to the energy differences of quantum states by measuring the transition frequencies upon which resonant excitation occurs. In this case, the excitations are driven by controlled mechanical oscillations of the boundary conditions with variable strength and frequency imposed by the confining neutron mirror.

For the first time the Rabi-like setup features three distinct regions without an additional mirror on top in the interaction region, allowing for an undisturbed and hence systematically well-defined wave function. Additionally the interaction time could be significantly increased which leads to narrower transitions. The experimental techniques for the new kind of setup with increased complexity were refined and implemented. These include alignment measurements and assessment as well as oscillation control and confinement. With this setup, transitions between the ground and the third gravitational state and for the first time between the ground and the fourth state were excited and observed with an energy difference of $\Delta E_{13} = h \times (464.1_{-1.2}^{+1.1} \text{ Hz})$ and $\Delta E_{14} = h \times (648.8_{-1.6}^{+1.5} \text{ Hz})$. Also for the first time, a full state reversal could be induced and observed namely for the transition between the ground and third state. No decoherence of the states was observed.

The wave functions have a vertical size of a few dozens of microns, and the system is sensitive to any deviations from Newton's inverse square law at these distances. Sources of such hypothetical deviations are an active field of research as they might give access to new extensions of the standard model of particle physics and explain the matter and energy content of the universe. With this setup, limits on chameleon fields, a new scalar field, which is considered as an attractive dark energy candidate, could be derived. Its existence would lead to energy shifts of the gravitational states which have a clear signature in the transition frequencies. Also, generic deviations in form of forces with a Yukawa-like interaction potential are studied. As any new force is likely to violate the Einstein equivalence principle, the experiment can be interpreted as a universally free-fall test.

Contents

Zusammenfassung	i
Abstract	iii
Contents	v
1 Gravity Experiments	1
1.1 Overview of ways to probe theories on gravitation	2
1.2 Quantum objects in the gravity field	3
1.3 Gravity resonance spectroscopy	4
2 Gravity tests using Resonance Spectroscopy	7
2.1 Ultra-cold neutrons	7
2.2 The Quantum bouncer	8
2.3 Gravity resonance spectroscopy with a full Rabi-type setup	10
2.3.1 State preparation	11
2.3.2 State analysis and detection	12
2.3.3 State excitation	13
3 Experimental realisation of Rabi-type GRS	17
3.1 Technical realisation and its systematic investigations	17
3.1.1 Neutrons time-of-flight	17
3.1.2 State preparation and analysis with rough boundary conditions	21
3.1.3 Setup alignment	27
3.1.4 Induced state excitation with mechanical oscillations	30
3.1.5 Neutron detection	35
3.1.6 Vacuum chamber	40
3.1.7 Magnetic shielding	41
3.1.8 External systematics	42
3.1.9 Null rate stability	45
4 Data analysis	47
4.1 Fit function and its parameters	47
4.2 Comparison of different fit hypotheses	49
4.3 Conclusions	51

5	GRS Results	53
5.1	Determination of the local acceleration	53
5.2	Einstein equivalence principle	53
5.2.1	General relativity and the Einstein equivalence principle	54
5.2.2	Quantum mechanical tests of EEP	54
5.2.3	The quantum bouncer and universal free fall	54
5.2.4	Limit on the Eötvösh parameter	55
5.2.5	Determining the neutrons mass	56
5.3	Fifth force constraints	57
5.4	Experimental constraints on chameleon fields	59
6	Summary & Outlook	65
A	Airy functions, their primitives and applications as wave functions	69
A.1	Airy functions	69
A.2	Overlap of Airy functions	70
A.3	The free wave function	70
A.4	The wave function with upper mirror	70
A.5	Overlap with partial derivative	72
A.6	Overlap with position operator	72
B	Characterisation of polarisation foil	73
B.1	Motivation	73
B.2	Characterisation of a polariser	73
B.2.1	Functioning of the polariser	73
B.2.2	Experimental setup	74
B.2.3	Data evaluation	74
C	Glossary	79
	Bibliography	81
	List of Figures	88
	List of Tables	90

Chapter 1

Gravity Experiments

Gravitation is one of the four known fundamental forces. While the other three forces, namely the electromagnetic, the weak and the strong force are described within the standard model of particle physics, gravitation still has a special part in our understanding of nature. Its description, general relativity (GR), is fundamentally different in its form from the standard model (SM).

The Einstein field equations, celebrating 100 years since introduction are at the heart of GR [Einstein, 1915]:

$$G^{\alpha\beta} + \Lambda g^{\alpha\beta} = \frac{8\pi G}{c^4} T^{\alpha\beta}, \quad (1.1)$$

where $G^{\alpha\beta}$ is the Einstein tensor, $T^{\alpha\beta}$ is the stress-energy tensor. Λ , the cosmological constant, originally introduced to allow for a static universe, is nowadays used to implement a mechanism to allow for an accelerated expanding universe caused by dark energy.

General relativity has passed numerous experimental tests in its 100 year history and is also at the heart of our modern technology, for example in global navigation satellite systems. However, from a conceptual point there is a strong desire to extend the theory and to unify GR with the standard model. There are numerous theoretical models providing such extensions but their construction proves to be quite tricky because GR is a geometric description while the other forces are described by gauge theories. Additionally, the gravitational force is many orders of magnitude weaker than the electromagnetic force. This so-called hierarchy problem should be addressed by a more general theory.

Furthermore, an extension seems to be required by empirical observations which pose some puzzling unanswered questions. The rotation curves of various galaxies show that the rotational velocities are rather linear and do not decrease with the radius as one might expect from general relativity. From the virial theorem this indicates a mass increase with radius $M \propto r$. The additional mass, which is currently unidentified, was named dark matter as it seems not to interact with the other three known forces, thus being invisible and *dark* [Zwicky, 1933, Trimble, 1987, Iocco et al., 2015].

At the same time we observe an acceleratingly expanding universe which leads us to believe that there is an additional pressure term in equation 1.1 responsible for this

behaviour. It is normally absorbed in the cosmological constant, its nature is also unknown and an intensive field of research. From the latest satellite data the energy-mass density in the universe is attributed to 26.8% dark matter and to 68.3% dark energy which supports a flat universe [Planck Collaboration, 2014].

1.1 Overview of ways to probe theories on gravitation

As gravitation is of great interest, there is a seemingly endless number of experiments studying gravitation and its effects over a huge length scale from cosmological distances to the quantum regime. In the following is a non-exhaustive list of experiments. Starting at the cosmological scale, there are observations of the cosmic microwave background from the satellite Planck and from ground BICEP-2 [BICEP2/Keck and Planck Collaborations, 2015], which look back to the recombination epoch when the universe became transparent. They study GR indirectly by looking at the dark matter and dark energy content.

The Lunar Laser Ranging (LLR) experiment contributes at an intermediate scale [Bender et al., 1973]. Corner-cube mirrors left at the moon during the Apollo and Luna moon missions reflect pulsed monochromatic laser light back to Earth. In the beginning only few photons were received from each shot. Today however, with improved laser power and experimental techniques, many thousand returning photons are detected today despite the ageing of the mirrors. This allows to track the distance to the moon governed by gravitational effects from Earth and the sun and probe for any additional forces [Williams et al., 2012].

One example of the many space based experiments is the evolved Laser Interferometry Space Antenna (eLISA) planned to start in 15 years. Three satellites will be searching for gravitational waves below 1 Hz while orbiting the sun. In a V-constellation, the 1×10^6 km distances of the two interferometer arms will be monitored by laser beams [Amaro-Seoane et al., 2012]. The ground based Laser Interferometer Gravitational Wave Observatory (LIGO) was built to measure gravitational waves at different locations. It is currently being updated to Advanced LIGO for an improved sensitivity at lower frequencies down to 10 Hz, which allows a longer observation time of certain sources. Two laser arms oriented normal to each other measure a four kilometre long cavity. Incoming gravitational waves from sources like coalescing neutron stars binaries or fast-spinning neutron stars are expected to be detected [Harry, 2010].

The most precise measurements of the weak equivalence principle are pendulum experiments [Schlamminger et al., 2008]. This field was pioneered by Eötvös who determined the acceleration of different materials with a torsion pendulum. The two test masses were mounted on the ends of a rod, which was balanced on a wire. This method allows to measure the so-called Eötvös parameter η . The experiments were again re-analysed by Dicke [Bod et al., 1991]. Nowadays the Eöt-Wash group is known for using the method with greatly improved techniques to test additional theories and to impose limits on η . Combining their data with the one obtained from LLR yield even more stringent limits [Adelberger et al., 1990].

1.2 Quantum objects in the gravity field

On even smaller scale, quantum mechanics is normally needed to describe a system which is often dominated by the electroweak or strong force. In such experiments, gravitation can be and is neglected for the description of small systems. In the following are a few experiments listed non-exhaustively which are designed in such a way that gravitational effects become visible. This allows to study gravitation at laboratory scales. Also the discrepancy between gravitation as a classical theory and quantum mechanics comes into play. In GR, as a geometrical theory, the kinematics are independent of a particles mass. The geometrical nature is the basis for Einstein Equivalence Principle. However in quantum mechanics, the inertial and gravitational masses enter on different footing [Greenberger, 1968]. A more thorough discussion follows in section 5.2.

The COW experiment [Colella et al., 1975] measured the gravitational phase shift of a neutron in an interferometric setup. A neutron wave function is split on a silicon plate, then deflected at a subsequent plate and finally combined again by a third plate (see figure 1.1). The output modes show the interfered signal from the two parts. Any phase difference that is accumulated by the wave function in the two separate ways results in intensity being moved from one output mode to the other. By tilting the silicon interferometer one path lays higher in the gravitational potential than the other, which leads to a gravitational phase shift β proportional to wave length, local acceleration and neutron mass: $\beta \propto \lambda g \hbar^{-2} m_N^2$ (as well as known and unknown systematic effects like the phase shift due to bending of the material). This shows that the quantum particle behaves indeed as expected in the gravity field. The same method can be used in atomic interferometers, which are implemented in various laboratories [Peters et al., 1999, Chiow et al., 2011, Hamilton et al., 2015a]. There, instead of neutrons, laser-cooled atomic ensembles are separated and combined again in a gravitational field. The separation, deflection and combination are here realised by laser pulses and the population of the output modes is determined by fluorescence. A modification of the scheme is an implementation where such an atom interferometer setup is dropped in a drop tower [Schlippert et al., 2014]. During the free fall two atom clouds of different composition are each interfered simultaneously and the weak equivalence principle (WEP) can be tested.

Very slow free-falling neutrons were used to test the WEP [Koester, 1976] (see figure 1.1 right). The kinetic energy gain from the fall needed to penetrate liquid lead and bismuth was measured and their scattering length derived. This method was compared to scattering-length measurements independent of gravity. While the first method includes the gravitational mass, the other results were only dependent on the inertial mass.

More recently, ultra-cold neutrons were used to study the weak equivalence principle [Frank et al., 2009]. Monochromatic neutrons, produced by a spectrometer, fell down in the gravity potential and passed subsequently a rotating grating. The grating decreased their kinetic energy by a quantised amount depending on the diffraction order. Afterwards the neutrons encountered an energy selector, which accepted the same energy as the initial spectrometer. Neutrons could only pass the experiment when the kinetic energy gain from the fall compensated the energy loss of the grating. To fulfil this condition, the vertical position of the final spectrometer could be changed as well as the rotation frequency of the grating. While the energy gain from the classical fall is dependent on the gravitational mass, the energy loss at the grating is a function of the

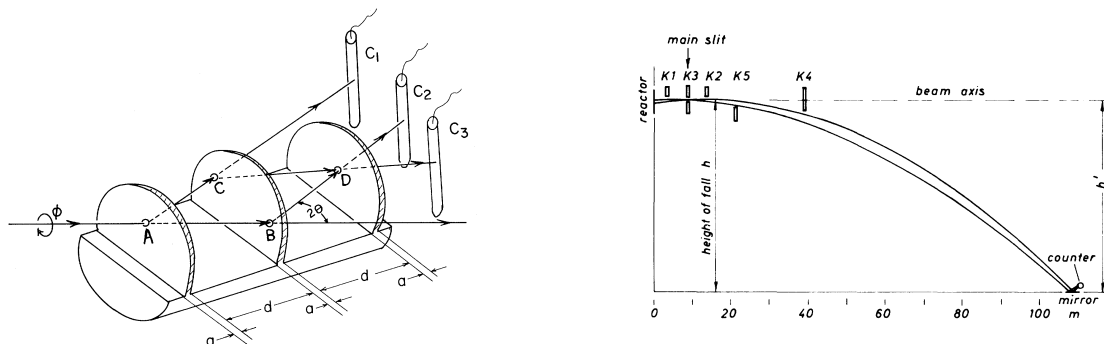


Figure 1.1: *Left*: The COW interferometer cut out of a Si mono-crystal. The neutron wave function is split by the first plate, deflected by the second and combined at the third plate. After the interferometer, the two output modes detected at C_2 and C_3 show shifting intensities dependent on the phase shift picked up in the interferometer. By tilting the interferometer the two paths are at different heights in the gravity potential. The picture was taken from [Colella et al., 1975]. *Right*: WEP test with cold neutrons. If the velocity gain of cold neutrons from a free fall is sufficiently high, they enter the liquid lead or bismuth. Otherwise they are reflected and detected by a detector. This allows a comparison of the gravitational mass with the inertial mass obtained by scattering length measurements. Picture taken from [Koester, 1976].

inertial mass which allows the experiment to compare them.

1.3 Gravity resonance spectroscopy

A different kind of experiment, namely gravity resonance spectroscopy (GRS) was realised and is studied in this work. An ultra-cold neutron is put above a neutron mirror, which is not penetrable by the neutron and thus poses a potential barrier. At the same time, the neutron is subject to the Earth's gravity field, which adds a potential, linearised in first order. Separating the degrees of freedom shows that in the vertical direction the neutron is confined by this potential. Thus, in the vertical direction, the neutron forms discrete eigen states. They have non-equidistant eigen energies, which follows from the linear potential form. Gravity resonance spectroscopy is a method that allows the measurement of energy differences between individual states. For this, resonant transitions between the states are induced. In the realised experiment, the transitions were driven by mechanical oscillations of the lower potential barrier posed by the neutron mirror. This means that the transition process for the resonances is devoid of any electro-magnetic interaction.

Gravity resonance spectroscopy was first introduced by [Jenke et al., 2011] in a very compact setup. In this work, the experiment was changed significantly by implementing a full Rabi-like setup, which allows a systematically clean state definition without dependence on experimental variables but only external, fundamental values.

The Rabi method is sensitive to energy difference of quantum states in the gravity potential of the Earth.

In this work the transition energy between the levels $|1\rangle$ and $|3\rangle$ was measured with a resolution of $\Delta E_{13} = 5 \times 10^{-15}$ eV and for $|1\rangle$ and $|4\rangle$ with $\Delta E_{14} = 7 \times 10^{-15}$ eV (1- σ standard deviation). This is several order of magnitude smaller than electromagnetically

bound states. In the long run a sensitivity of 5×10^{-21} eV can be expected [Abele et al., 2010].

While GRS also uses a quantum system within a gravitational field in the Newtonian limit, the experiment is unique in the way that gravitation enters the system. For other experiments, gravity becomes detectable through an induced phase shift or due to an energy gain of the quantum particle. Here however, the properties of the system themselves are defined by the gravitational field. As a consequence, gravitation is not the reason for one effect among others that leads to a measurable change in a physical quantity, but instead defines the whole system. Consequently, hypothetical modifications of general relativity do not just lead to deviations of one effect among many, but to be the main effect that can be studied in a systematically simpler form.

Gravity resonance spectroscopy has access to a number of parameters which allow to study gravity with different aspects. These experimental parameters are distance, mass, torsion, spin-coupling and the cosmological constant. A summary can be found in table 1.1. Focusing on the distance allows to test the validity of Newton's inverse square law at short distances. Most new physics models predict additional quantum fields which exhibit characteristic length dependencies of a Yukawa-like potential. The search for such models that modify the distance dependency is discussed in section 5.3. Next, both the inertial and the gravitational mass enter the description of our system, but on a different footing, which allows a test of the universal free fall, which is an important part of the Einstein equivalence principle which itself is a cornerstone of GR. Additionally, this test is not with a classical but a quantum system. In section 5.2 it will be discussed how GRS can contribute to this topic. Next, cosmological models with a screening mechanism, like the hypothetical chameleon field, can in principle be detected with GRS. Derived limits on this special scalar-field can be found in section 5.4. GRS can also search for modifications of the gravitational potential caused by (pseudo-)scalar couplings of neutrons with axion-like particles, which are dark matter candidates. This has been demonstrated in the previous iteration of the experiment [Jenke et al., 2014] and a technical analysis of a component, namely the spin-selector can be found in appendix B. For completeness, it should be mentioned that theoretically GRS has the means to search for torsion, a geometrical concept beyond GR, as it would result to a metric-spin coupling of the neutron. This has not been tested with this setup but further discussion can be found in [Abele et al., 2015].

distance	The validity of Newton's law at short distances will be studied in chapter 5. Models modifying the distance-dependence are discussed in section 5.3.
mass	The different footing of inertial and gravitational mass and the test of the universal free fall, part of the Einstein equivalence principle, will be studied in section 5.2.
cosmological constant	Models explaining the cosmological constant lead to effects detectable by GRS, see section 5.4.
spin-coupling	Extensions of GR could lead to an additional spin-coupling as is the case with dark matter candidates axion-like particles.
torsion	An additional torsion term in GR as described by Einstein-Cartan theory. A discussion is beyond the scope of this work.

Table 1.1: Accessible parameters of GRS that allow a deeper understanding of gravitation and theoretical extensions.

Chapter 2

Gravity tests using Resonance Spectroscopy

2.1 Ultra-cold neutrons

While there are many quantum objects to study gravity, the properties of ultra-cold neutrons make them ideal probes. Neutrons below a critical energy of about 300 neV (depending on the material) are reflected totally under any angle of incidence from most surfaces, they are then called ultra-cold neutrons (UCNs). This effect occurs when the wave length of the neutron is large enough to be coherently scattered by the nuclei of the bulk. The bulk can then be described by an effective Fermi potential V_F which was introduced by Fermi in 1936 [Golub et al., 1991]:

$$V_F = \frac{2\pi\hbar^2}{m_N}nb_c, \quad (2.1)$$

where m_N is the neutron mass, b_c the coherent scattering length of the material and n the material density. The neutron with a kinetic energy below V_F has an exponentially decaying probability of penetrating the bulk and is thus reflected from the surface. Typical values for the Fermi potential of different materials are $V_F \approx (50 \text{ to } 500) \text{ neV}$.

First ultra-cold neutrons were produced at Munich, Germany, and in Dubna, Russia, by [Steyerl, 1969, Lushchikov et al., 1969]. They can be produced in fission reactors like FRM-II in Munich and the high-flux reactor at the Institut Laue-Langevin (ILL) in Grenoble, which delivers the highest UCN density. At the ILL, UCNs are obtained through multiple steps: Neutrons from the reactor core are thermalised in a cold source filled with liquid deuterium. Afterwards they ascend in a neutron guide against gravity reducing their kinetic energy. By sending them through a Doppler-cooling turbine, developed by Steyerl [Steyerl, 1975] their velocity is reduced down to $\sim(5 \text{ to } 10) \text{ m s}^{-1}$. The ultra-cold neutrons are then fed through neutron guides and are available for experiments in a steady-flow mode. Alternative approaches use super-thermal neutron sources which employ down-scattering of cold neutrons in super-fluid helium He^4 [Zimmer et al., 2011] and spallation sources in combination with down-scattering in solid deuterium e.g. at the Paul Scherrer Institut [Anghel et al., 2009].

Ultra-cold neutrons found numerous applications in various experiments due to their properties. Currently the best limits on the neutrons electric dipole moment (nEDM)

velocity (5 to 10) m s ⁻¹	wave length (80 to 40) nm	energy (130 to 500) neV
magnetic moment -60.3 neV T ⁻¹	electr. polarisab. (11.6 ± 1.5) × 10 ⁻⁴ fm ³	magn. polarisab. (3.7 ± 2.0) × 10 ⁻⁴ fm ³

Table 2.1: Properties of UCNs (*upper*) and neutrons in general [Beringer et al., 2012] (*lower*).

were obtained with UCNs at the ILL [Baker et al., 2006, Pendlebury et al., 2015]. Ongoing experiments for the nEDM search are planned e.g. at the FRM-II in Munich, which houses a shielded room with the lowest magnetic field in the solar system [Altarev et al., 2015] and at the PSI in Villigen [Baker et al., 2011]. The lifetime of the neutron is also a very important question as it effects for example the nucleosynthesis. It can be measured by two methods. First, there is the in-flight mode where cold neutrons traverse a so-called decay volume and the decay products are measured relatively to the incoming flux. The most current in-beam experiment is [Nico et al., 2005]. The second method stores ultra-cold neutrons in a vessel for a varying time and afterwards the remaining neutrons are counted as a function of the storage time. This counting-the-survivors method was employed in the experiment MAMBO II at the ILL [Pichlmaier et al., 2010]. Both methods observe different neutron lifetimes, the resolution of this discrepancy is an ongoing task. Reviews of such experiments can be found in [Wietfeldt & Greene, 2011, Dubbers & Schmidt, 2011].

2.2 The Quantum bouncer

When studying massive quantum objects in the gravity field, one normally retreats to a Newtonian limit of the description, where velocities are smaller than the speed of light and space-time curvature is sufficiently small. This corresponds to $h_{\mu\nu}$, describing the deviation from the Minkowski metric, fulfilling $|h^{00}| \ll 1$. Gravity is then described by an external conservative field which satisfies¹ $\nabla^2\phi = 4\pi G\rho$ and is a limit of equation 1.1. As most quantum features like superposition or entanglement are rather fragile, the conditions of low or vanishing velocities, limited spatial regions need to be fulfilled during experiments. Furthermore, the back action of the test objects onto the space-time is neglected. In classical terms, only the passive mass of the object, sensing the field, is considered, its active mass, generating a field, is neglected.

The quantum object with mass m is attracted in the gravitational field of the Earth. For a laboratory application on the Earth's surface, far from the centre of mass, it is sufficient to linearise the gravity potential to

$$V(z) = m g z, \quad (2.2)$$

with the local acceleration $g = -\frac{GM_{\oplus}}{R_{\oplus}^2}$.

The description of a quantum particle above a barrier is called the "quantum bouncer" and was presented in the 1970ies [Langhoff, 1971, Gibbs, 1975]. The solution was adapted to ultra-cold neutrons in the gravity field by [Luschikov & Frank, 1978] who identified

¹From now on, in this work the notion of the potential $V(r)$ will be used instead of the field ϕ .

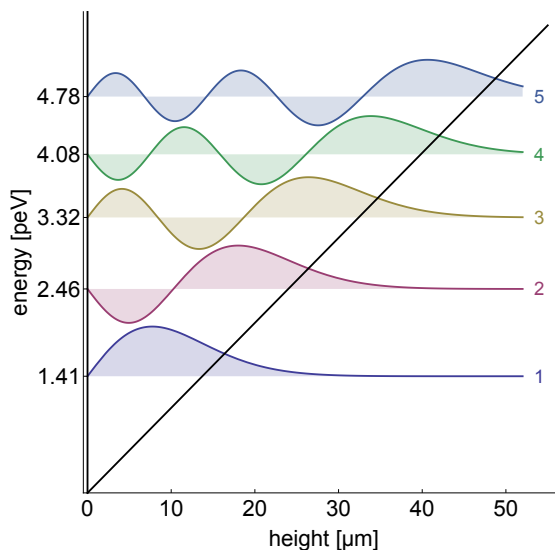


Figure 2.1: The first five eigen states and the corresponding eigen energies of an ultra-cold neutron in the gravity field above a neutron mirror placed below $z = 0$ which is shown as an infinite potential. The black lines show the potential.

the experimental advantages of UCNs (see section 2.1). The horizontal and vertical degrees of freedom can be separated and the one-dimensional Schrödinger equation for the vertical direction z reads:

$$\left(-\frac{\hbar^2}{2m_N} \frac{\partial^2}{\partial z^2} + m_N g z \right) \psi_n(z) = E_n \psi_n(z). \quad (2.3)$$

The equation is solved with the boundary conditions that the wave function has to vanish at the mirror and infinity $\psi_n(0) = \psi_n(\infty) = 0$. The neutron forms discrete eigenstates with non-equidistant energy-levels E_n . The eigenfunctions are described by Ai^2 functions (see figure 2.1 and appendix A):

$$\psi_n(z) = a_n \text{Ai} \left(\frac{z}{z_0} - \frac{E_n}{E_0} \right), \quad (2.4)$$

with the characteristic length z_0 and energy scale E_0 . Airy functions also appear in various fields like optics and electromagnetic tunnelling [Panda & Panda, 2001]. The potential with the first five eigenstates and their corresponding eigenenergies can be seen in figure 2.1. The quantum states of a neutron in the gravity field were first observed in 2002 at the ILL by our group [Nesvizhevsky et al., 2002] by measuring the transmission of neutrons behind a neutron mirror-absorber system in dependence of the slit height. The neutrons could not pass the setup if the slit height was smaller than $\approx 14 \mu\text{m}$, a slit size through which optical light can pass. The observed behaviour cannot be explained by a classical theory and is in agreement with the quantum mechanical picture.

²The Airy function is named after Sir George Biddell Airy, born in 1801 at Alnwick, Northumberland (North of England). Note that Airy also measured the local acceleration of the Earth in 1854 both on the surface and 1256 feet below ground in the pursuit to determine the mean density of the Earth [Airy, 1856].

The characteristic length z_0 and energy E_0 of the system are determined solely by the neutrons mass m_N , the local acceleration g and Planck's constant \hbar . Upon interaction, the time scale t_0 is also used:

$$z_0 = \sqrt[3]{\frac{\hbar^2}{2m_N^2g}} = 5.9 \text{ }\mu\text{m}, \quad (2.5)$$

$$E_0 = \sqrt[3]{\frac{\hbar^2 m_N g^2}{2}} = 0.6 \text{ peV}, \quad (2.6)$$

$$t_0 = \sqrt[3]{\frac{2\hbar}{m_N g^2}} = 1.1 \text{ ms}. \quad (2.7)$$

Lifting a neutron one meter against the Earth's gravity requires an energy of ~ 103 neV. For comparison, the length scale z_0 for an electron is $881 \text{ }\mu\text{m}$, the energy scale is 0.05 peV . Screening the electron from electromagnetic interaction at this level is futile. Another advantage of experiments with ultra-cold neutrons is their tiny polarisability compared to atoms ($\alpha_N = (11.6 \pm 1.5) \times 10^{-4} \text{ fm}^3$ and $\beta_N = (3.7 \pm 2.0) \times 10^{-4} \text{ fm}^3$) [Abele, 2008, Beringer et al., 2012].

2.3 Gravity resonance spectroscopy with a full Rabi-type setup

Resonance methods Resonance methods are very common and often relied upon in natural sciences, their success stems from the excellent precision they provide. Resonance methods are applied in nuclear magnetic resonance (NMR), laser spectroscopy, spin-echo and many more. With the use of resonance methods, time can be measured better than any other physical quantity, so that definitions of other quantities are derived from it.

This allows to measure energy with great precision by using resonance methods together with the connection: $E = \hbar\omega$. The high precision of time measurements leads to high quality energy determination. We implement Rabi's method which was introduced in [Rabi et al., 1939] and used originally to determine the magnetic moment of molecules.

Full Rabi-type setup Gravity resonance spectroscopy was first realised in a setup by [Jenke et al., 2011]. Extending the experiment from this simplified Rabi setup [Jenke et al., 2014] to a full three-part Rabi setup is a crucial step towards the planned implementation of Ramsey's scheme with gravitationally bound UCNs [Abele et al., 2010]. The setup presented here, consists of three distinct regions, similar to Rabi's original setup, shown in figure 2.2. In the first region, a quantum system is prepared in a defined eigen state. This state is excited subsequently into another state by a controlled interaction in the second region. The final region together with the following neutron detector perform a projection onto the analysing state. The observed neutron flux at the detector is a measure of successful state excitation. In contrast to other resonance experiments, the transition between states is not induced by electromagnetic interaction but by mechanical oscillations of the interaction region. The oscillations are controllable both in strength and frequency.

The following sub-chapters will cover the composites and the theoretical description of each region. The matrix formalism is used for the description as we treat finite, discrete

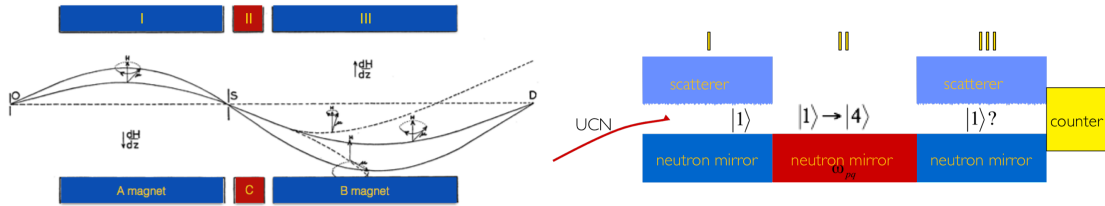


Figure 2.2: *Left*: The original Rabi setup with the three experimental regions I, II, III is shown. A molecular beam from left to right passes through a magnetic gradient field and is detected at the end. In between in the region marked in red with label C, an oscillating radio frequency field drives transitions between the states. (Picture adapted from [Rabi et al., 1939].) *Right*: The Rabi-like setup presented in this work also features three regions. Ultra-cold neutrons are first prepared, then excited (in the red region) and finally analysed, see text. In both experiments state selection for state preparation and analysis are marked in blue and the excitation region for state transition is marked in red.

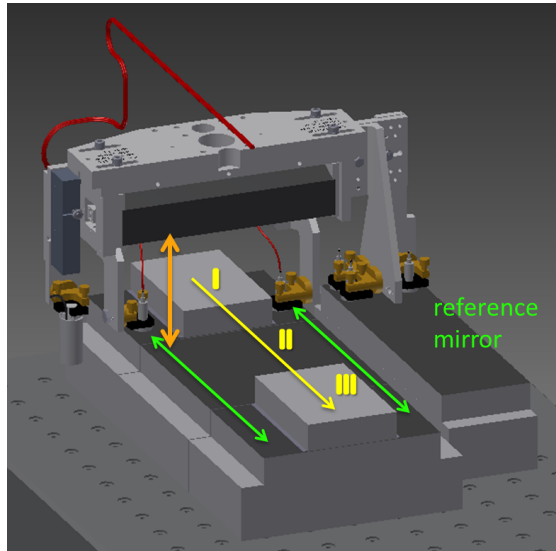


Figure 2.3: A technical drawing of the Rabi-like setup. In the middle the three regions I, II, III for preparation, excitation and analysing are shown and labelled in yellow. The construction above the mirrors holds capacitive sensors and is also part of the laser interferometer. The reference mirror is used by the capacitive sensors.

states. For the analysis of the experiment it is sufficient to consider only the first few eigen states, however the formalism allows to include up to any arbitrary state number. The propagation through the experiment is analysed step by step where the propagation matrix U_{ij} of that step gives the evolution of the wave function:

$$|\psi_i\rangle = U_{ij} |\psi_j\rangle \quad (2.8)$$

2.3.1 State preparation

In the first region the quantum system is prepared into a well defined state. With our realisation, we prepare the neutron in a lower state by suppressing higher states. This

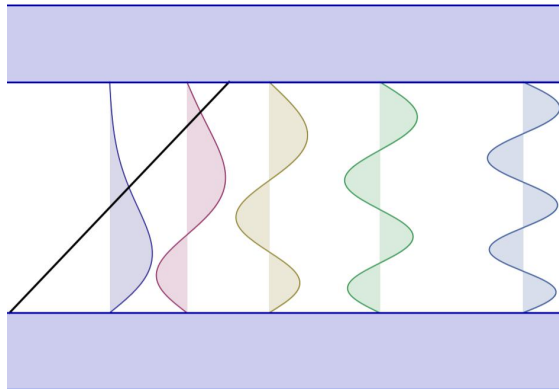


Figure 2.4: The wave functions of the first five eigen states between two neutron mirrors (in blue) are shown. The black line indicates the linearised gravity potential. The additional mirror on top squeezes the wave functions, especially the higher ones, leading to higher energies of the states.

is achieved by adding a rough neutron mirror on top of a flat one at a distance l . The wave function Ψ between the mirrors is described by a superposition of eigen states. The eigen functions ϕ_n are different from equation 2.4 due to the additional boundary condition $\phi_n(l) = 0$ that the upper mirror imposes and contain also Airy's Bi functions (see appendix A.4):

$$\phi_n(z) = a_n \text{Ai} \left(\frac{z}{z_0} - \frac{E_n}{E_0} \right) + b_n \text{Bi} \left(\frac{z}{z_0} - \frac{E_n}{E_0} \right). \quad (2.9)$$

The first five eigen functions are plotted in figure 2.4 between the two confining mirrors. The rough surface of the upper mirror leads to non-specular scattering, mixing the velocity components of the neutron, which allows the neutron to penetrate the mirror where it is absorbed. Upon interaction with the rough surface the neutron is effectively removed from the system. The rough surface adds a state-dependent loss mechanism which increases for higher states:

$$\Psi_{\text{I}} = \sum_n \gamma_n c_n \phi_n \quad (2.10)$$

It can be assumed that the loss γ_n is proportional to the overlap with the rough surface. However as the initial state population c_n entering the system is unknown, the state after region I can be described with the state population $c_{n\text{I}} = \gamma_n c_n$ as a starting point for the further description:

$$\Psi_{\text{I}} = \sum_n c_{n\text{I}} \phi_n \quad (2.11)$$

2.3.2 State analysis and detection

The third region is realised equivalently to the first region and again suppresses higher states. Together with the detector situated behind the third region they act as a projective measurement onto the lower states. The propagation matrix is the same as

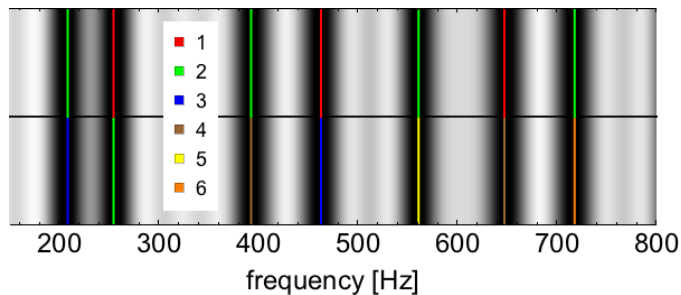


Figure 2.5: The transition probabilities encoded in black for the transitions $|1\rangle \leftrightarrow |2\rangle$ to $|2\rangle \leftrightarrow |6\rangle$ up to a frequency of 800 Hz are shown. The colours denote the states involved in the transition. For example the resonance $|2\rangle \leftrightarrow |3\rangle$ is indicated by the blue and green line at 208 Hz. The transition $|1\rangle \leftrightarrow |2\rangle$ is at 255 Hz. This work analyses the transitions $|1\rangle \leftrightarrow |3\rangle$ and $|1\rangle \leftrightarrow |4\rangle$ at 464 Hz and 649 Hz. The broadening $\Delta f = 1/t$ of the transitions stems from the interaction time $t = 20 \text{ cm}/(8 \text{ m s}^{-1})$. It is sufficiently smaller than the frequency spacing between the transitions, justifying a two-level treatment. This plot shall only give an impression of the distribution of the resonance frequencies and their width. It deviates significantly from the measured signal as, among other things, there is deliberately no weighting due to the initial state occupation. Each transition was plotted with an oscillation strength leading to a π -flip.

equation 2.10. The detector then gives a signal proportional to the trace of the density matrix $\langle \Psi | \Psi \rangle \leq 1$ which is smaller than unity due to the loss mechanism.

An ideal analysis would correspond to a projection onto the ground state $|1\rangle$, however, in reality the state analyser is described by a more general matrix with only diagonal elements:

$$M_A = \sum_n c_{n,A} |\phi_n\rangle \langle \phi_n|. \quad (2.12)$$

2.3.3 State excitation

In the second region the transition between different eigen states is driven by a variation of the boundary condition. This is achieved by mechanically oscillating the mirror of region II with an oscillation amplitude A_x and frequency $f = \omega/(2\pi)$:

$$V(z, t) = mgz + V_F \Theta(A_x \sin \omega t) \quad (2.13)$$

The solution of the Schrödinger equation can be found in various text books covering Rabi's method e.g. [Fox, 2006] and is only presented here as a rough sketch.

Looking at just one transition we can determine the time-dependency of the state population of the two involved levels by treating the system as a qubit. Like a spin- $\frac{1}{2}$ system the time evolution is described by a $SU(2)$ matrix. In our system the transition frequencies are well separated due to the non-equidistant eigen energies, see figure 2.5. It is thus justified to use the two-level approach. In the previously realised setup, an additional boundary condition imposed by a second top mirror, shifted the eigen energies such that some transition frequency became close to degeneracy. The system could be treated with a three-level formalism [Jenke, 2011], however the experimental slit height is difficult to determine experimentally.

For the two-level description, the solution of the Schrödinger equation tells how the population of the states $|i\rangle$ and $|j\rangle$ evolves with time:

$$\begin{pmatrix} c_i(t) \\ c_j(t) \end{pmatrix} = \begin{pmatrix} \cos\left(\frac{\Omega_{RS}t}{2}\right) + i\frac{\delta\omega}{\Omega_{RS}}\sin\left(\frac{\Omega_{RS}t}{2}\right) & -\frac{\Omega_R}{\Omega_{RS}}\sin\left(\frac{\Omega_{RS}t}{2}\right) \\ \frac{\Omega_R}{\Omega_{RS}}\sin\left(\frac{\Omega_{RS}t}{2}\right) & \cos\left(\frac{\Omega_{RS}t}{2}\right) - i\frac{\delta\omega}{\Omega_{RS}}\sin\left(\frac{\Omega_{RS}t}{2}\right) \end{pmatrix} \begin{pmatrix} c_i(0) \\ c_j(0) \end{pmatrix}, \quad (2.14)$$

where t is the interaction time, during which the neutron is exposed to the varying potential. The Rabi frequency $\Omega_R = \langle i | \partial_z | j \rangle A_v$ depends on the overlap $\langle i | \partial_z | j \rangle$ and the oscillation strength $A_v = \omega A_x$. A_v is the maximal velocity of the oscillation, A_x the maximal displacement. The generalized Rabi frequency $\Omega_{RS} = \sqrt{\Omega_R^2 + \delta\omega^2}$ includes the frequency detuning $\delta\omega = 2\pi(f - f_{ij})$, which describes the offset of the applied frequency f from the resonance frequency f_{ij} of the transition $|i\rangle \leftrightarrow |j\rangle$. The overlap $\langle i | \partial_z | j \rangle$, calculated in appendix A.5, is a function on z_0 . The transition frequency f_{ij} depends on the energy scale E_0 . So they both can well be re-parametrised to be functions of the local acceleration g .

The probability P_i to find the state $|i\rangle$ populated after region II when the state $|i\rangle$ was initially prepared, $c_i(0)^2 = 1, c_j(0)^2 = 0$, is given by:

$$P_i = |c_i(t)|^2 = \left(\frac{\delta\omega}{\Omega_{RS}}\right)^2 + \left(\frac{\Omega_R}{\Omega_{RS}}\right)^2 \cos^2(\Omega_{RS}t/2). \quad (2.15)$$

A state population reversal, a so-called π -flip, occurs at the oscillation strength $A_v = \pi / (\langle i | z | j \rangle t)$, which can be solved analytically with equation A.12. The overlap integral $\langle i | z | j \rangle$ is inversely dependent on the transition frequency ω . With an interaction time $t = 25$ ms, the oscillation amplitude $A_x = \frac{\pi}{t} \frac{2\pi\hbar z_0}{E_0} = 5 \mu\text{m}$ gives a π -flip for each transition upon resonance. However, for technical reasons concerning the oscillation stability of the nano-positioning table, most measurements were performed with constant maximum oscillation strength of $A_v \sim 2 \text{ mm s}^{-1}$.

If the state preparation leaves also the state $|j\rangle$ populated, equation 2.15 is modified and gives:

$$P_i = \langle i | \Psi \rangle = c_i^2 + (c_j^2 - c_i^2) \left(\frac{\Omega_R}{\Omega_{RS}}\right)^2 \sin^2(\Omega_{RS}t/2) - c_i c_j \frac{\Omega_R}{\Omega_{RS}} \sin^2(\Omega_{RS}t), \quad (2.16)$$

with the initial state occupations c_a and c_b . As the phase θ between the state $|i\rangle$ and $|j\rangle$ is unknown in the experiment and cannot be assumed constant, the phase has to be integrated over and the probability of finding the neutron in the state are $|i\rangle$:

$$P_i = \frac{1}{2\pi} \int_0^{2\pi} \langle i | \Psi \rangle d\theta = 1 + \left(\frac{c_b^2}{c_a^2} - 1\right) \left(\frac{\Omega_R}{\Omega_{RS}}\right)^2 \sin^2(\Omega_{RS}t/2). \quad (2.17)$$

To include the region III into the analysis, we apply the corresponding matrix M_{ij} and obtain the following norm of the final state behind region III, normalised to the state

before region II:

$$\begin{aligned}
 P_{ij} = P_i + P_j &= \frac{1}{2\pi} \int_0^{2\pi} \langle \Psi | \Psi \rangle d\theta = 1 + \left(\frac{c_a^2 p_2^2 + c_b^2 p_1^2}{c_a^2 p_1^2 + c_b^2 p_2^2} - 1 \right) \frac{\Omega_R^2}{\Omega_{RS}^2} \sin^2(\Omega_{RS} t/2) \\
 &= 1 - k_{ij} \frac{\Omega_R^2}{\Omega_{RS}^2} \sin^2(\Omega_{RS} t/2), \quad (2.18)
 \end{aligned}$$

where the unknown initial state occupations and the selection efficiencies are subsumed into the contrast k_{ij} . This is especially advantageous if the preparation and selection efficiencies c_i and p_i are not experimentally accessible. The contrast is symmetric with respect to the preparation and analysis.

When more than two states are in the interaction region, but transitions only take place within two states at a time, while the others are not influenced, then the total probability is simply the combined one. The total signal describing the two transitions $|1\rangle \leftrightarrow |3\rangle$ and $|1\rangle \leftrightarrow |4\rangle$ then reads:

$$P = P_{13} + P_{14} - 1 = 1 - k_{13} \frac{\Omega_{R13}^2}{\Omega_{RS13}^2} \sin^2(\Omega_{RS13} t/2) - k_{14} \frac{\Omega_{R14}^2}{\Omega_{RS14}^2} \sin^2(\Omega_{RS14} t/2). \quad (2.19)$$

The approach that the transitions can be described separately, leads to the description of the total signal as a sum of the individual signals with their separate contrasts.

Chapter 3

Experimental realisation of Rabi-type GRS

The measurements presented in this work were performed at the UCN beam line at the PF2 platform of the Institut Laue-Langevin¹ (ILL), which is known for its high-flux neutron-source reactor. We were allocated the experiment number *3-14-305* which was scheduled during the reactor cycles 167 and 168 from 28.08.-12.11.2012. In between the two cycles there was a planned reactor shut down for a fuel rod change. After setting up the experiment and performing various tests on the parts of the setup and initial preparations we started measuring the transmission of neutrons through the full 3-part Rabi setup as a function of the oscillation frequency and amplitude.

In this chapter, the various components of the experiment, as used during the beam time, are presented and their physical implications are discussed in detail. The methods, like the velocity selection of ultra-cold neutrons (UCNs) and the preparation of the quantum system, are theoretically studied and evaluated. It is followed by a discussion of the realisation for induced state transitions. Afterwards, the driving and monitoring of the mechanical oscillations is discussed. The methods of neutron detection used in the experiment are presented and followed by a discussion of the obstacles with the setup alignment and ways of dealing with them. The vacuum chamber and its purpose are mentioned briefly. The observed rate dampening concludes the chapter together with an analysis of external influences such as the moon and the rotation of the Earth.

3.1 Technical realisation and its systematic investigations

3.1.1 Neutrons time-of-flight

Selecting trajectories with Collimating blades

The experiment is of the so-called "flow-through" type, meaning that the neutrons pass through our setup horizontally. The aim is that the neutrons form bound quantum states close to the ground state with transversal energies in the pico-eV regime. Controlling and determining their horizontal velocity while preparing them at the same time in a vertical quantum state is the task of the velocity selector.

¹<http://www.ill.eu>

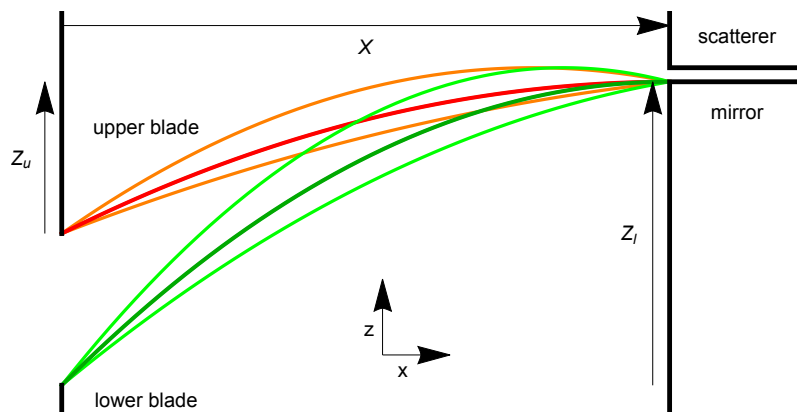


Figure 3.1: Velocity selection with mechanical blades. In this part of the experiment and only here it is sufficient to consider the flight path of neutrons on classical trajectories. Neutrons come from the left and fly ballistically to region I (shown in 2.3) which is the mirror-scatterer system indicated to the right. The neutrons can only exit region I on the right when they have a small vertical velocity v_z inside the mirror-scatterer system. The mirror and the scatterer are separated by the height l . The origin of the coordinate system is chosen to be the upper front edge of the lower neutron mirror. The region between the orange (green) curves indicates the flight paths for neutrons within the accepted velocity range entering at the upper (lower) paddle. The image is not to scale.

Based on previous realisations [Jenke, 2008] the velocity selector consists of a pair of collimating blades and the state selector, a mirror-scatterer system, of region I (see figure 3.1). The collimating blades are made of boronated steel with high neutron absorption cross section and can be adjusted to desired heights. Neutrons on other trajectories are absorbed. The mirror-scatterer system itself consists of a neutron mirror with a flat surface at the bottom and a mirror on top with a roughened-up surface, also called the scatterer. The mirrors are separated by two spacers on the left and right sides, such that there is a slit with height l between the mirror and the scatterer. While neutrons are reflected totally from the flat mirror surface, those which can interact with the rough surface are likely to get scattered out of the system and hence are effectively removed from the description. Neutrons which ascend in the gravity potential behind the paddles are only accepted by the mirror-scatterer system if their vertical velocity component v_z is small enough inside the mirror-scatterer system such that they do not interact with the scatterer. All other neutrons are removed from the system. This mechanism imposes a condition on the horizontal velocity component.

In the case that the slit height is negligible, only neutrons with the following horizontal velocity component v_x are accepted:

$$X\sqrt{\frac{g}{2Z_l}} \leq v_x \leq X\sqrt{\frac{g}{2Z_u}}, \quad (3.1)$$

where X is the distance from the paddles to the mirror-scatterer system, $Z_{l,u}$ the position of the lower/upper paddle from the upper surface of the lower mirror and g the local acceleration.

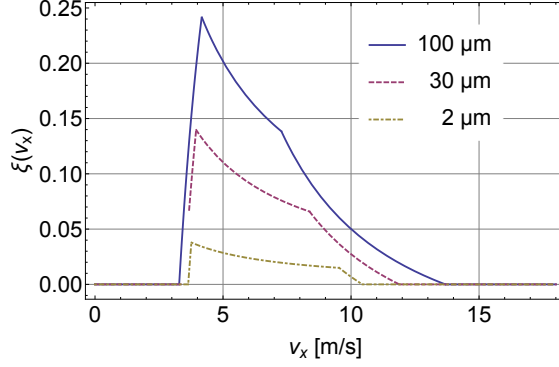


Figure 3.2: The influence of the slit height l expressed by the geometric factor $\xi(v_x)$. The curves are normalized to the $l = 100 \mu\text{m}$ curve. Decreasing the slit height leads, besides an overall flux reduction, to a suppression of lower horizontal velocities v_x and prevents the smearing of the higher cut velocity. For the vanishing slit height, the spectrum is not continuous any more but jumps to the plateau between v_{xl} and v_{xu} .

Interplay between blades and state selector

Equation 3.1 has to be adapted when the slit height l between the mirror and the absorber is not neglected. A neutron passing point $(x, z) = (X, Z)$ (with the origin set to the upper front edge of the lower mirror) is accepted if its vertical velocity at the slit entrance is:

$$\frac{X}{2Z} \left(\sqrt{2gl} - \sqrt{-2g(l-Z)} \right) \leq v_x \leq \frac{X}{2Z} \left(-\sqrt{2gl} - \sqrt{-2g(l-Z)} \right). \quad (3.2)$$

Neutrons with such velocities follow trajectories as indicated in figure 3.1.

The horizontal velocity spectrum $p(v_x)$ that is observed behind the velocity selector is obtained by integrating equation 3.2 over the paddle opening with the appropriate incoming velocity distribution $p_I(v_x, z)$ that the beam has at the horizontal position of the paddles:

$$p(v_x) = N \int_{Z_l}^{Z_u} p_I(v_x, z) \Theta(v_z - v_{zl}(z)) \Theta(v_{zu}(z) - v_z) dz, \quad (3.3)$$

with the appropriate normalisation condition N , and the limiting velocities v_{zl}, v_{zu} from equation 3.2 for the vertical velocities at the paddle positions $v_z(v_x, X) = \frac{gX}{v_x}$.

For the case where the incoming distribution is homogeneous in z , equation 3.3 simplifies to:

$$p(v_x) = N p_I(v_x) \xi(v_x), \quad (3.4)$$

where the remaining integral can be calculated analytically and results in a purely geometric factor $\xi(v_x)$ (see figure 3.2):

$$\xi(v_x) = \max \left(\min \left(Z_u, \frac{gX^2}{2v_x^2} - \frac{\sqrt{2lg}X}{v_x} \right) - \max \left(Z_l, \frac{gX^2}{2v_x^2} + \frac{\sqrt{2lg}X}{v_x} \right), 0 \right). \quad (3.5)$$

For given positions of the paddles, equation 3.5 can also be expressed as a normalized function of v_x :

$$v_c = \sqrt{2gl}, \quad v_i = \frac{Xv_c}{2} \left(\frac{\left(\sqrt{1 - \frac{Z_l}{l}} \mp 1 \right) / Z_l}{\left(\sqrt{1 - \frac{Z_u}{l}} \mp 1 \right) / Z_u} \right), \quad (3.6)$$

$$\begin{aligned} \bar{\xi}(v_x) = \frac{1}{\log \frac{Z_l}{Z_u}} & \left(\Theta(v_x - v_I) \Theta(v_{III} - v_x) \left(v_x^{-1} - \frac{gX}{2v_c} v_x^{-2} \right) \right. \\ & + \Theta(v_x - v_{II}) \Theta(v_{IV} - v_x) \left(v_x^{-1} + \frac{gX}{2v_c} v_x^{-2} \right) \\ & + \Theta(v_x - v_I) \Theta(v_{II} - v_x) \frac{Z_l}{Xv_c} \\ & \left. - \Theta(v_x - v_{III}) \Theta(v_{IV} - v_x) \frac{Z_u}{Xv_c} \right). \end{aligned} \quad (3.7)$$

Depending on the choice of experimental values, different terms of equation 3.7 dominate and lead to either a step-like or a mainly inverse- v_x form of the geometric factor. The log-term ensures the correct normalisation.

Simulations of a velocity selection with rough media can be found in [Chizhova et al., 2014]. Additionally, UCNs have to pass through multiple aluminium foils which cuts their velocity spectrum at the critical velocity of aluminium. As this is around 3.2 m s^{-1} it has no effect on the presented experimental setup.

Application during beam time 3-14-305

The incoming velocity spectrum was determined by a measurement set conducted in the beginning of the beam time *3-14-305*. The lower mirror had a width of 200 mm, the upper one of 100 mm, both were 150 mm long. The slit between them was set to the height $l = (98.5 \pm 0.6) \mu\text{m}$ (see table 3.1). The total flux P , being the integral of equation 3.2, was measured as a function of the lower paddle's position while keeping the upper paddle fixed (see figure 3.3).

The incoming velocity distribution $p_I(v_x)$ was assumed to be a polynomial of order four with six independent parameters. The total flux P was integrated analytically for all measured values of the lower paddle position. By fitting P with the least-square method, by minimizing the χ^2 , the values for the parameters were obtained. Figure 3.3 shows the measurement together with the fitted curve. The velocity distribution during the experiment can now be calculated analytically by applying the corresponding geometrical factor for the paddle values and slit size to be found in table 3.1 (see Figure 3.4).

The final settings for the beam time *3-14-305* are displayed in table 3.1. Neglecting the slit width between the mirrors gives an acceptance of $(5.6 \text{ to } 9.5) \text{ m s}^{-1}$.

Influence of the velocity spread

The interaction time τ of the neutron with the oscillating potential in region II is determined by the velocity v_x of the neutrons. To account for the velocity spread in the experiment, the expected Rabi-like signal displayed in section 2.3 has to be integrated

		Velocity measurement	Experiment
slit height	l	$(98.5 \pm 0.6) \mu\text{m}$	$30 \mu\text{m}^*$
upper paddle	Z_u	-1.1 mm	-1.1 mm
lower paddle	Z_l	$(-5.1 \text{ to } -1.1) \text{ mm}$	-3.0 mm
flight distance	X	140.5 mm	140.5 mm

Table 3.1: Parameters of the setup used during beam time *3-14-305*. After the determination of the incoming velocity spectrum in a measurement series with varying position of the lower paddle, the gravity resonance spectroscopy measurements were performed with the settings displayed in the right column. The given slit height for the experiment (marked by *) is the nominal slit height, the actual value is obtained by the track detector measurement in subsection 3.1.2.

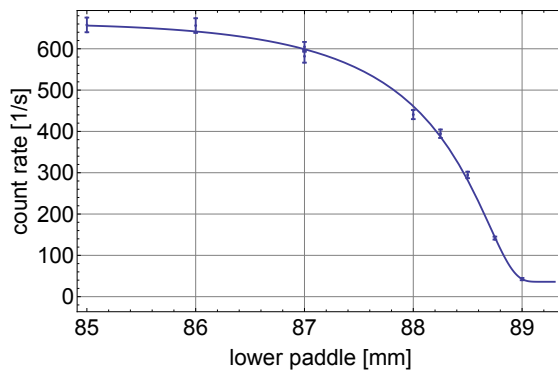


Figure 3.3: The data points obtained for the velocity spectrum measurement. The solid line is the fitted curve for the total flux P behind the setup in dependence of the lower paddle position Z_l .

with the determined velocity spectrum $p(v)$ given in equation 3.7:

$$\bar{P}(f, a) = \int_0^{\infty} P(f, a, \tau = 1/v) p(v) dv \quad (3.8)$$

The influence of the selected velocity spectrum on a generic Rabi-like signal with oscillation strength $a_v = 2 \text{ mm s}^{-1}$ is shown in figure 3.5. As this oscillation strength does not correspond to a full π -flip, the contrast of the $|1\rangle \leftrightarrow |4\rangle$ transition decreases with velocity. However the width of the dip is inverse proportional to the interaction time τ . Including these effects, the velocity-averaged curve deviates very little from the curve obtained for the averaged velocity. Thus, the velocity spread of the neutrons is not critical and it is sufficient to use a mean velocity and a mean interaction time. For the further analysis and evaluation only the mean velocity is used.

3.1.2 State preparation and analysis with rough boundary conditions

Determination of roughness parameters

The state selection discussed in section 2.3.1 is realised with neutron mirrors who have a rough surface. Neutrons in higher states, being more likely to interact with the rough surface, get scattered out of the system and are thus effectively suppressed. The rough

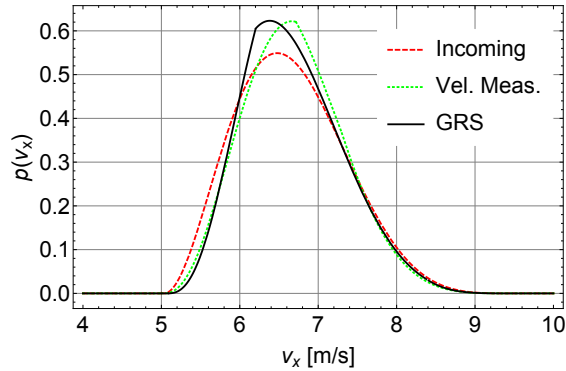


Figure 3.4: Comparison of normalised velocity spectra. The dotted line shows the velocity spectrum behind region I during the velocity measurements for the lower paddle position used later on. The dashed line shows the deduced velocity spectrum at the paddles. The solid line is the velocity spectrum used later on for the gravity resonance spectroscopy.

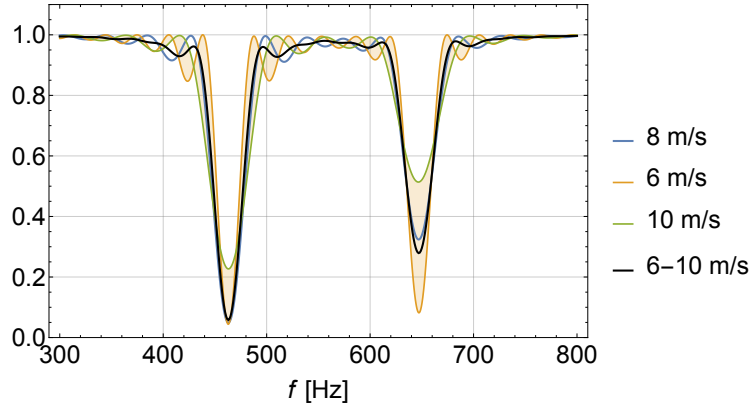


Figure 3.5: A generic Rabi-like signal for two transitions is shown for the neutron velocities $v_x = 8$ m/s (blue), $v_x = 6$ m/s (red), $v_x = 10$ m/s (brown) and for a velocity spectrum 6 m/s $< v_x < 10$ m/s (black). The plot is drawn for an oscillation strength of $a_v = 2$ mm s $^{-1}$. As this does not correspond to a full π -flip for the transition $|1\rangle \leftrightarrow |4\rangle$ at 642 Hz, the contrast of the transition reduces from $v_x = 6$ m/s to $v_x = 10$ m/s. The width of the Rabi curve decreases with the velocity. Together with the change in contrast, however, the slopes of the curve are only hardly effected. The curve for the neutron velocity $a_v = 8$ m s $^{-1}$ and the velocity-averaged curve (both in bold) deviate insignificantly.

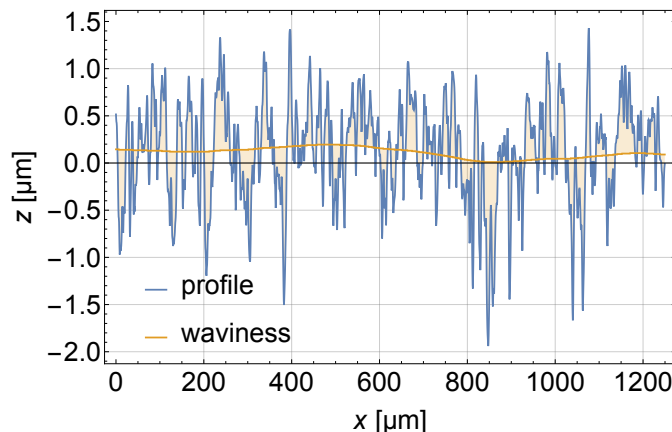


Figure 3.6: The profile and the waviness of a typical neutron scatterer. The roughness is just the difference between the two and is indicated through the shaded area. The horizontal resolution of the plot is $0.5 \mu\text{m}$, the vertical is $0.005 \mu\text{m}$.

surface is produced by manually roughening with corundum. For this the mirror was covered with corundum paste and moved in a trained way. It is a highly sensitive task, as large-scale waviness needs to be avoided and the task needs a few iterations.

There are two distinct measurement methods to measure the roughness of surfaces: A 1-D scan with a tip moving across the surface and recording the height. The resolution of the scan is limited by the tip which has a certain radius of $2 \mu\text{m}$ which leads to the smoothing of very sharp and narrow valleys. The obtained profile can be seen in figure 3.6. The rough surface can be characterised by a set of roughness parameter: the height profile $P(x) = R(x) + W(x)$ is comprised of the roughness R , which describes the low scale fluctuations and the waviness W for the large scale behaviour. They are obtained by filtering the profile for a certain cut-off length λ_c . In our case we chose a cut-off wave length $\lambda_c = 0.8 \text{ mm}$ between the roughness and the waviness, which is the DIN EN ISO4287 standard for a non-periodic roughness in the range $R_z = (0.5 \text{ to } 10) \mu\text{m}$. The standard defines the roughness measurement as follows: the measurement length that the needle travels is $5\lambda_c$ with an additional half a wavelength λ_c before and after to allow for accurate filtering. During the measurement N samples of the height are taken, dependent on the horizontal resolution of the device. In our case, the horizontal resolution was $0.5 \mu\text{m}$, the nominal vertical resolution $0.005 \mu\text{m}$. The roughness parameter are defined as R_a , the arithmetic mean of the five sections and R_z , the mean of the five maximum peak-to-peak heights within five sections:

$$R_a = \frac{1}{5N} \sum_{i=1}^{5N} |z_i|, \quad R_z = \frac{1}{5} \sum_{i=1}^5 (z_{\max,i} - z_{\min,i}). \quad (3.9)$$

The roughness of the two mirrors 306 and 307 used in the experiment were $R_z = (3.65 \pm 0.45) \mu\text{m}$, $R_a = (0.38 \pm 0.17) \mu\text{m}$ and $R_z = (3.38 \pm 0.34) \mu\text{m}$, $R_a = (0.37 \pm 0.15) \mu\text{m}$ respectively. A detailed characterisation of the surface properties was performed during a student project and a master thesis [Jung, 2013, Wautischer, 2015].

The second method uses a scanning electron microscope to raster the surface and

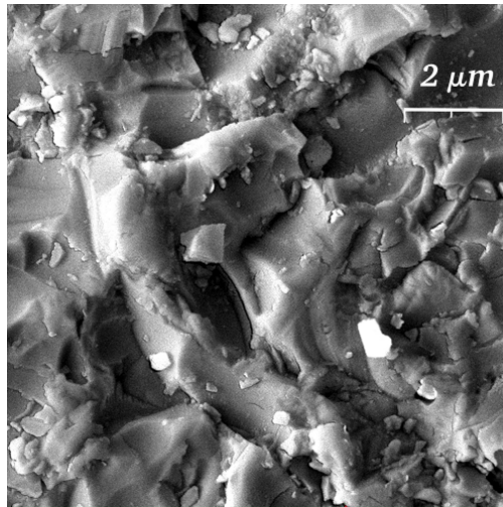


Figure 3.7: A scanning electron microscope picture of the scatterer’s rough surface coated with ^{58}Ni of minimal thickness around 50 nm as not to alter the roughness parameters. The nickel coating makes the surface conducting. The coating was done by D. Seiler at the Technische Universität München. The picture was taken by the USTEM.

gives a 2-D scan. For this method, the surface needs to be conducting, so a scatterer coated with ^{58}Ni was used. The coating has a thickness of around 50 nm and was done with electron-beam physical vapour deposition (EBPVD). There, a high-energy electron beam vaporizes the substrate, nickel in this case, which then gets deposited onto an exposed surface, here, the rough mirror. A picture obtained by a scanning electron microscope at the USTEM facility² can be seen in figure 3.7. The horizontal and vertical resolution was 10 nm. The obtained surface parameters, agreeing with the 1-D measurements, were also used for studies on a velocity filter of ultra-cold neutrons for transport dynamics [Chizhova et al., 2014].

Track detector measurement

To check the functionality of region I and III, the vertical probability distribution of the neutrons behind a mirror-absorber system was measured based on a method presented here. For that reason a roughed up mirror was put above a flat mirror separated by brass spacers of nominal height $l = 30 \mu\text{m}$. Such a setup suppresses higher states as described in section 2.3.1.

The slit size used in the experiment requires a quantum mechanical description. If the slit size exceeds $\gtrsim 200 \mu\text{m}$ the neutron transmission rate $r(l) \propto l^{2/3}$ depends on the slit height l as follows from phase-space considerations. The first experimental demonstration of gravitationally bound ultra-cold neutrons showed deviations from the classical curve as expected from quantum mechanics for small slit heights [Nesvizhevsky et al., 2002]. As a standard, the measurement was repeated with this setup. The transmission rate was recorded with spacers of different heights (see figure 3.8).

²Universitäre Service-Einrichtung für Transmissionselektronenmikroskopie (USTEM) <http://www.ustem.tuwien.ac.at>

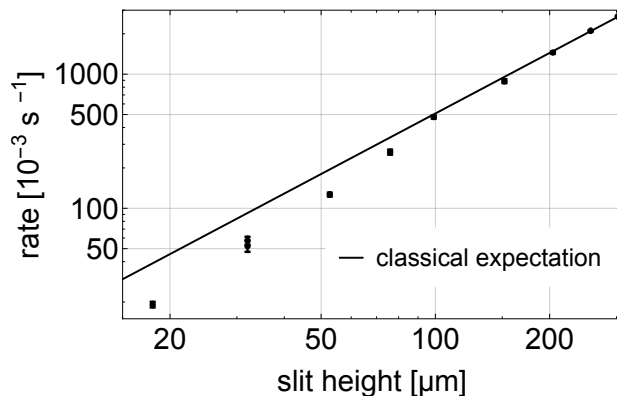


Figure 3.8: Dependence of the transmission rate on the slit height. The curve of behaviour $l^{3/2}$ is fitted to the points higher than 190 μm , where the points follow the classical behaviour. At lower slit heights the points are well below the curve in accordance with the first demonstration of gravitationally bound UCNs [Nesvizhevsky et al., 2002].

The vertical probability density of the neutrons was measured with a boron coated track detector. A $\approx 220 \mu\text{m}$ thick ^{10}B layer is deposited onto a CR-39 track detector using electron-beam physical vapour deposition³. The ultra-cold neutron is captured by the ^{10}B layer and one of the two daughter products (α particle or lithium ion) can leave tracks in the CR-39 detector (for the two interaction channels see equation 3.13). The layer thickness was adapted to the neutron velocity to maximize the detector efficiency [Klein, 2000, Stadler, 2009, Saul, 2011]. After the measurement, the boron layer is removed and the tracks are enlarged by chemical etching until the tracks can be read out optically with a microscope. Using sophisticated track reconstruction, the capture position of the neutron is obtained. For a detailed description see [Jenke et al., 2013].

Initial state occupation

The result of such a measurement with the track detector labelled *L9* can be seen in figure 3.9. The track detector was exposed to a neutron flux of $(70.9 \pm 3.1) \times 10^{-3} \text{ s}^{-1}$ for 59 hours. 5051 tracks including background events were recorded. For this measurement, the mirror-absorber system was placed on a commercially available height/tip/tilt table. The table's three internal capacitive sensors were permanently read out to log the stability of the setup (see figure 3.10).

A convolution has to be performed which accounts for the spatial resolution of the track reconstruction. The point-spread function is assumed to be of Gaussian form with a specific broadening σ . The measured wave function probability with the contribution c_i of the first three states ψ_i can be seen in figure 3.11. Even though the data is displayed in binned form, the parameters presented in table 3.2 were obtained by fitting with a χ^2 -method. Additionally a maximum-likelihood analysis was performed which yielded similar results. The vertical probability distribution used was:

³The boron coating of the track detector was done by D. Seiler at the Technische Universität München.

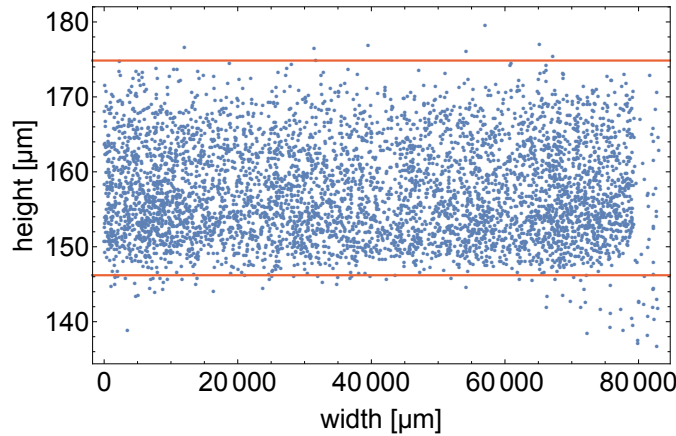


Figure 3.9: Track detector *L9*. Each dot corresponds to a reconstructed track from a Li-ion or an α particle. The exposed area was roughly $40 \mu\text{m} \times 80 \text{mm}$. The upper surface of the bottom mirror was around height position $146.2 \mu\text{m}$ and is not visible as a sharp edge due to statistics and the broadening of the point-spread function. The horizontal lines indicate the position of the lower and upper mirror as determined from the data analysis.

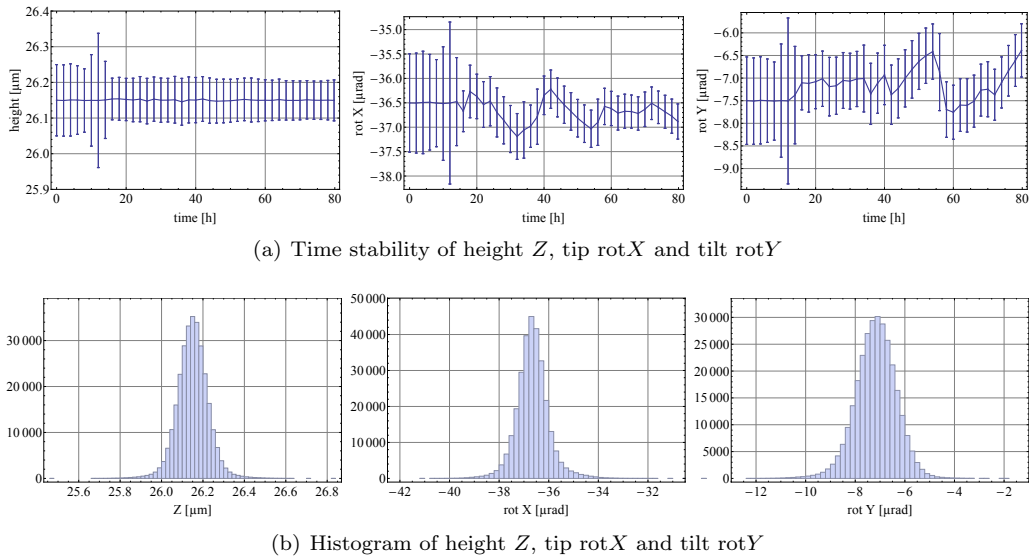


Figure 3.10: Stability of the mirror-absorber system during track detector measurement *L9*.

$$p(z) = B + \int_{-\infty}^{\infty} \frac{\exp^{-\frac{z'^2}{2\sigma^2}}}{\sqrt{2\pi}\sigma} \sum_{i=1}^3 c_n \phi_n^2(z - z' + z_{\text{Offset}}, l) dz'. \quad (3.10)$$

From table 3.2, it can be seen that the initial state preparation does not work ideally but also leaves the second and third state populated after region I. The initial state preparation is very dependent on the manually produced roughness of the neutron scatterer.

Decreasing the slit height removes higher states more aggressively but as discussed

slit height	l	$28.45^{+0.62}_{-0.49}$
occupation of state I	c_1	$59.70^{+1.59}_{-1.48}\%$
occupation of state II	c_2	$34.03^{+2.17}_{-2.15}\%$
occupation of state III	c_3	$6.27^{+2.61}_{-2.68}\%$
z-offset	z_{Offset}	$-11.2^{+0.1}_{-0.1} \mu\text{m}$
norm	N	$1440^{+21}_{-21} \text{ cts/bin}$
background	B	1.1 cts/bin
broadening	σ	$1.36^{+0.13}_{-0.14} \mu\text{m}$

Table 3.2: Results of the track detector analysis obtained by fitting the data. with a $\chi^2_{\text{red}} = 0.86$ with 7 parameters.

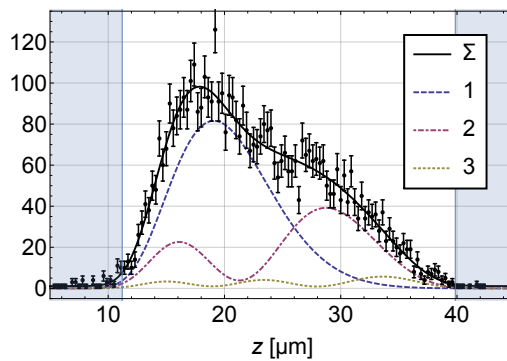


Figure 3.11: Spatial probability distribution behind the mirror-scatterer system as determined by the track measurement. The solid, black line is the sum of the three dashed lines depicting the probability distribution of the first three states broadened by the spatial resolution of the tracking process. The second bump below the position $30 \mu\text{m}$ is due to the contribution of the second state. The bottom of the mirror slit is above $10 \mu\text{m}$, the slit height is below $30 \mu\text{m}$ as indicated by the shaded regions. The values obtained by fitting can be found in table 3.2. Notice that the curves do not approach the background immediately at the lower mirror around $11 \mu\text{m}$, which is due to the broadening. The physical wave function however does not penetrate the mirror.

in the subsequent section, this does not necessarily produce the desired initial state occupation in region II.

3.1.3 Setup alignment

Setup layout The setup with its three regions consists of multiple mirrors (see figure 2.3). The lower mirrors have all a width of 200 mm, the upper mirrors only found in region I and III with their roughed up lower surface have a width of 100 mm. The lengths of the mirrors in region I and III are 150 mm while the length of the mirror in region II is 200 mm. Together they bring the total length of the mirror system to 500 mm. In comparison with the setup used in the previous experiments [Jenke, 2011, Jenke et al., 2014] which combined all three regions into one with a length of 150 mm, the increased experimental requirements are perceptible. The length of region II now allows for an increased interaction time by one third which results directly in a reduced width of the

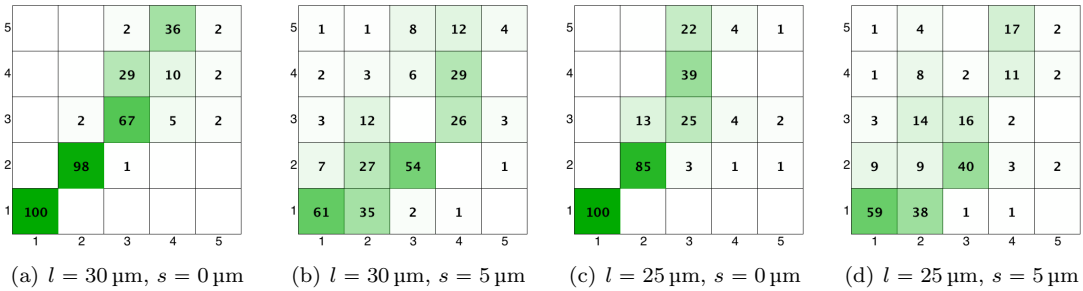


Figure 3.13: The transition probability $\int \phi_i^*(z)\psi_j(z-s)dz$ in percent shown for different slit heights l in region I and steps s between region I and II. The horizontal axes labels denote the eigenstate i in region I, the vertical axes the eigenstate j in region II. In (c), the second state in region I populates the third state with 13% probability compared to 2% in (a) which is due to the energy shift induced by the upper mirror in region I. The neutron has to "climb up" against a step of $5 \mu\text{m}$ in (b) which leads to lower state occupations compared with (a). For the transition from region II to region III the matrices need to be transposed. Each row and column sum up to unity when considering all states.

Figure 3.13 shows the overlap probability for different slit sizes and steps: as one would expect, there is a higher probability of finding the neutron in a higher state when going from a region with an upper mirror to a region without one. With a slit width $l = 25 \mu\text{m}$ and no step, the transition probabilities between the states i and j are shown in section 3.13(c). In region II the third state gets populated by 13% from the second state in region I. Steps of $s = 5 \mu\text{m}$ lead to significant mixing of state populations, they need to be avoided to maintain the state preparation from region I.

While decreasing the slit height in region I results in an increased suppression of higher states, it also increases the eigen energies of the states. But this leads to an increased population of higher states in region II as can be seen in figure 3.13.

Steps & gaps, Tip & tilt

The alignment of the neutron mirrors can be controlled by an external sensor system consisting of five capacitive sensors *D-510.101* from the company Physik Instrumente⁵. The system was designed by H. Filter. Each sensor measures the separation to the neutron mirror surfaces, which were electrically grounded for that purpose, within a measurement range of $100 \mu\text{m}$. The sensors are mounted on a translation stage to scan the mirror surfaces in the direction parallel to the neutron path with a vertical distance of roughly $200 \mu\text{m}$. Three of the sensors are placed above a flat reference mirror next to the actual setup to determine the wobble of the translation stage during its movement and correct for it. The dimensions of the neutron mirror with a width of 200mm was chosen larger than the neutron path so that the remaining two sensors can scan the mirror surface to the left and right of the neutron path. This allows to detect steps even during measurement. A schematic view of the capacitive sensor system can be found in

⁵Physik Instrumente (PI) GmbH & Co. KG, Auf der Römerstraße 1, 76228 Karlsruhe, Deutschland, <http://www.pi.de/>

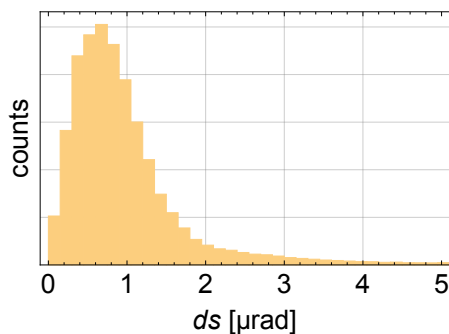


Figure 3.14: Histogram of the total inclination ds of the granite as achieved by a closed-loop control during the experiment. A maximum likelihood estimation of a Maxwell distribution for the data without the tail gives a mean $\mu = 0.52 \mu\text{rad}$. The measured distribution however has a larger tail.

figure 2.3. Before each measurement, the regions were realigned to ensure steps smaller than $0.5 \mu\text{m}$.

Additionally the tip (the inclination parallel to the neutron velocity) and tilt (the inclination normal to the neutron velocity) of the mirrors with respect to each other can be determined by this capacitive sensor system. The granite on which the tables are placed acts as the reference frame for the overall tip and tilt of the experiment. The initial levelling of the granite was performed with a high sensitivity water-level. The granite itself is stabilized actively by a closed-loop control (PID), consisting of three piezo elements and a tip/tilt sensor. During the course of the experiment the closed-loop control stabilised the granite to values well below $5 \mu\text{rad}$ as can be seen in figure 3.14. The general long-term stability of the levelling PID was studied in a bachelor thesis [Fellinger, 2012].

While an inclination normal to the neutron velocity is without any effect, an inclination parallel to the velocity leads to a different separation of degrees of freedom and a reduced local acceleration: $g' = g \cos \alpha \approx g (1 - \alpha^2/2)$. For a tip of less than $10 \mu\text{rad}$ the effect can be neglected as a tilt of $10 \mu\text{m}$ corresponds to an energy shift of $6 \times 10^{-23} \text{eV}$ for the transition $|1\rangle \leftrightarrow |3\rangle$ which is many orders below our current sensitivity. The measured dependence on an overall tip within the range of the positioning table is shown in section 3.15.

Additionally a gap, that is a lateral spacing between the regions, is also unwanted. During assembly a gap as tiny as possible was introduced to ensure that the oscillations of region II can take place undisturbed and to prevent sympathetic oscillation in region I and III. The gap was measured to be $(50 \text{ to } 75) \mu\text{m}$. The change of height of a neutron with velocity $v_x = 5 \text{ m s}^{-1}$ is around 1.1 nm while bridging the gap of $75 \mu\text{m}$. The tiny gap is thus not critical.

3.1.4 Induced state excitation with mechanical oscillations

Driving oscillations

As mentioned before, the mirror in region II is mounted on a piezo-driven nano-positioning table. The table controller has an external input, which was connected to a wave func-

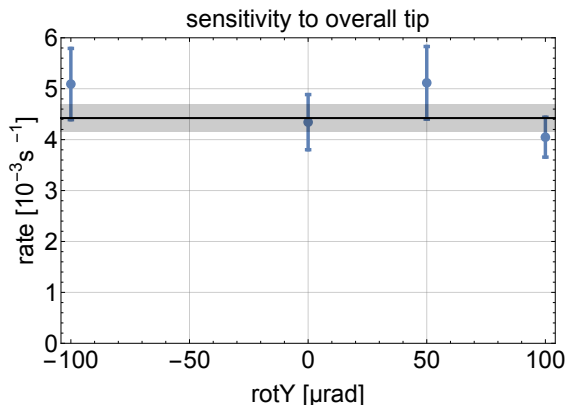


Figure 3.15: Dependence of the rate on the tip, i.e. the inclination of the mirror along the neutron velocity direction. Over a vast range, the tip has no influence on the transmission rate.

tion generator. To induce transitions between the different states, the wave function generator would feed a sinusoidal voltage with adjustable amplitude and frequency to the controller. There, the voltage is amplified and fed to each piezo individually whose elongations then follow the wave form. The weight of the mirror in region II and its mounting was designed to be ≈ 5.4 kg which leads to a mechanical resonance frequency of region II of 152 Hz. We chose to operate the system above its resonance frequency (see figure 3.18). As experience from previous beam times showed that the power consumption of the table controller increased with the applied oscillation strength and frequency, we employed a more powerful controller to access frequencies above 600 Hz. However, a few concessions had to be made as we could not drive the table with a strength greater than 2.3 mm s^{-1} at 650 Hz.

Monitoring oscillations

The oscillation of region II can be monitored by two different systems: internally with the included capacitive sensors inside the nano-positioning table and externally with a laser interferometer. The capacitive sensor system consists of three capacitive sensors which are located in the corners of the table. During the oscillation, their positions can be read out by software with a high sampling rate of up to 50 kHz. Such a measurement can be seen in figure 3.16.

Monitoring oscillations by laser interferometer During the whole experiment, the oscillation of region II was monitored by a three-axes laser interferometer from the company SIOS⁶. The main implementation was developed for a previous realisation of the experiment by T. Lins during the course of his Diplomarbeit [Lins, 2011] and adapted for this setup. The three beams of the laser interferometer are pointed at various positions on the mirror. One beam serves as a reference and shines on a fixed mirror. One beam scans the oscillating surface. For this the guiding optics, which consist of mirrors and penta prisms, were displaced with the use of two horizontal translation stages, one in

⁶SIOS Meßtechnik GmbH, Am Vogelherd 46, D-98693 Ilmenau, Germany, <http://sios.de/>

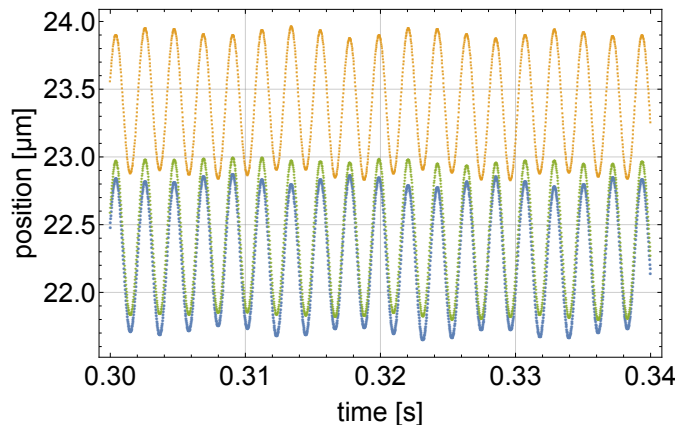


Figure 3.16: The position of the nano-positioning table as seen by its three internal capacitive sensors for an oscillation with a driving frequency $f_D = 462$ Hz. The offset is different for each sensor as the neutron mirror is aligned with respect to the other mirrors in region I and III. In the table-internal coordinate system this corresponds to an inclined plane. The sample rate of the capacitive sensors is 50 kHz. The correlations of the positions are $> 99.5\%$, their relative phases are $|\phi| < 0.28^\circ$.

neutron flight direction and one perpendicular to it. A drawing of the setup can be seen in figure 2.3.

The interferometer uses one polarisation of a He-Ne laser with a wave length of 632.8 nm and a power of ≈ 2 mW. The data recording is done in a burst mode where $N_B = 2^{13} = 8192$ length measurements are performed with a repetition rate $f_R = 2604.17$ Hz. The maximal detectable frequency according to the Nyquist theorem is $f = f_R/2 = 1302$ Hz and the spacing in the frequency domain is $\Delta f = f_R/N_B = 0.32$ Hz.

The monitoring was done in real time but can be repeated off line. The data evaluation scheme is displayed in figure 3.17. The recorded data, i.e. position over time, was translated into the frequency domain by discrete Fourier transformation (DFT). An example of such an obtained frequency spectrum is shown in figure 3.18, the driving frequency as well as the systems resonance frequency and the turbo pump can be seen. Owing to the nature of a DFT with a finite sample size, peaks appear to be smeared out and amplitude leaks into neighbouring frequencies. The spectrum was Gauss filtered around the driving oscillation and converted back to the time domain by an inverse discrete Fourier transform (iDFT). From there the oscillation amplitude was derived by a fit. Unwanted frequencies are orders of magnitude weaker in amplitude and at values un-critical for resonance spectroscopy. For example, the masses of the mirrors were chosen such that the resonance frequency of the setup itself lies well below 200 Hz where no transitions from the first few gravitational states are possible.

The result of an oscillation map can be seen in figure 3.19. The monitored area exceeded the area covered by the neutron path. Due to a weaker response of one piezo which could not be completely corrected by the electronic settings, a slight gradient can be observed for some measurements. To correct for this effect, a plane was fitted to the spatially distributed amplitude values and the mean value for the area covered by the neutrons was derived.

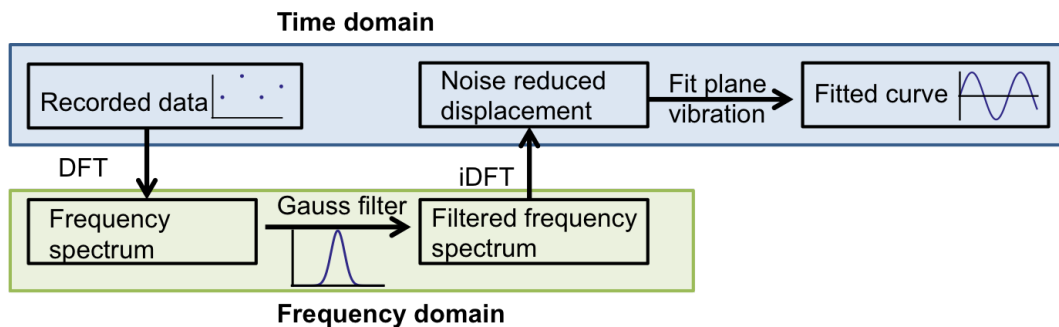


Figure 3.17: The scheme shows the measurement of oscillation strength and phase. The recorded raw data is transformed to the frequency domain by a discrete Fourier transform (DFT). A Gauss filter with width σ_G centred around the driving frequency f_D gives a filtered spectrum which is converted into the time domain by an inverse DFT (iDFT). The resulting data can be fitted with a sinus to obtain the oscillation strength and phase. The analysis is done in real time in LABVIEW to monitor the experiment and can also be done offline for post-process analysis.

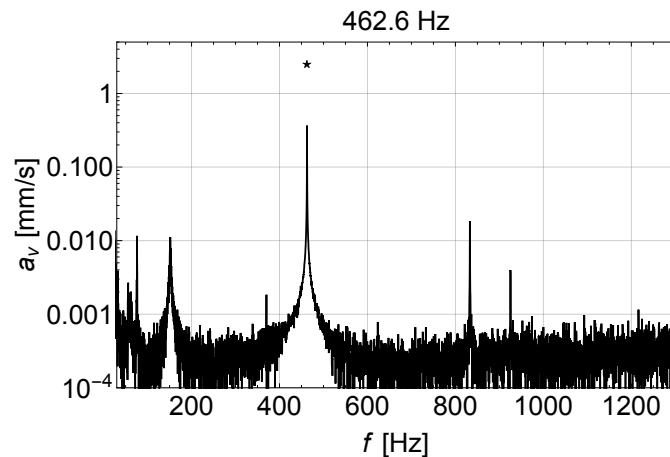


Figure 3.18: An exemplary raw frequency spectrum shows the maximal oscillation velocity as measured by the laser spectrometer. The driving frequency applied through the wave function generator was 462.6 Hz. The sample rate was 2604.17 Hz with 2^{13} measurement points. The peak seems to be very broad, leaking into neighbouring frequencies which is due to the nature of a discrete Fourier transform. After following the procedure described in figure 3.17, the value of $a_v = 2.52 \text{ mm s}^{-1}$, marked by the star, is obtained. Other frequencies are orders of magnitude smaller and can be neglected. The turbo pump can be seen at 833 Hz, the peak at 152 Hz is the resonance frequency of our table setup. The second harmonic of the driving frequency can also be seen. All other frequencies vanish in the noise floor.

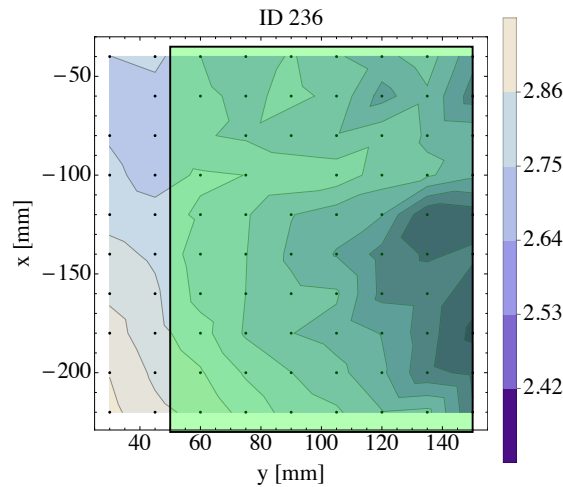


Figure 3.19: A map of the recorded oscillation amplitude of ID 236. The driving frequency was 462.6 Hz. Each dot corresponds to an amplitude measurement of the mirror surface in region II, the contour areas are interpolated. The neutron path is indicated by the green area, the beam enters at the top and leaves at the bottom.

The neutron mirror with its thickness of 35 mm is very stiff and so it follows the movement of the position table directly without any higher orders of oscillation being observed. The laser spectrometer also monitored the sympathetic oscillation of the regions I and III, that is if through some coupling these regions would also follow the driven oscillation in region II. In both regions the oscillation amplitude was observed to be well below 3% of the level of region II.

Calibration of the laser system Various external effects may influence the measurement by the laser system. Under certain circumstances sympathetic oscillations of parts of the setup, such as mirrors and mounts have been observed. As they might influence the oscillation measurement, depending on their strength and phase relative to applied oscillation, an additional, independent mean of calibrating the observed signal was implemented. For this, a second three-beam SIOS laser interferometer was employed outside the opened vacuum chamber on an external mounting. The only physical connection between the interferometer and the optics with the neutron mirrors was through the mounting of the platform which qualifies as a sufficient separation. The laser beams were directed in turn to fixed positions on the oscillating mirror of region II as well as the bottom mirrors of region I and III. Control measurements were performed during the reactor shut down between the reactor cycles 167 and 168 and after the end of the main measurements.

Implication of oscillation phase

If the oscillation of the mirror surface is not synchronised, this can have some implications. A phase gradient perpendicular to the direction of flight is of no concern. However a phase gradient $\Delta\phi/\Delta l$ parallel to the neutron velocity v will be experienced by the

neutron as a shifted frequency f' while moving over the surface with length l :

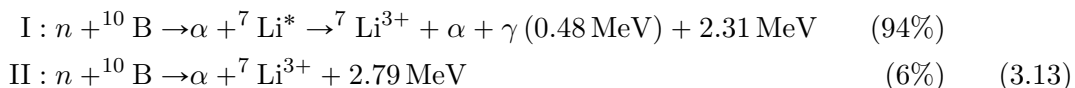
$$\begin{aligned} \cos(\omega t + \phi) &= \cos\left(\omega t + \frac{\Delta\phi}{\Delta l}x\right) = \cos\left(\omega t + \frac{\Delta\phi}{\Delta l}vt\right) = \cos(\omega't), \\ \Delta f &= f' - f = -\frac{v\Delta\phi}{2\pi\Delta l}. \end{aligned} \quad (3.12)$$

The measured phase uncertainty in the flight direction was smaller than 2° over the whole mirror length for all frequencies f . This corresponds to a maximum frequency shift of $\Delta f_\phi < 0.2$ Hz.

3.1.5 Neutron detection

Detection principle

Detector The neutron detector, located behind region III, is a highly background-optimized counter using a proportional chamber [Jenke et al., 2013]. The inside of the entrance window is ^{10}B coated to converted the ultra-cold neutrons to charged α -particles and Li-ions. The two possible reactions are:



The daughter products fly away back-to-back due to the low centre-of-mass momentum, so one of them may enter the gas volume. The volume is filled with ArCO_2 gas and a voltage of 700 V is applied between the detector housing and the collecting wire. The charge deposition is converted to a voltage measurement and fed into a time-resolved multi-channel analyser (MCA)⁷ with 1024 channels. The thickness of the converter layer and the materials of the detector were chosen carefully and are highly optimized to reduce background sensitivity. Here the background consists mainly of α particles from impurities in the detector material and external ionizing particles. The measured (background) spectrum of the detector can be seen in figure 3.20. While the coating of the detector foil had a width of 11 cm, the entrance was shielded to allow only an active area with a width of 9 cm which is slightly larger than the beam tube opening of the beam guide before the experiment. A detailed discussion of the detector concept can be found in [Saul, 2011].

Determination of background and incoming flux

Beam monitor The incoming neutron flux provided by the PF2 platform may be subject to changes from different origins, for example a modified reactor power or temperature instabilities of the cold neutron source. To account for these changes, a so-called beam monitor is installed upstream of the experiment. It is a ^3He detector attached to a connection between two beam guides who counts neutrons which are lost at the intersection. This provides a measure of the neutron flux in the beam guide. A detailed description can be found in [Jenke, 2011]. The (background) spectrum of the beam monitor is recorded by the same multi-channel analyser of our detector and can be found in figure 3.20.

⁷A commercially available *quadADC* from the company *ITECH Instruments*.

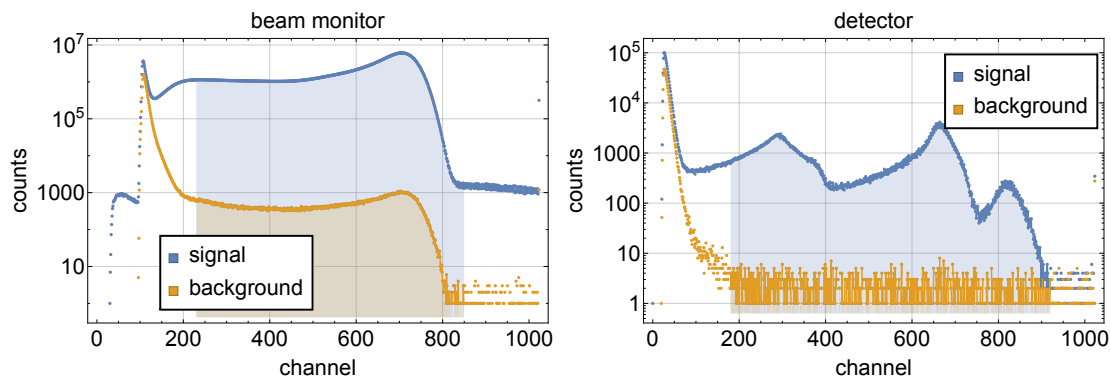


Figure 3.20: Beam monitor and detector spectra. *Left:* The upper (lower) points show the spectrum of the signal (background). The signal follows a typical ${}^3\text{He}$ detector spectrum. The background shows the same characteristics as the signal as the background of the beam monitor is dominated by neutrons. *Right:* The upper (lower) points show the signal (background) of the detector. The first and second peak are not well separated and originate from Li-ions, produced after neutron capture. The third and fourth peak are due to α -particles. The areas under the peaks correspond to the different channel probabilities. The spike at lower channels originates from electronic noise. All spectra are cut below a certain threshold by hardware to ignore electronic noise. The shaded areas indicate the regions of interest: (230-850) for the beam monitor and (180-920) for the detector.

The count rate of the beam monitor is used for normalisation of the recorded count rate from our detector. The background of the beam monitor is neutron dominated, because of its exposed position closer to the reactor core, where shielding is more difficult. In contrast for the detector, the characteristic α and Li peaks cannot be clearly seen, which demonstrates sufficient shielding.

The multi-channel analyser records both, the detector and the beam monitor, and produces a histogram over 1024 channels each. Only the events within specific channels, defined by the region of interest (ROI) are taken, all others are rejected as they are dominated by electronic and other noise sources. The region of interest is chosen such that the signal-to-noise ratio (SNR) is maximized while ensuring a sufficiently large number of events. The chosen ROI of (230-850) for the beam monitor results in a SNR of 3576 over all measurements. For the detector with the ROI of (180-920) the SNR of 18.77 was achieved for measurements where no oscillation was applied in region II. During measurements upon resonance for the $|1\rangle \leftrightarrow |3\rangle$ transition with oscillation strength corresponding to a π -flip (where the signal is expected to drop significantly, see figure 4.3), the SNR was still 4.32 and for the $|1\rangle \leftrightarrow |4\rangle$ transition 2.64. This emphasises the importance of a background-optimized detector concept, which was improved iteratively [Thalhammer, 2013].

Temporal stability of spectra

The spectrum of the detector was stable during the whole experiment. As the ROI for the detector is chosen to be at channel regions with minimal counts, shifts of the spectrum have very little influence on the total neutron count within the ROI. However,

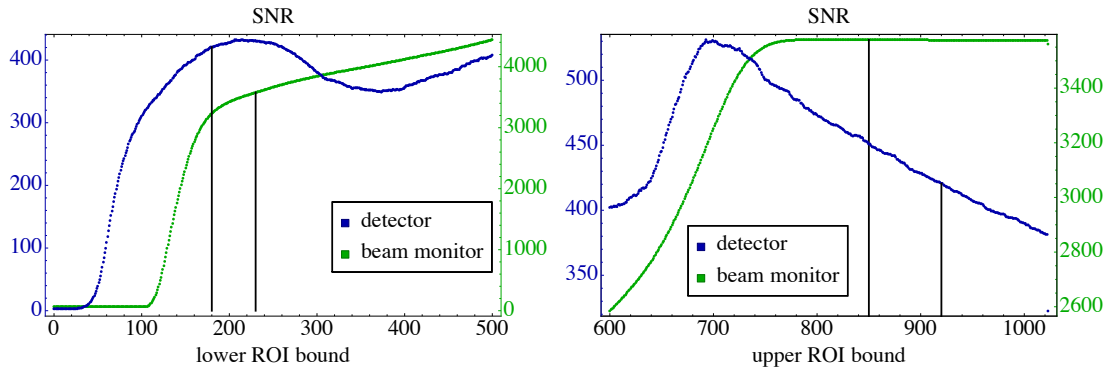


Figure 3.21: Signal-to-noise ratio (SNR) for the beam monitor and the detector as a function of the lower (upper) ROI bound shown in the *left* (*right*) figure. In each figure the detector is shown in blue with the left axis whereas the beam monitor is shown in green and the corresponding right axis. It is interesting to compare the structure of the SNR with the spectra shown in 3.20. The black lines indicate the chosen ROI bounds: (230-850) for the beam monitor and (180-920) for the detector. The upper ROI bound of the detector is chosen such as to include both α -peaks.

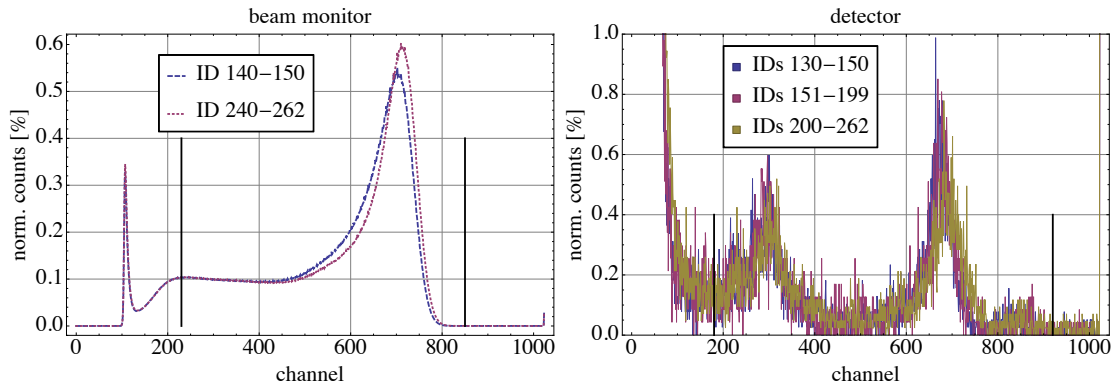


Figure 3.22: Beam monitor (*left*) and detector (*right*) spectra comparisons. A change of the spectrum where the peak shifts to higher channels with increasing measurement IDs is visible for the beam monitor. The detector spectrum however remains stable over time.

the time stability of the beam monitor was subject to slight variations. Figure 3.22 shows the combined and normalised spectra of the measurement IDs 140-150 and 240-262. A clear shift of the spectrum is observed. In general, there are two typical effects that can influence the spectrum: first the whole spectrum can shift owing to fluctuations of the base voltage and second the spectrum can scale due to a non constant high-voltage supply. To quantify the behaviour, the peak was fitted with a Gauss-shape to determine the peak position for each measurement. Together with the fitted rising edge of the spectra the two cases can be distinguished. Figure 3.23 shows the fitted peak and edge channels P_N , E_N compared to the original positions P_0 and E_0 as well as the resulting width of the spectrum. The final rates were obtained with the new ROI_N :

$$ROI_N = P_N + (ROI_0 - P_0) \frac{P_F - E_F}{P_0 - E_0} \quad (3.14)$$

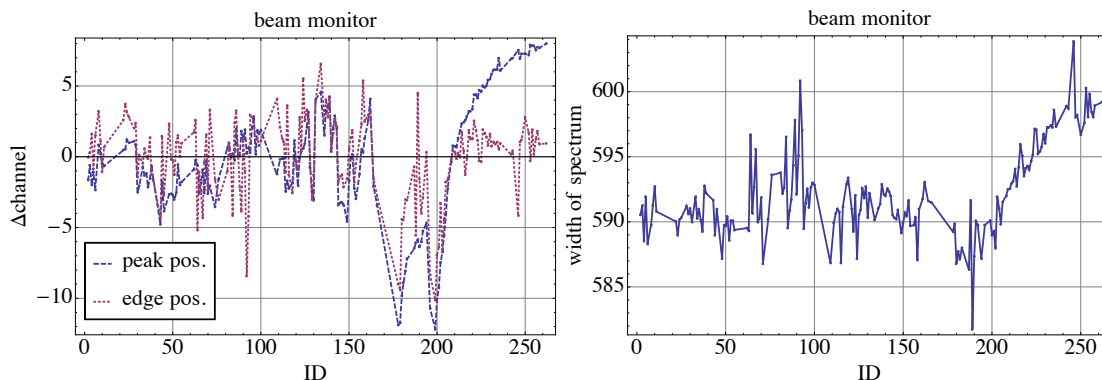


Figure 3.23: *Left*: Stability of the peak and edge position of the beam monitor displayed over the measurement ID. *Right*: The resulting number of channels in the region of interest. Towards higher IDs a scaling is visible.

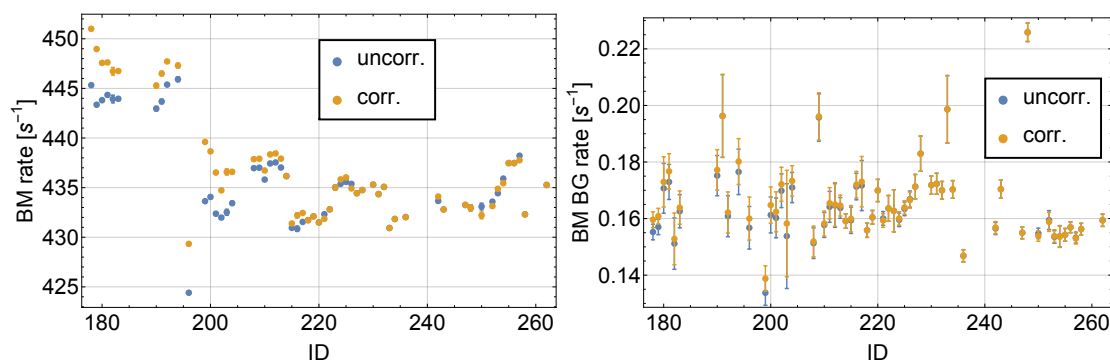


Figure 3.24: The raw and the spectrum-shifting corrected beam monitor rate (*left*) and the beam monitor background rate (*right*) over the measurement ID. Between the IDs 194 and 195, a reactor shut-down with a fuel element change took place, the beam monitor rate was lower afterwards.

The beam-monitor (background) count rates were corrected for this effect. After correction the beam monitor indicated a neutron flux change of $< \pm 1.2\%$ during the measurements in cycle 4 and $< \pm 0.8\%$ during cycle 3.

Linearity of the beam monitor The implemented measurement scheme counts surviving neutrons at different times, so it is sensitive to the initial flux entering the setup. The purpose of the beam monitor is to give a measure of the incoming neutron flux. Ideally the beam monitor behaves linearly to the incoming flux. A measurement series was performed where the incoming flux was controlled by the adjustable opening of an upstream shutter. The recorded rate of the beam monitor was compared to the signal seen by the detector placed directly behind the collimating plates inside the main experimental vacuum chamber. For high count rates of the beam monitor (above 350 s^{-1}), the ratio of the detector and beam monitor showed the desired constant behaviour (see figure 3.25). This justifies the normalisation of the detector rate with respect to the beam monitor rate.

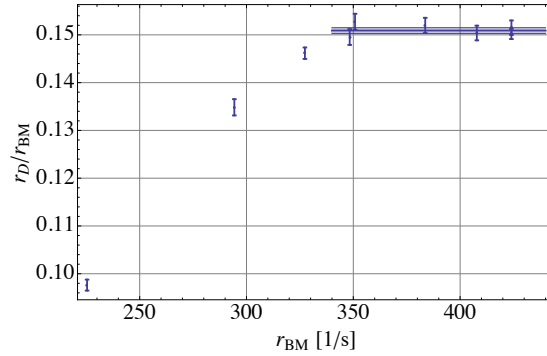


Figure 3.25: The dependence of the detector signal as a function of the beam-monitor rate. For high beam-monitor rates the behaviour is constant. The ratio of the detector and beam monitor rates r_D and r_{BM} saturates for $r_{BM} > 350 \text{ s}^{-1}$ at $(15.09 \pm 0.06) \%$ with a compatibility of 69%.

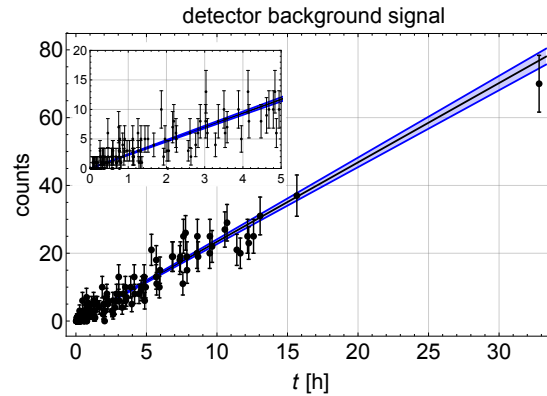


Figure 3.26: All individual background measurements plotted over their duration. The fitted curve gives the rate $r_{BG} = (641 \pm 17) \times 10^{-6} \text{ s}^{-1}$.

Determination of background

The background of the detector was determined in separate measurements. Additionally we utilized a particularity of the PF2 platform. The neutron beam on the PF2 platform is shared alternately among up to three experiments, so the waiting times between beam allocations were used for additional background-rate measurements. To achieve low background rates, extensive shielding of both the detector as well as the experiment with B_4C were employed. The beam-monitor (background) rate was determined for each measurement separately, as they have high enough count rates. The beam monitor rate was around 435 s^{-1} , its background was in the order of 0.16 s^{-1} . The very small detector background rate can only be determined over the duration of the whole experiment. After a total time of 616 hours it is found to be $r_{BG} = (641 \pm 17) \times 10^{-6} \text{ s}^{-1}$ (see figure 3.26). With the beam-monitor (background) rate r_{BM} ($r_{BM,BG}$) and the detector background rate r_{BG} , the corrected rate r_C for each measurement can be determined from the recorded rate r of the detector:

$$r_C = \frac{r - r_{BG}}{r_{BM} - r_{BM,BG}}.$$

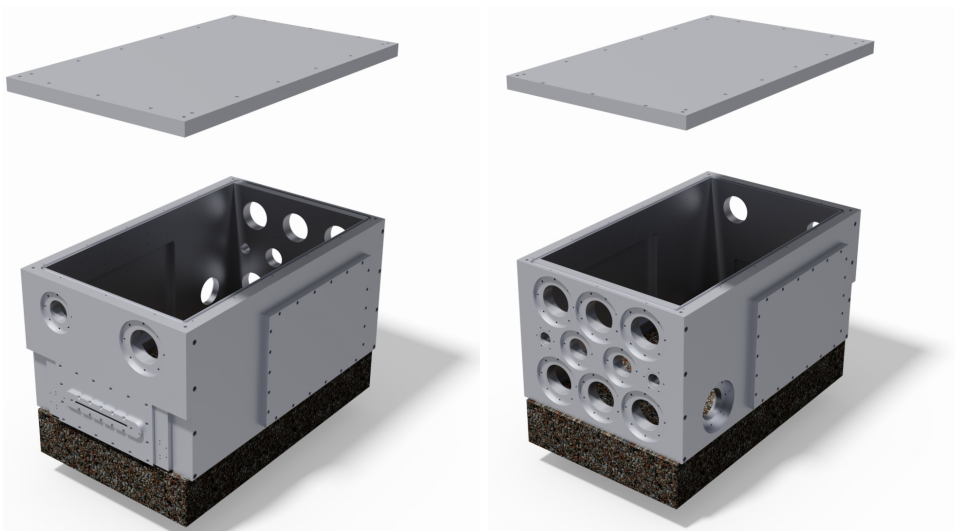


Figure 3.27: The vacuum chamber designed for the experiments since 2010 as seen from the front (*left*) and back (*right*). The vacuum chamber is placed on a granite and has a lid, which is removable by crane. The entrance slit for the neutrons, which resembles a mouth can be seen in the left figure. The feed-throughs on the front side are used for the vacuum components, the feed-throughs on the rear are for electronic components like high-voltage for the detector, control of the devices etc.

3.1.6 Vacuum chamber

UCNs have a short mean free path length $x_M \lesssim 14$ cm in air at ambient pressure. This is owed to the fact that the absorption cross section scales inversely with the velocity:

$$\sigma \propto \frac{1}{v}. \quad (3.15)$$

To obtain a sufficiently high neutron count rate, the experiment has to be performed in vacuum. As the experiment has grown in complexity and also in size at the same time, the previously existing vacuum chamber had to be replaced. During the course of this thesis a new vacuum chamber was constructed and built. Its inner dimensions are $905 \text{ mm} \times 530 \text{ mm} \times 480 \text{ mm}$, which corresponds to a volume $> 225 \text{ l}$. This vacuum chamber was used for the beam times *3-14-283*, *DIR-94*, *3-14-305*, *3-14-314* and *3-14-331*.

The vacuum chamber is placed on top of the granite, which acts as the bottom of the vacuum chamber (see figure 3.27). The lid is removable by crane. The sealing is done with O-rings. Each side has at least one flange, the back features multiple for feed-throughs, which are for pumping the vacuum, electronic connectors for the devices inside, laser and gas feed-throughs. A thin AlMg3-foil at the front allows the neutrons to enter.

The design was adapted from the previous vacuum chamber. The program CATIA⁸ was used for the creation of plans. Two chambers, one out of stainless steel, one of

⁸Proprietary software of Dassault Systemes

aluminium were built. Only the latter was used in the experiment to avoid any magnetic stray fields. The vacuum chamber also houses the velocity selector. Up to beam time *3-14-305*, the previously existing selector was used. Since then a newly designed selector was used, which was placed in a front-side extension to facilitate the larger 3-part setup. The redesigned selector with the extension were designed during a master thesis [Bittner, 2013]. The vacuum chamber was pumped by an oil-free turbomolecular pump from *Pfeiffer Vacuum*. The leak rate for the empty vacuum chamber was $(1.7 \pm 0.3) \times 10^{-6}$ mbar m³ s⁻¹ [Jung, 2013]. With the fully equipped vacuum chamber a pressure of $\sim 1 \times 10^{-4}$ mbar was achieved. The neutron loss due to absorption is thus negligible.

The vacuum pressure is also of physical significance when studying new forces like chameleons. If such a new short-range force interacts with the residual gas, effects need to be considered. For example, the hypothetical chameleon might get screened by gas inside the vacuum chamber. For a detailed discussion see section 5.4.

Upcoming experiments with increasing length will require a new vacuum chamber which will also house the granite and multiple layers of μ -metal.

3.1.7 Magnetic shielding

The neutron has a magnetic moment $\mu = -60.3 \text{ neV T}^{-1}$ which is three orders of magnitude smaller than for atoms (see table 2.1) which leads to a potential energy in a magnetic field:

$$V = -\mu B. \quad (3.16)$$

Gradients of magnetic fields would lead to an additional force on the neutron, thus it is necessary to shield the experiment from magnetic fields to allow for high-precision measurements.

On the sides of the vacuum chamber, as well as above and below, 1 mm thick μ -metal shields were mounted to ensure a magnetic field at the setup below 15 nT. The magnetic field was measured by the 3-axis magnetic field sensor FLC3-70 from the company Stefan Mayer Instruments⁹. The fluxgate sensor was situated below a translation stage, a few centimetres above the neutron mirror surface, left of the beam path. With the translation stage it could be moved parallel along the neutron's flight direction. It has a measurement range of $\pm 200 \mu\text{T}$ and was read out continuously.

The materials used for the different parts of the setup were selected on their magnetic properties, only non-magnetic and non-magnetisable materials were used. The component with the highest magnetic field was the translation stage.

Figure 3.28 shows the time stability of the magnetic field and the gradient along the neutron's flight path. Only the gradient along the neutron's flight path of the vertical magnetic field B_z is crucial as it leads to an additional acceleration. As the sensor's round geometry made its alignment difficult, the gradient of the total field is considered here. In the given case, where the different field components are not anti-correlated this is a very conservative approach as it overestimates the effect. The additional acceleration can be estimated from the magnetic field change $\Delta B = 11 \text{ nT}$ over the measurement

⁹<http://www.stefan-mayer.com>

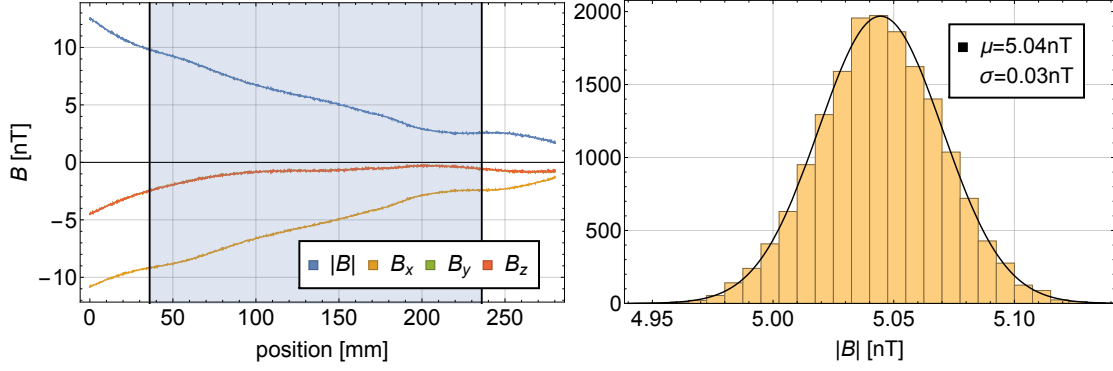


Figure 3.28: Magnetic field measurements. *Left*: The magnetic field above the neutron mirror along the flight direction of the neutrons. The shaded area indicates region II, on its left is region I. *Right*: A histogram of the magnetic field’s magnitude at a fixed position over the duration of a measurement.

length $\Delta x = 280$ mm:

$$\frac{\Delta a_{\text{mag}}}{g} = -\frac{\mu}{gm_N} \frac{\Delta B}{\Delta x} = -2 \times 10^{-8}. \quad (3.17)$$

3.1.8 External systematics

Linearisation of potential

The linearisation of the gravity potential shown in equation 2.2 is the result of an expansion around the Earth’s radius r_\oplus :

$$\begin{aligned} V(r) &= G \frac{M_\oplus m_N}{r} \\ &= G \frac{M_\oplus m_N}{r_\oplus} \left(2 - \frac{r}{r_\oplus} \right) + \mathcal{O}(r - r_\oplus)^2 \\ &= V_0 + m_N g z + \mathcal{O}(z)^2, \quad \text{with } g = -G \frac{M_\oplus}{r_\oplus^2}, \quad z = r - r_\oplus, \end{aligned} \quad (3.18)$$

with the Earth’s and neutron masses M_\oplus and m_N . The deviation of the linearised potential from the true potential accumulates to $\Delta V = 1.5 \times 10^{-11}$ peV at a height of $l = 30 \mu\text{m}$. To first order perturbation theory, the first four eigen energies are shifted by $(2 \times 10^{-12}$ to $2 \times 10^{-11})$ peV:

$$\Delta E_n = -G \frac{M_\oplus m_N}{r^3} \langle \psi_n | z^2 | \psi_n \rangle. \quad (3.19)$$

As we are far from such an accuracy the linearisation is justified.

Tidal effects

The moon on its orbit around the Earth modifies the local value of g by its gravitational attraction. The maximal deviations are observed when the moon is the closest and the

furthest away respectively:

$$g'_{\zeta} = \pm \frac{GM_{\zeta}}{(d_{\zeta} \pm r_{\oplus})^2}. \quad (3.20)$$

This results in a relative change $\frac{g'_{\zeta}}{g} = -3.5 \times 10^{-6}$ to 3.3×10^{-6} . Additionally the Earth revolves in 27 days around the centre of mass which is located roughly 1680 km below the surface. The centrifugal force from this motion is directed away from the moon along the axis containing the mass centres of Earth and moon for every point on the Earth and leads to an acceleration $\frac{g''_{\zeta}}{g} = 3.4 \times 10^{-6}$. This effect counteracts the gravitational pull of the moon. The net effect of the moon gives $\frac{g_{\zeta}}{g} = -9.9 \times 10^{-8}$ to 1.2×10^{-7} .

The sensitivity on the i -th state is given by

$$\delta E_i = \frac{\partial}{\partial g} E_0(g) \text{AiZero}(i) \delta g, \quad (3.21)$$

with $E_0(g) = \sqrt[3]{\frac{\hbar^2 m_N g^2}{2}}$ from equation 2.6. The first four states have a sensitivity of $(2.1 \times 10^{-7}$ to $6.1 \times 10^{-7})$ peV.

The same is true for the sun on its diurnal path across the sky. Using equation 3.20 with the sun mass M_{\odot} and distance d_{\odot} shows that the effect from the gravitational pull is of order $\frac{g'_{\odot}}{g} = \pm 6.0 \times 10^{-4}$ while the centrifugal force is $\frac{g''_{\odot}}{g} = \mp 6.0 \times 10^{-4}$ resulting in a total effect $\frac{g_{\odot}}{g} = -5.6 \times 10^{-8}$ to 4.7×10^{-8} . This leads to a sensitivity of $(9.7 \times 10^{-8}$ to $2.8 \times 10^{-7})$ peV for the first four states.

Coriolis force

The laboratory is no inertial frame as (among other things) the Earth rotates around its axis. Thus, in the laboratory reference frame pseudo forces like the Coriolis force F_{Cor} appear. The Coriolis force couples the horizontal and vertical degrees of freedom. It depends on Earth's angular velocity ω_{\oplus} and the flight direction of the neutron v_N :

$$\vec{F}_{\text{Cor}} = -2m_N \vec{\omega}_{\oplus} \times \vec{v}_N. \quad (3.22)$$

Equation 3.22 shows that only the component normal to the Earth's rotation axis contributes. The neutron, flying horizontally in the laboratory system with roughly $v = 8 \text{ m s}^{-1}$ in Grenoble at a latitude of 45° , feels a maximal additional acceleration $\frac{a_{\text{Cor}}}{g} = 8.4 \times 10^{-5}$. The energy of the first four states is thus shifted by $(7.9 \times 10^{-5}$ to $2.3 \times 10^{-4})$ peV. The effect can be corrected for, a 2 degrees orientation uncertainty at a north-west alignment of the experiment leads to a maximal uncertainty of 2×10^{-6} peV.

External mass distribution

Surrounding masses also modify the local acceleration felt by the neutron. For example the mirror on above the neutron in region I and III counteracts Earth's gravity. The mirror has a density $\rho = 2.5 \text{ g cm}^{-3}$ and let us assume the dimensions $l_x, l_y, l_z = (200 \times 200 \times 35)$ mm. Treating the potential created from the mirror as a perturbation, the

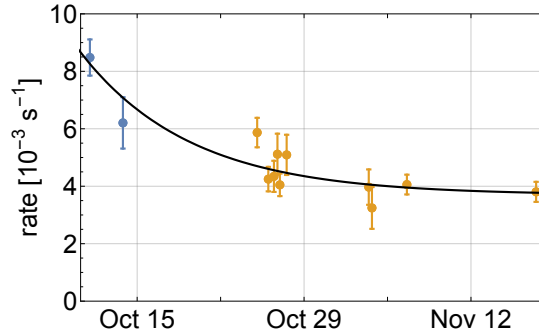


Figure 3.29: The observed drop of the transmission rate over time when no oscillation was applied. The two measurement subsets, one before and one after the reactor shut down are plotted in blue and orange. The black line shows the time behaviour of the rate $A(t)$ with an exponential dependency.

energy shift can be calculated with the overlap of the potential, generated by the neutron mirror, with the wave function:

$$\begin{aligned} \Delta E_n &= \langle \psi_n | V(z) | \psi_n \rangle \\ &= G\rho m_N \int_{z=0}^{\infty} \int_{l_z} \int_{l_y} \int_{l_x} \psi_n^*(z) \frac{1}{r} \psi_n(z) dl_x dl_y dl_z dz. \end{aligned} \quad (3.23)$$

The energy shift for the ground state, which is closest to the mirror is $\Delta E_1 = 4.5 \times 10^{-8}$ peV.

Effect	Influence	Effect	Influence
Coriolis force	2.3×10^{-4} peV	mirror mass	$\leq 4.5 \times 10^{-8}$ peV
Moon	$\leq 6 \times 10^{-7}$ peV	Linearisation	1.5×10^{-11} peV
Sun	$\leq 3 \times 10^{-7}$ peV		

Table 3.3: Overview of systematic effects. The effects can be ignored as we cannot resolve them with our current sensitivity. For an improved GRS setup they will have to be considered.

Outlook

Currently, the effects presented herein can be neglected as the experiment is mainly limited by statistics due to the low count rates. Future realisations of GRS with improved count rates and/or new setups will need to address these systematics and correct for them. Future experiments will allow to group the data according to the sidereal day and to address a whole new range of questions. By seeing effects from other celestial bodies, the probing range will increase from micrometer to AU and maybe beyond. If increased sensitivity allows to determine the attraction to the centre of the galaxy, it is expected that part of it should be attributed to dark matter [Stubbs, 1993] as the relative dark matter content increases with scale.

3.1.9 Null rate stability

The neutron flux was measured repeatedly when no oscillation was driven. Over the time of the experiment, a degradation of this transmission rate was observed. The behaviour of transmission rate over time can be seen in figure 3.29. Small neutron flux variations are normal at a neutron source like the ILL (see section 3.1.5), however for this significant change, the definite origin is unknown. As the behaviour is not seen with a simplified 1-part Rabi setup, it is likely that depositions like dust have accumulated on region II over time as there is no protecting mirror above the surface. To test this hypothesis, the vacuum chamber was opened after the measurements and the surface of the mirror in region II was carefully cleaned. An ensuing measurement without driven oscillation exhibited an increased count-rate. As no time for further investigations was available, no conclusive explanation for the behaviour can be given. The next generation of the experiment will feature a protection against unwanted depositions.

The measurements extended over the two reactor cycles 167 and 168, in between was a reactor halt for ten days. For the analysis we group the measurements into two subsets, according to the cycles.

To study the effect, various time dependent behaviours were tested on their compatibility with the data points where no oscillation was applied. The expected constant rate r_0 was multiplied by a time dependent function $A(t)$ to match the recorded rate $r = A(t)r_0$. The compatibility of the following models can be seen in table 3.4.

Constant Choosing $A(t) = A_0$ as constant over time is not compatible with all measurements, it is labelled *const. I* in the results table 3.4. Even two individual constant rates for each of the two subsets are not compatible (labelled *const. II*).

Linear drop The next to simplest approach is a linear time dependency $A(t) = A_0 - c_0t$. Still, the model does not explain the behaviour sufficiently.

Quadratic and higher orders The next polynomial order, a quadratic term is tested: $A(t) = A_0 + c_0t^2$. Still the compatibility is not high enough. Even increasing the order of the polynomial up to four does not give satisfying results.

Exponential drop The model of exponential dampening of the rate uses the form $A(t) = c \exp^{-kt} + A_0$. This model describes the data best and is used in the data evaluation in section 4.1. There the correction is applied to all data points. The measurements in the two subgroups can now be treated on the same footing, a separation is not needed. The fitted curve is shown in figure 3.29.

Future realisation of GRS will include an additional setup protection against dust deposition from the top.

$A(t)$	const. I	const. II	linear	quadratic	exponential
# parameters	1	2	2	2	3
reduced χ_{red}^2	5.75	2.16	3.06	1.57	1.26
Probability	2×10^{-7}	2.8×10^{-2}	7×10^{-4}	7.2×10^{-2}	2.5×10^{-1}

Table 3.4: Compatibility of various time-dependent corrections with the measured data sets to describe the observed rate dampening throughout the cycles 167 and 168.

Chapter 4

Data analysis

With the gravity resonance spectroscopy setup, 58 measurements were performed, 13 of them without any driving oscillation. 5245 neutrons were detected during 355.6 hours.

4.1 Fit function and its parameters

The count rate of the detector and the beam monitor as well as their background count rates were used as input of the experiment. The function r used to describe the measured data is based on the theoretical function $P(A_v, \nu)$ which models Rabi transitions between the states $|1\rangle \leftrightarrow |3\rangle$ and $|1\rangle \leftrightarrow |4\rangle$ as explained in section 2.3. It also contains a time dependent part $A(t)$ which is motivated by the discussion in section 3.1.9.

$$r(t_L, A_v, \nu) = A(t_L)P(A_v, \nu). \quad (4.1)$$

The varying parameter controlled in the experiment were the applied frequency in region II, the oscillation strength and additionally time and date.

The Rabi transition curve which was presented in equation 2.19 reads:

$$P(A_v, \nu) = 1 - c_{13} \left(\frac{\Omega_{R,13}}{\Omega_{RS,13}} \right)^2 \sin^2(\Omega_{RS,13}t/2) - c_{14} \left(\frac{\Omega_{R,14}}{\Omega_{RS,14}} \right)^2 \sin^2(\Omega_{RS,14}t/2). \quad (4.2)$$

The Rabi frequencies $\Omega_{R,ij}$ are a function of the local acceleration g and the oscillation strength A_v . This dependency is inherited by Ω_{RS} , which additionally depends on the oscillation frequency ν . We thus have two input parameter A_v and ν for the Rabi function and four parameters to be determined by the fit: the local acceleration g , the contrasts c_{13} and c_{14} as well as the duration t of the interaction.

Temporal damping of all measurements Motivated by the discussion in section 3.1.9 the term $A(t)$ was introduced to attribute for the observed null rate decay. By using the form presented in equation 4.1, all measurement points are subject to the time-dependent correction. As section 3.1.9 suggests, an exponential dependency on the time was chosen:

$$A(t_L) = A_d \exp^{-(t_L - t_0)\tau} + o, \quad (4.3)$$

where t_L is the laboratory time, t_0 is a chosen time reference. o is the rate that will be approached finally. The rate A_d and the inverse time τ are describing the observed decay.

Parameters Three variables are varied throughout the experiment and used as an input for the fit. These are the laboratory time t_L necessary for the rate dampening as well as the applied oscillation frequency ν and oscillation strength A_ν for the transition curve. A non-linear model fit then determines the most likely parameters of which our model has seven.

Fit results The parameters obtained by a fit with the least-square method are presented in table 4.1. The fit with 7 parameters and 56 data points leads to a χ^2 of 70 and a reduced χ^2_{red} of 1.43. The errors of the parameters were obtained by mapping the χ^2 neighbourhood around each parameter. For this, a parameter is stepwise in- or decreased while a new set of the other parameters is found that minimises χ^2 . From the obtained grid, the error of the considered parameter is obtained for which χ^2 is increased by 1. This determines the statistical 1- σ error. The method is chosen to obtain errors comparable with other groups using the same method. The asymmetric χ^2 -environment for two exemplary parameters is shown in figure 4.1. The correlation between the parameters can be seen in figure 4.2. It is important to note that the correlation of g with all other parameters is below 18%.

parameter	g	c_{13}	c_{14}	t
	local acceleration	contrast $ 1\rangle \leftrightarrow 3\rangle$	contrast $ 1\rangle \leftrightarrow 4\rangle$	interaction time
best value	$9.844^{+0.035}_{-0.037} \text{m/s}^2$	$43.58^{+0.04}_{-0.04} \%$	$77.99^{+0.08}_{-0.08} \%$	$26.318^{+0.001}_{-0.001} \text{ms}$
parameter	o	A_d	τ	
best value	$3.816^{+0.221}_{-0.310} 10^{-3} \text{s}^{-1}$	$3.076^{+0.331}_{-0.329} 10^{-3} \text{s}^{-1}$	$-13.762^{+0.350}_{-0.347} \text{s}^{-1}$	

Table 4.1: Fit parameters and their statistical 1- σ errors as determined by χ^2 -method for a confidence level of 68%.

The theoretical function plotted with the parameters obtained by this fit are shown in figure 4.3. It is a function of the oscillation frequency and strength. The frequencies of the two transitions $|1\rangle \leftrightarrow |3\rangle$ and $|1\rangle \leftrightarrow |4\rangle$ are $f_{13} = 464.14^{+1.10}_{-1.18} \text{Hz}$ and $f_{14} = 648.80^{+1.54}_{-1.64} \text{Hz}$.

For the resonance frequencies the rate drops upon successful excitation into a higher state. With this experiment, the restoration of a quantum state, a so-called 2π -flip, was observed for the first time in gravity resonance spectroscopy. In previous experiments, the rate only dropped with increasing oscillation strength at the resonance frequencies, due to an additional damping mechanism in the interaction region [Jenke et al., 2011]. Here however, with nearly twice the oscillation strength of a π -flip, the rate was restored to the original value. This shows that the coherence of the state is well preserved.

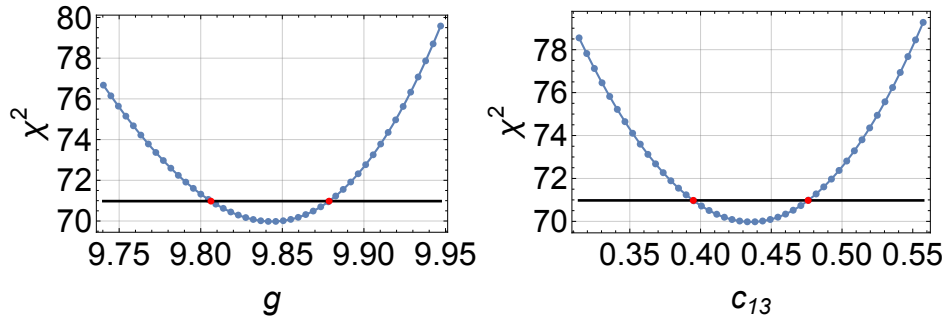


Figure 4.1: The asymmetric χ^2 -environment for the parameter g (left) and c_{13} (right). The χ^2 -values were found by a least-square fit of the other (six) parameters. The values are then interpolated. The bold black line shows $\chi_{\min}^2 + 1$. The red dots determine the asymmetric uncertainties with 68% confidence. The environment of the two parameters is exemplary and look similar for the other parameters.

τ												
A_d						1						
o					-26	88						
t					-27	8	-19					
c_{14}					-58	44	9	36				
c_{13}						-5	25	5	-8	-15		
g							18	11	6	10	6	10
	g	c_{13}	c_{14}	t	o	A_d	τ					

Figure 4.2: The symmetric correlation of the seven fit parameters in percent. Green (red) denotes positive (negative) correlation. The physically interesting parameter g is sufficiently uncorrelated.

4.2 Comparison of different fit hypotheses

Comparison of null rate corrections: For completeness, the fit procedure was repeated for different time-dependent terms $A(t)$. The compatibility of these are presented in table 4.2.

One approach uses only the measurements without driven oscillation to determine the temporal rate dampening. The fit was presented in section 3.1.9. However there are fewer data points that can be used to determine the correction. When the correction is then applied to all data points, the resulting fit procedure gives $\chi^2 = 51$ for the 56 measurements and 5 parameter. The local acceleration yields $g = 9.868^{+0.042}_{-0.047} \text{ms}^{-2}$.

Comparison of transmission functions: Additionally a model was tested, where the two resonance dips were not dependent by a fundamental connection. Instead they are allowed to have completely independent resonance frequencies. This model-independent

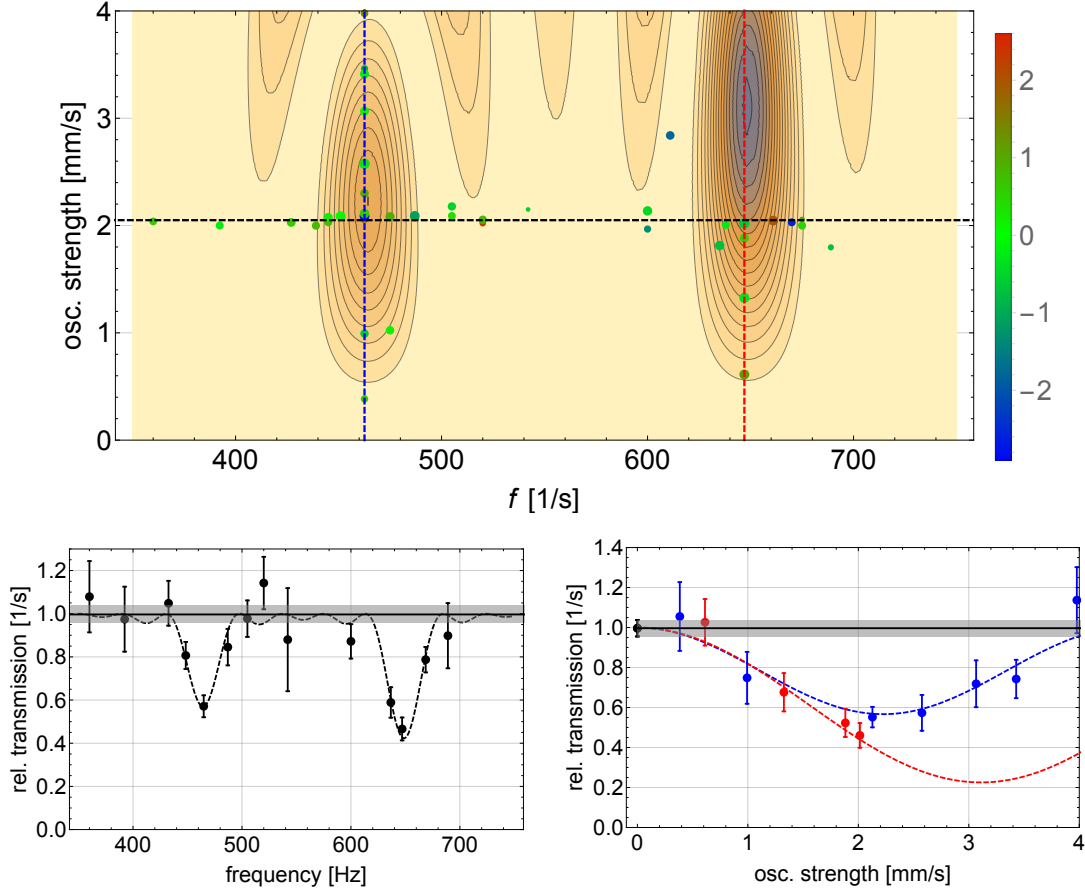


Figure 4.3: *Top*: The contour plot shows the observed transmission rate in dependence of the oscillation strength and amplitude. The plot is normalised to the rate observed without any applied oscillation. The contour surface is the theoretical curve for transitions $|1\rangle \leftrightarrow |3\rangle$ and $|1\rangle \leftrightarrow |4\rangle$ with the parameters obtained by fit. Each dot represents a measurement, its size is inversely proportional to its statistical uncertainty. The colour corresponds to its normalized error with respect to the fitted curve. *Lower left*: The transmission rate in dependence on the oscillation frequency for an oscillation strength of 2.05 mm s^{-1} . The curve is a cut at this strength through the contour plot. Only measurement points within a close oscillation strength are plotted. The data are binned equidistantly with 20 Hz spacing. *Lower right*: The rate in dependence on the oscillation strength for the frequencies 463 Hz and 647 Hz which correspond to the $|1\rangle \leftrightarrow |3\rangle$ and $|1\rangle \leftrightarrow |4\rangle$ transitions. The curves are cuts of constant frequencies in the contour plot. All shown error bars indicate the statistical 1σ error.

approach gave a $\chi^2 = 69.7$ with an additional parameter, in total 8. The resonance frequencies for the two transitions were: $f_{13} = 465.0^{+2.0}_{-2.0}$ Hz and $f_{14} = 648.2^{+2.0}_{-2.3}$ Hz.

Alternatively the connection between the two transitions can be even further relaxed: Allowing transitions their own interaction time results effectively in independent dip widths, expressed by two different interaction times. The reasons for such an assumption could be state dependent horizontal velocities or a mechanism that influences the coupling to the oscillation differently for each state. So far there are no hints pointing towards such effects. Such an approach gives a $\chi^2 = 65.19$ for 9 parameters. The transition

model	$A(t)$ const.	$A(t)$ linear	indep. dips w. fixed width	indep. dips
χ^2	158.7	86.4	69.7	65.2
reduced χ^2_{red}	3.11	1.73	1.45	1.39
g [ms^{-2}]	$9.822^{+0.038}_{-0.042}$	$9.821^{+0.006}_{-0.006}$	$g_{13} = 9.870^{+0.064}_{-0.0637}$ $g_{14} = 9.829^{+0.045}_{-0.052}$	$g_{13} = 9.871^{+0.062}_{-0.063}$ $g_{14} = 9.693^{+0.056}_{-0.054}$

Table 4.2: The (reduced) χ^2 values and the resulting value for the local acceleration obtain by different fit hypotheses. The error corresponds to 68% probability.

frequencies are $f_{13} = 465.0^{+2.0}_{-2.0}$ Hz and $f_{14} = 642.2^{+2.5}_{-2.4}$ Hz. The two interactions times are: $t_{13} = 25.90^{+1.52}_{-1.40}$ ms and $t_{14} = 17.19^{+1.52}_{-1.35}$ ms.

4.3 Conclusions

The results show the successful excitations of the transition $|1\rangle \leftrightarrow |3\rangle$ and for the first time the transition $|1\rangle \leftrightarrow |4\rangle$. Additionally, for the $|1\rangle \leftrightarrow |3\rangle$ a 2π -flip could be observed. This means that the excitation was driven such that the populated third state was emptied again into the ground state and the original state population is restored. This was the first time that such a state restoration was observed with gravity resonance spectroscopy. Additionally, the width of the transitions could be decreased compared to previous realisations owing to the longer interaction region. No decoherence of the states was found with the given sensitivity.

For the further discussion, the following procedure is used: All data are corrected by the exponential time dampening of the rate as discussed in subsection 3.1.9. Each extension of the fit model assumes a fundamental, physical connection between the transitions. Only one universal local acceleration and one universal interaction time is used in the coming models.

Chapter 5

GRS Results

5.1 Determination of the local acceleration

By assuming known inertial and gravitational masses of the neutron, the experiment can serve as a gravimeter with a quantum object which determines the value for the local acceleration g . From the results presented in section 4.1, the experimentally derived local acceleration is $g = 9.844_{-0.037}^{+0.035} \text{m/s}^2$, for which this yields a successful test of Newton's inverse square law at short distances.

5.2 Einstein equivalence principle

The history of the equivalence principle dates back to ancient Greece when Aristotle discussed how objects fall. In his famous *Physics* he states that matter falls according to its mass. But already Philoponus, a philosopher who lived in Alexandria in the 6th century disagreed with Aristotle's view [Rabinowitz, 2007]. The discussion became more substantial when Kepler found a description of the planet movements which did not need their masses. Well known is the test by Galileo by measuring the roll time of marbles on an inclined plane. Newton then provided the theory where the inertial mass m_i , which resists changes of movement and the gravitational mass m_g , which interacts with the gravitational field, are equal.

In classical mechanics all particles in an external gravitational field are subject to the same acceleration if their inertial and gravitational masses are equal which follows from:

$$m_i a = m_g g. \quad (5.1)$$

In the following sections when talking about the gravitational mass, the passive gravitational mass, which couples to an external field, is meant as opposed to the active mass, which generates a gravitational field. This implies that the back action of the test particle mass on the field can be neglected, which is valid for the here discussed scenario of a neutron in the gravity field: if we assume a neutron to be a homogeneous sphere with a radius $r_N = 1 \text{ fm}$ than the gravitational self energy is given by:

$$E_G = -\frac{3}{5} G \frac{m_N^2}{r_N} = -7 \times 10^{-31} \text{ J}. \quad (5.2)$$

5.2.1 General relativity and the Einstein equivalence principle

In general relativity, formulated by Einstein, an observer is unable to distinguish between an accelerated and a free-falling reference frame. This cornerstone of general relativity leads to a geometrical interpretation of gravitation as a metric theory. If the back action of test particle on the space-time geometry is sufficiently small, the equations of motion are independent of masses and each mass follows a geodesic.

The Einstein equivalence principle (EEP) leads to three different hypotheses [Giulini, 2012]: The universality of free fall (UFF) or often called the weak equivalence principle (WEP), the local Lorentz invariance (LLI) and the local position invariance (LPI). While a geometric nature is sufficient to satisfy UFF, a metric theory is needed for EEP. The three hypotheses are of viable theoretical interest. Any violation of them would show the limits in the validity of general relativity and hint to extensions of the theory. For example, time-varying fundamental constants would lead to composition dependent effects and hence to violations of the UFF [Uzan, 2011].

Currently the UFF is the best tested part of this triple, see subsection 5.2.4. The LLI states that local non-gravitational experiments have no preferred space-time direction. It is tested to the level of 10^{-16} [Herrmann et al., 2005]. The LPI is commonly formulated as universality of gravitational redshift (UGR) and universality of clock rates (UCR) which states that travelling different world lines between two events leads to the same red shift and two clocks agree upon travelling the same world line. They are tested to 7×10^{-5} [Vessot et al., 1980] and $(2 \pm 4) \times 10^{-6}$ [Fortier et al., 2007] respectively.

5.2.2 Quantum mechanical tests of EEP

Gravitational effects on a quantum system were demonstrated with neutron interferometry, where two different flight paths in the gravity potential lead to a detectable phase shift dependent on the mass of the neutron [Colella et al., 1975].

Another test is to let slow neutrons fall onto a liquid mirror from a variable height. As long as the kinetic energy gain from the fall is smaller than the Fermi potential of the liquid mirror, the neutron will be reflected of the surface and detected by a counter. While the free fall includes m_g , the Fermi potential depends on m_i (see section 2.1). This yields the inertial mass of the neutron to $m_i = (1 + (1.6 \pm 2.5) \times 10^{-4})m_g$ [Koester, 1976] (but no rigorous test of the equivalence of the two masses). Additional work [Schmiedmayer, 1989] including scattering length determined with other experimental setups, derived the mass ratio $\frac{m_g}{m_i} - 1 = (11 \pm 17) \times 10^{-4}$. However some argue that this test is not purely quantum as only the interaction with the reflecting material is with a quantum description, the free fall itself is in the classical limit [van der Zouw et al., 2000].

5.2.3 The quantum bouncer and universal free fall

[Greenberger, 1968] pointed out an intrinsic difference between GR and quantum mechanics. So while in GR a particles trajectory is independent on the particle's mass by construction using a geometrical structure, it enters in quantum mechanics due to quantization of various quantities. For example, the mass of an electron can be derived from

its allowed orbits around a hydrogen nucleus. This means that quantities which are classically kinematic can become depend on the mass.

Now we revisit the discussion of section 2.2 to introduce rigorously the inertial and gravitational masses. This follows the proposal of [Kajari et al., 2010]. The Schrödinger equation with the potential $V(z) = m_g g z$ takes then the form:

$$\left(-\frac{\hbar^2}{2m_i} \frac{\partial^2}{\partial z^2} + m_g g z\right) \psi_n(z) = E_n \psi_n(z), \quad (5.3)$$

where $g = \frac{GM_\oplus}{R_\oplus^2}$ originates only from the external gravity field. Solving the equation above leads to the energy scale E_0 and length scale z_0 , similar to equations 2.6:

$$E_0 = \sqrt[3]{\frac{\hbar^2 m_g^2 g^2}{2m_i}}, \quad z_0 = \sqrt[3]{\frac{\hbar^2}{2m_i m_g g}}. \quad (5.4)$$

We are now in a situation to have two experimental parameters accessible where the inertial and gravitational mass enter in different relations. While gravity resonance spectroscopy allows precise measurements of E_0 , experiments measuring the time evolution of an UCN wave function after falling down a step provide accurate z_0 values [Jenke et al., 2009].

5.2.4 Limit on the Eötvösh parameter

Typically deviations on the WEP are normally parametrised by the Eötvösh parameter η . It describes the difference of acceleration a of two different test masses A and B , ideally at the same position to be subject to the same gravitational field, with different chemical compositions.

$$\eta = 2 \frac{a_A - a_B}{a_A + a_B}. \quad (5.5)$$

The current limit of UFF, which is obtained by torsion pendulum experiments comparing Beryllium and Titanium is $\eta = (0.8 \pm 1.8) \times 10^{-13}$ [Schlamminger et al., 2008]. As the test masses are macroscopic, this test is purely classical.

With gravity resonance spectroscopy, the Eötvösh parameter can derived from comparing the local acceleration obtained from the transition frequencies and an external classical measurement. The local acceleration g_{spring} was measured at the VCN experiment on the PF2 platform with a spring based WS 410/100 gravimeter. The value $g_{\text{sp}} = (9.80507 \pm 0.00002) \text{ms}^{-2}$ was obtained [Weber, 1998]. The uncertainty of this value originates from the uncertainty of the absolute value measured at a reference point in Grenoble that this relative measurement is referenced to. The uncertainty of the relative measurements are several orders better. Comparing the two acceleration gives the following Eötvösh parameter:

$$\eta = (3.93 \pm 3.80) \times 10^{-3}. \quad (5.6)$$

To put the result in perspective one should not forget that the g_{sp} measurement is nearly 20 years old and was conducted only in rough proximity to the actual GRS location. Over such a time frame it is not possible to reconstruct all potential changes in the

surrounding. This value should hence be seen as a demonstration of the measurement procedure.

Alternatively the local acceleration can be measured by a free-falling corner cube where the reflecting mirror of one arm of a Michelson interferometer is let fallen [Marson & Faller, 1986]. We can express the local acceleration g as function of the value g_{cc} measured by the corner cube with inertial and gravitational masses M_i, M_g :

$$g = \frac{M_i}{M_g} g_{cc}. \quad (5.7)$$

Together with the expression

$$\frac{m_g M_i}{m_i M_g} = \frac{2 + \eta}{2 - \eta} = 1 + \eta + O(\eta^2), \quad (5.8)$$

Equation 5.4 can be rewritten as:

$$E_0 = \sqrt[3]{\frac{\hbar^2 m_i g_{cc}^2}{2}} \left(1 + \frac{2}{3} \eta + O(\eta^2) \right), \quad (5.9)$$

$$z_0 = \sqrt[3]{\frac{\hbar^2}{2 m_i^2 g_{cc}}} \left(1 - \frac{1}{3} \eta + O(\eta^2) \right), \quad (5.10)$$

$$E_0^2 z_0 = \frac{\hbar^2 g_{cc}}{2} \frac{M_i m_g}{M_g m_i} = \frac{\hbar^2 g_{cc}}{2} (1 + \eta + O(\eta^2)). \quad (5.11)$$

Equation 5.11 shows how the Eötvösh parameter can be accessed experimentally to first order without the need of the inertial nor gravitational mass of the neutron by the incorporation of the additional measurement parameter z_0 . The test compares the neutron as a quantum system with the classical corner-cube system.

5.2.5 Determining the neutrons mass

By alternatively arguing that the Eötvösh parameter is tested experimentally to $\eta = (0.8 \pm 1.8) \times 10^{-13}$ [Schlamminger et al., 2008] we can determine the gravitational and inertial mass of the neutron by reformulating equations 5.4 to:

$$m_i = \frac{\hbar^2}{2 E_0 z_0^2}, \quad m_g = \frac{E_0}{g z_0}. \quad (5.12)$$

A combined test of both the energy scale E_0 and the length scale z_0 allows simultaneous determination of the gravitational and inertial masses. Measurements of z_0 have been performed and will be further improved with the qBouncer by either letting neutrons fall of a step of the order of a few tens of microns or recording the spatial height distribution of the neutron. The measurement of E_0 is taken from section 4.

Alternatively instead of z_0 , one can use the inertial mass m_i obtained from other experiments [Mohr et al., 2012] together with the classical g_{sp} value used above. This results in

$$\frac{m_g}{m_i} - 1 = (3.94 \pm 3.82) \times 10^{-3}. \quad (5.13)$$

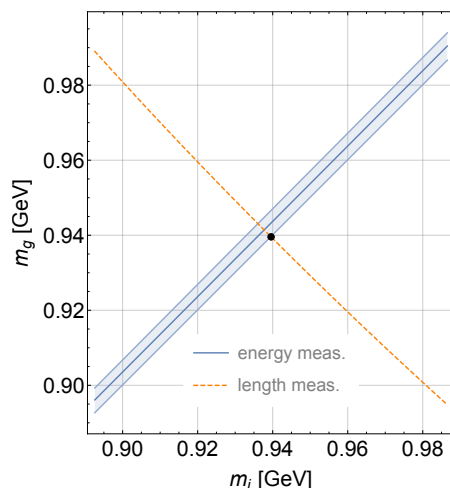


Figure 5.1: The figure shows the gravitational mass of the neutron m_g in dependence of its inertial mass m_i . The blue line represents the value with its $1\text{-}\sigma$ error obtained by combining the measured result from GRS with the classical g measurement. The dashed orange curve indicates the expected value from a length-scale z_0 measurement. The black dot shows the CODATA value for the neutron’s inertial mass [Mohr et al., 2012].

Figure 5.1 shows the experimental bounds in the neutrons gravitational and inertial mass by this experiment combined with a classical g measurement. Future simultaneous determination of the length scale z_0 will add different constraints to determine them both.

5.3 Fifth force constraints

At low energies the effects of new physics can be described by an effective field theory. Typically, to leading order the corrections to the effective potential caused by new physics are Yukawa-like. The resulting potential for two masses M and m with a separation r reads:

$$V(r) = V_N + V_Y = -G \frac{mM}{r} \left(1 + \alpha \exp^{-\frac{|r|}{\lambda}} \right), \quad (5.14)$$

where α describes the strength of the new force compared to the gravitational force and λ is its range. A positive α accounts for an attractive force.

Such deviations can be attributed to almost any hypothetical new fifth force, which is spin-independent. For limits on deviations from spin-dependent forces see [Jenke et al., 2014] and appendix B. One example where such a parametrisation can be used is the model of large extra-dimension. It tries to solve the hierarchy problem and to explain why gravity is so weak compared to other forces [Arkani-Hamed et al., 1998]. According to this theory gravity is diluted into n other dimensions which are compactified at a certain length which is significantly bigger than the Planck length. This would lead to a modified gravitational constant G and effectively change the inverse square law to r^{-2-n} at short enough distances [Arkani-Hamed et al., 1999].

Torsion pendulum experiments can provide limits down to tens of microns [Kapner et al., 2007]. Experiments with cryogenic micro-cantilevers can be used to derive limits

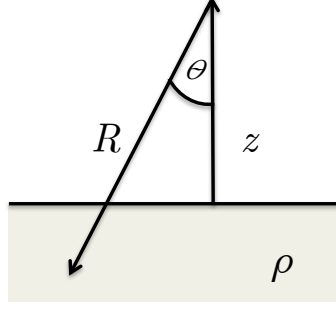


Figure 5.2: The potential at distance z over an infinite half-space of matter with density ρ .

on fifth forces [Smullin et al., 2005, Geraci et al., 2008]: an additional force would alter the oscillation frequency of the cantilever when a source mass is close by ($25 \mu\text{m}$). A force with $|\alpha| > 14000$ for $\lambda = 10 \mu\text{m}$ was excluded. For a range below tens of microns, Casimir force experiments have been used [Lamoreaux, 1997]. Micromechanical torsion oscillators give access to the submicron length scale [Decca et al., 2007]. The best limit in the micrometer range is derived from Casimir force measurements with torsion pendulum [Sushkov et al., 2011]. A more recent detailed overview of current limits can be found in [Antoniadis et al., 2011].

For small ranges λ in the micrometer regime, the q BOUNCE experiment is sensitive to such a coupling [Jenke, 2008] without any masking Casimir force. The additional force that the UCN is subject to, originates from the mirror below with its high matter density. Such a hypothetical force would shift the observed transition frequency. The potential above the mirror is obtained by integrating the contributions of the matter density ρ of the mirror (see figure 5.2):

$$V_Y(z) = -2\pi\alpha G\rho m_N \int_{\theta=0}^{\frac{\pi}{2}} \int_{R=\frac{z}{\cos\theta}}^{\infty} \frac{R^2}{R} \sin\theta \exp^{-\frac{R}{\lambda}} dR d\theta \quad (5.15)$$

$$= -2\pi\alpha G\rho m_N \lambda^2 \exp^{-\frac{z}{\lambda}}, \quad (5.16)$$

with R and θ as integration variables that describe the lower mirror as an infinite half-sphere. This approximation is valid for a small interaction length compared to the dimensions of the mirror $\lambda \ll l_{\text{mirror}}$, due to the exponential decay. This additional potential shifts the energies of the eigenstates. They can be calculated from first order perturbation theory: $\delta E_n = \langle \psi_n | V_Y | \psi_n \rangle$ with the overlap $O_\lambda \propto \langle \psi_n | \exp^{-\frac{R}{\lambda}} | \psi_n \rangle$ shown in table 5.1. The new resonance frequencies f_{ij}^* are given by:

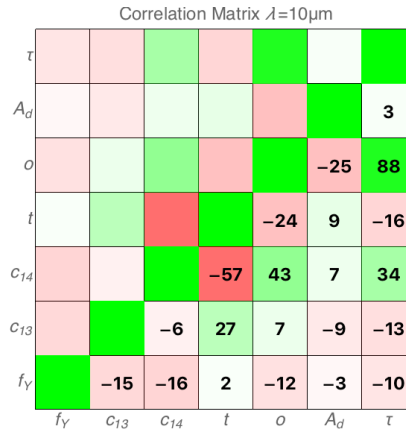
$$f_{ij}^* = (E_{ij} + \delta E_j - \delta E_i) / h = f_{ij} + f_Y \lambda^2 (O_{Yj} - O_{Yi}). \quad (5.17)$$

To obtain limits on the strength α , the data are fitted for the given local acceleration and the parameter $f_Y = 2\pi G\rho m\alpha$ extracted. The resulting limits are shown in figure 5.4 and table 5.2. The correlation between the fitted parameters can be seen in figure 5.3. For the length $\lambda = 10^{-5.25}\text{m} \approx 5.6 \mu\text{m}$, the fit yields an $\alpha = 10^{10.42}$ with a $\chi^2 = 67.90$ for 7 parameters and 56 measurements. From this follows that Yukawa-like forces with $\alpha < -10^{10.93}$ and $\alpha > 10^{11.38}$ respectively can be excluded with a confidence level of 95.45%.

	$n=1$	2	3	4	5
$\lambda = 1 \mu\text{m}$	0.40	0.44	0.46	0.47	0.47
$10^1 \mu\text{m}$	21.27	17.06	14.28	12.45	11.19
$10^2 \mu\text{m}$	44.91	55.11	60.60	64.08	66.42
$10^3 \mu\text{m}$	48.72	63.48	73.26	80.80	87.01

 Table 5.1: Overlap $O_{Y_n}(\lambda)$ with Yukawa-like potential for different states n and λ in percent.

$\log_{10} \lambda [\text{m}]$	-7.5	-7	-6.5	-6	-5.5	-5.25	-5	-4.5	-4	-3.5
$\log_{10} \alpha_+$	24.93	21.44	17.97	14.75	12.28	11.38	10.67	9.67	8.99	8.43
$\log_{10} -\alpha_-$	24.51	21.01	17.54	14.31	11.83	10.93	10.22	9.23	8.56	8.00

 Table 5.2: Limits on a Yukawa-like force with an attractive coupling strength α_+ and with repulsive α_- for various lengths λ (95% C.L.).

 Figure 5.3: The correlations of the fit parameters for a Yukawa potential with $\lambda = 10 \mu\text{m}$ in percent. Green (red) denotes positive (negative) correlation.

The sensitivity of the experiment is dependent on the mass density of mirror, which is $\rho_{\text{BK7}} = 2.51 \text{ g cm}^{-3}$ for our BK7 mirrors. It can be further improved if the mirror is coated with a material of high density, e.g. gold with $\rho_{\text{Au}} = 19.3 \text{ g cm}^{-3}$. As there is an exponential decay of the potential with the distance, the improvement in sensitivity is maximal if the coating thickness d_c is larger than the interaction range $d_c \gg \lambda$. Otherwise equation 5.16 needs to be trivially modified.

5.4 Experimental constraints on chameleon fields

As mentioned in chapter 1 we observe an accelerating expanding universe which is attributed to dark energy. It is often written in the form of a cosmological constant which ironically was originally introduced by Einstein to guarantee a static universe. The nature of dark energy is still unknown today, but there are many potential candidates [Carroll, 2001]. One candidate of particular interest is the so-called chameleon.

So far, no experimental evidence for deviations from general relativity within our

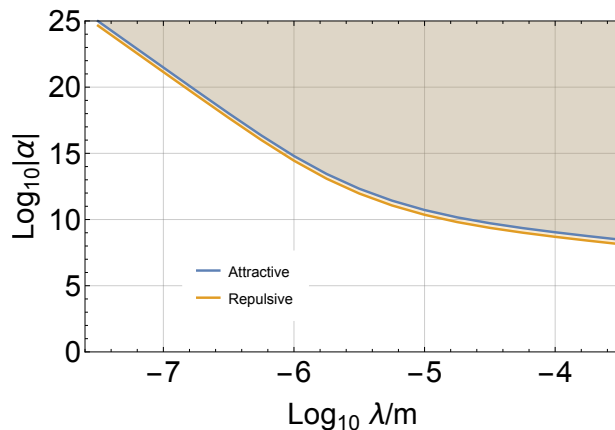


Figure 5.4: The exclusion plot for Yukawa-like forces with strength α dependent on the range λ at a confidence level of 95.54%. The line for an attractive (repulsive) strength with $\alpha > 0$ ($\alpha < 0$) is shown in blue (orange).

solar system was observed and any new theory has to explain both the short as well as the long scale behaviour. The chameleon field provides such a mechanism [Khoury & Weltman, 2004]. It is a scalar field, which has a self interaction and a mass coupling, thus acquiring mass in the vicinity of matter density.

The potential term V is of the run-away type and for a Ratra-Peebles model (with a parameter $n_C > 0$) it is given by:

$$V(\Phi) = \Lambda^4 e^{\Lambda_C^n / \Phi_C^n} \simeq \Lambda^4 + \frac{\Lambda^{4+n_C}}{\Phi^{n_C}}, \quad (5.18)$$

where Λ corresponds the cosmological constant (or the part of it that should be attributed to the chameleon). Together with the interaction term, this potential V leads to an effective potential V_{eff} :

$$V_{\text{eff}}(\Phi) = V(\Phi) + \frac{\beta}{M_{\text{Pl}}} \Phi \rho, \quad (5.19)$$

with the matter density ρ , matter coupling strength β and the Planck mass M_{Pl} . An exemplary potential is plotted in figure 5.5. The minimum of the potential V_{eff} determines the mass of the chameleon, which increases in vicinity of mass and thus leads to an reduced interaction length. Due to this built-in screening mechanism, any matter density suppresses the chameleon field. The chameleon thus hides in most laboratory setups but should affect at cosmological distances. It should be noted that the existence of a chameleon field would violate the weak equivalence principle. So while the chameleon is screened in most laboratory experiments, the neutron is small enough that the chameleon field is not screened. In our experimental setup the chameleon field modifies the gravity potential felt by the neutron [Brax & Pignol, 2011]:

$$V(z) = -mgz + \beta \frac{m}{M_{\text{Pl}}} \Lambda \hbar c \left(\frac{2 + n_C}{\sqrt{2}} z \Lambda \right)^{\frac{2}{2+n_C}}, \quad (5.20)$$

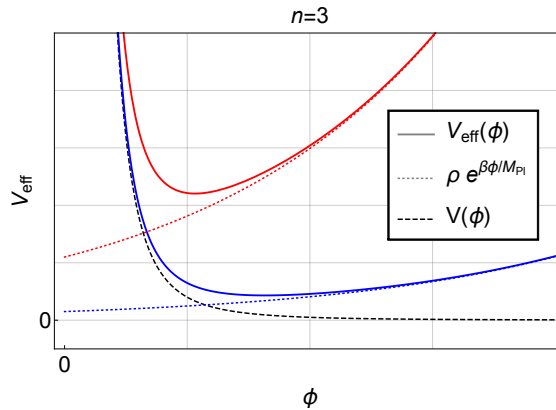


Figure 5.5: The effective chameleon potential (solid line) is composed by the self-interaction (dashed black line) and the matter interaction (dotted line) for a low (blue) and a high (red) matter density ρ . With a high matter density the minimum of the effective potential is found at lower values of Φ corresponding to a higher mass.

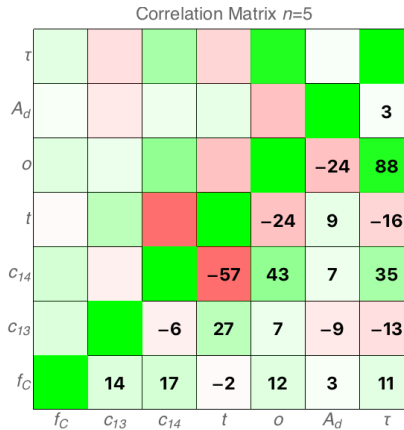


Figure 5.6: The correlations in percent of the fit parameters for a chameleon potential with $n_C = 5$. Green (red) denotes positive (negative) correlation.

where $\overline{M}_{\text{Pl}} = \frac{M_{\text{Pl}}}{\sqrt{8\pi}} = \sqrt{\frac{\hbar c}{8\pi G}}$ is the reduced Planck mass, $\Lambda = 2.4 \text{ meV}$ the cosmological constant. The coupling strength is $\beta > 0$ and n_C is a positive constant. Adding another mirror on top would complicate the solution [Ivanov et al., 2013].

For small potentials the energy shift can be calculated numerically for each state at first order perturbation theory:

$$\delta E_n = \langle \psi_n | V_{\text{Cham}}(z) | \psi_n \rangle, \quad (5.21)$$

$$O_n(\alpha) = \langle \psi_n | z^\alpha | \psi_n \rangle, \quad (5.22)$$

with $\alpha = \frac{2}{2+n_C}$. The overlap O_n increases with the state number n , hence increasing the energy separation between the states. The chameleon is thus expected to increase the frequency of the transition frequency of any two states. The energy difference of any two

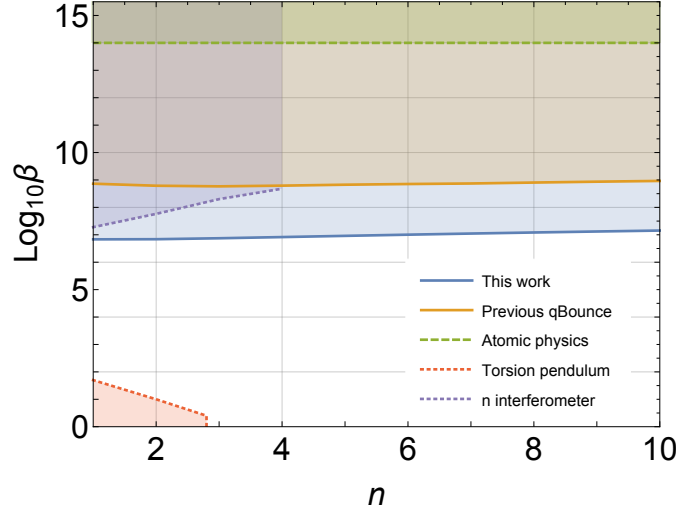


Figure 5.7: Chameleon exclusion plot for the parameter range of β and n . The solid line displays the limit obtained for a confidence level of 95%. The dashed line shows the limit obtained from atomic physics [Brax & Burrage, 2011], the upper solid line the limit previously obtained with GRS in a more compact setup [Jenke et al., 2012]. The purple dashed line is the limit derived with a neutron interferometer [Lemmel et al., 2015]. The lower bound is obtained from torsion pendulum experiments [Adelberger et al., 2009].

states is shifted:

$$E_{ij} = -\sqrt[3]{\frac{\hbar^2 g^2 m}{2}} (\text{AiZero}[j] - \text{AiZero}[i]) + \delta E_j - \delta E_i. \quad (5.23)$$

This energy difference can be calculated and changes the transition frequency $|i\rangle \leftrightarrow |j\rangle$ by:

$$f_{\text{Cham},ij} = \beta \frac{m}{M_{Pl}} \Lambda c \left(\frac{2 + n_C}{\sqrt{2}} \Lambda \right)^{\frac{2}{2+n_C}} \left(\langle \psi_j | z^{\frac{2}{2+n_C}} | \psi_j \rangle - \langle \psi_i | z^{\frac{2}{2+n_C}} | \psi_i \rangle \right). \quad (5.24)$$

This calculation is performed for vacuum but is also valid for in the experiment where we had a pressure of $p = 1 \times 10^{-4}$ mbar. For higher gas pressures the screening by gas molecules has to be considered. A detailed discussion about this topic can be found in [Brax et al., 2013].

The data has been evaluated with the following fit function and a limit on the parameter space β, n_C was obtained. The results can be found in table 5.3. The derived limit, together with limits from other experiments, can be seen in figure 5.7. It shows the chameleon coupling β as a function of the parameter n_C . The correlations between the fit parameters is shown in figure 5.6. The fit for $n = 5$ yields a $\beta = 10^{6.49}$ and gives a $\chi^2 = 67.93$ for 7 parameters and 56 measurements. A coupling strength $\beta > 10^{6.96}$ can be excluded with a confidence level of 95.45%.

As the chameleon is a very prominent candidate, many other experiments are investigating its nature. Another method to search for the chameleon is by looking at its coupling to photons through an afterglow effect [Brax & Burrage, 2010] The experiment CHASE

n_C	1	2	3	4	5	6	7	8	9	10
$\log_{10} \beta$	6.83	6.84	6.87	6.92	6.96	7.00	7.05	7.08	7.12	7.15

Table 5.3: Limits on the chameleon field coupling strength β for various Ratra-Peebles parameter n_C (95% C.L.).

obtained a limit of $\beta_\gamma < 10^{-11}$ with this method [Steffen et al., 2010]. Other limits were obtained by evaluating atomic energy level shifts [Brax & Burrage, 2011]. Until recently most stringent upper limits on the chameleon field were obtained from our previous compact 1-part setup [Jenke et al., 2012]. It also uses GRS which allows a photon-free, direct coupling of the chameleon. However in the previous setup, a second boundary condition imposed by the upper mirror, shifts the energy of the neutron’s states dependent on the slit size between the mirrors. Neutron interferometry with cold neutrons also constrains chameleons [Lemmel et al., 2015]. There, one path of the interferometer leads through a small pressure cell, evacuated to variable degree, where the hypothetical chameleons are not screened in contrast to the other path, which should lead to a measurable phase shift. Recently, new limits from an atom interferometer were derived [Hamilton et al., 2015b]. For $n_C < 3$ there exists also a lower limit on the coupling strength which was obtained from 5th force tests [Adelberger et al., 2009].

Chapter 6

Summary & Outlook

With the setup presented here, the technique of Gravity Resonance Spectroscopy was further improved. The previously limiting systematic factor, an upper mirror in the interaction region could be spared by realising a three-part setup. While being systematically more appealing, it increased the experimental complexity of the experiment. New techniques were incorporated and the setup was modified at many different areas. Additionally the influences of the changed layout were evaluated, like the eigen basis changes between regions, alignment influences and confinement of the oscillation.

With the new setup and the increased interaction time transitions between the states $|1\rangle \leftrightarrow |3\rangle$ and $|1\rangle \leftrightarrow |4\rangle$ could be studied, the latter for the first time in GRS. Another first is the observed state revival of the ground state upon a π -flip for the transition $|1\rangle \leftrightarrow |3\rangle$. Driving the oscillation sufficiently strong the original state population of the first and the excited third state could be restored. The observed energy resolution of these transitions was $\Delta E_{13} = 5 \times 10^{-15}$ eV and $\Delta E_{14} = 7 \times 10^{-15}$ eV (1- σ standard deviation). This is a feature that is only possible with the new three part setup which does not add any dampening in the interaction region (and further improved setups to come in the future). No decoherence of the states was observed with this setup.

With this experiment, the natural length scale E_0 of a gravitationally bound ultra-cold neutron is easily accessible. This allows to study the connection of the local acceleration, the neutrons gravitational and inertial mass and Planck's constant. The measured local acceleration can be compared with the value obtained in a classical measurement to test the weak equivalence principle or to derive the gravitational mass of the neutron. New experiments within the *q*BOUNCE collaboration will further enrich this discussion by determining the natural length scale z_0 with increased precision. Hypothetical deviations of Newton's inverse square law of gravity at the micrometer length scale are of avid interest for the community searching for extensions of the standard model. Such new forces are in the sensitivity range of the experiment and limits for a special parametrisation with the form of a Yukawa-like potential have been derived. Furthermore, the observed transitions were used to derive limits on the scalar chameleon field, a very popular candidate for dark energy. While not the most stringent ones, they are more rigorous than previous limits obtained from neutron physics.

Following the lessons learned from expanding the setup, the next technological leap

lays ahead as the implementation of Gravity Resonance Spectroscopy with a Ramsey-like setup [Ramsey, 1956]. The advantages this step will bring, like self-focussing velocity insensitivity and even longer propagation times, face the challenging task of maintaining the borderline low neutron flux [Abele et al., 2010]. New ultra-cold neutron sources with a higher flux might help to facilitate the external time constrains of this class of experiments. Furthermore, a Ramsey-like setup would also allow, with some modifications, to test the neutrons charge [Durstberger-Rennhofer et al., 2011].

Appendices

Appendix A

Airy functions, their primitives and applications as wave functions

A.1 Airy functions

In this appendix known integrals and expressions [Vallée & Soares, 2004] are applied to the case of a quantum bouncer in a linear potential and expressed as are needed for analytical treatment in this work. The Airy functions Ai and Bi, named after Sir George Biddell Airy, are solutions of the differential equation:

$$y'' = xy. \quad (\text{A.1})$$

The Airy functions Ai and Bi are linearly independent, they are shown in figure A.1. While they are defined for complex arguments, only the case with real arguments is considered in this work. The roots of the Airy functions, denoted by AiZero and BiZero, which are needed for the solution of the Schrödinger equation in section 2.2 cannot be found analytically.

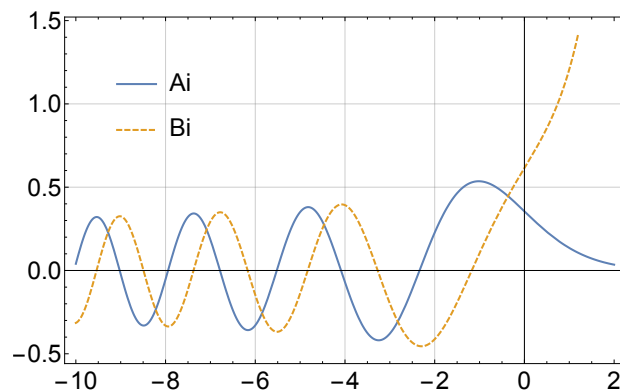


Figure A.1: The Airy functions Ai (Bi) shown as solid (dashed) line. While $\lim_{z \rightarrow \infty} \text{Ai}(z) = 0$, Bi does not converge.

A.2 Overlap of Airy functions

The overlap of different linear combinations A, B of Airy functions Ai and Bi can be calculated by:

$$\int A(\alpha(z + \beta)) B(\alpha(z + \beta)) dz = (z + \beta) A(\alpha(z + \beta)) B(\alpha(z + \beta)) - \frac{1}{\alpha} A'(\alpha(z + \beta)) B'(\alpha(z + \beta)) \quad (\text{A.2})$$

A more general form for different arguments reads:

$$\int A(\alpha(z + \beta_1)) B(\alpha(z + \beta_2)) dz = \frac{1}{\alpha^2(\beta_1 - \beta_2)} \{A'(\alpha(z + \beta_1)) B(\alpha(z + \beta_2)) - A(\alpha(z + \beta_1)) B'(\alpha(z + \beta_2))\} \quad (\text{A.3})$$

A.3 The free wave function

The wave function of a neutron in the gravity field, which fulfils the Schrödinger equation reads:

$$\psi_n(z) = c_n \text{Ai} \left(\frac{z}{z_0} + \text{AiZero}(n) \right), \quad (\text{A.4})$$

where z is the vertical coordinate, z_0 is the length scale that scales the Airy function accordingly to the physical system (see equation 2.5). The wave function of the n -th state is a Airy function shifted by the n -th root. This ensures that the wave function fulfils the boundary condition $\psi(z = 0) = 0$. The eigen energy of the state is given by

$$E_n = -\text{AiZero}(n) \cdot E_0, \quad (\text{A.5})$$

with the energy scale E_0 of the system.

To obtain the normalisation constant c_n in equation A.4, the definite integral given in equation A.2 can be used with the limits $\lim_{z \rightarrow \infty} z \text{Ai}^2(z) = 0$ and $\lim_{z \rightarrow \infty} \text{Ai}'^2(z) = 0$:

$$\int_0^\infty \text{Ai}^2 \left(\frac{z}{z_0} + \text{AiZero}(n) \right) dz = z_0 \text{Ai}'^2(\text{AiZero}(n)). \quad (\text{A.6})$$

Demanding that the wave function squared has to be unity $|\psi_n(z)|^2 = 1$ gives the normalisation constant c_n with dimension $L^{-1/2}$:

$$c_n = 1/\sqrt{z_0 \text{Ai}'^2(\text{AiZero}(n))}. \quad (\text{A.7})$$

A.4 The wave function with upper mirror

When a second mirror at height l confines the neutron from above, an additional boundary condition has to be satisfied $\phi(z = l) = 0$. The wave function of a neutron in the gravity field with an additional boundary condition then reads:

$$\phi_n(z) = a_n \text{Ai} \left(\frac{z}{z_0} - \frac{E'_n}{E_0} \right) + b_n \text{Bi} \left(\frac{z}{z_0} - \frac{E'_n}{E_0} \right). \quad (\text{A.8})$$

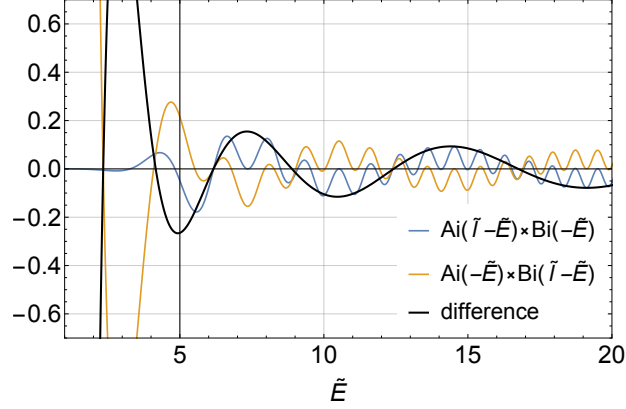


Figure A.2: Energy solutions with additional boundary condition. The left and right hand side are shown in blue and orange for a $\tilde{l} = 5$, which corresponds to a slit height $l = 29.3 \mu\text{m}$. The difference between the two is plotted in black, the roots of this function give the eigen energies $E'_n = \tilde{E}_n E_0$ of the n -th state, the first six can be seen.

The requirement $\phi(z = l) = 0$ gives the connection of the coefficients a_n, b_n :

$$b_n = -a_n \frac{\text{Ai}(-\tilde{E}_n)}{\text{Bi}(-\tilde{E}_n)}, \quad (\text{A.9})$$

with the dimensionless short form $\tilde{E}_n = E'_n/E_0$. The energy E'_n of the n -th state is increase compared to equation A.5, because the wave function is now more confined. To calculate a_n equation A.2 can be used again with $A = B = \phi_n$ and the normalisation condition of the wave function $|\phi_n(z)|^2 = 1$:

$$\begin{aligned} z_0 a_n^{-2} = & (\tilde{l} - \tilde{E}_n) \text{Ai}(\tilde{l} - \tilde{E}_n)^2 - 2 \frac{\text{Ai}(-\tilde{E}_n)}{\text{Bi}(-\tilde{E}_n)} (\tilde{l} - \tilde{E}_n) \text{Ai}(\tilde{l} - \tilde{E}_n) \text{Bi}(\tilde{l} - \tilde{E}_n) \\ & + \tilde{l} \frac{\text{Ai}(-\tilde{E}_n)^2}{\text{Bi}(-\tilde{E}_n)^2} \text{Bi}(\tilde{l} - \tilde{E}_n)^2 + \frac{\text{Ai}(-\tilde{E}_n)^2}{\text{Bi}(-\tilde{E}_n)^2} \left(\text{Bi}'(-\tilde{E}_n)^2 - \tilde{E}_n \text{Bi}(\tilde{l} - \tilde{E}_n)^2 \right) \\ & - \left(\frac{1}{\text{Bi}(-\tilde{E}_n)} \text{Ai}'(\tilde{l} - \tilde{E}_n) - \frac{\text{Ai}(-\tilde{E}_n)}{\text{Bi}(-\tilde{E}_n)^2} \text{Bi}'(\tilde{l} - \tilde{E}_n) \right)^2 \\ & + \text{Ai}'(-\tilde{E}_n)^2 - 2 \frac{\text{Ai}(-\tilde{E}_n)}{\text{Bi}(-\tilde{E}_n)^2} \text{Ai}'(-\tilde{E}_n) \text{Bi}'(-\tilde{E}_n), \quad (\text{A.10}) \end{aligned}$$

with $\tilde{l} = l/z_0$. So the difficult task is to determine the energy E'_n of the n -th eigenstate. As there is no analytical expression, it has to be found numerically by solving the equation:

$$\text{Ai}(\tilde{l} - \tilde{E}_n) \text{Bi}(-\tilde{E}_n) = \text{Bi}(\tilde{l} - \tilde{E}_n) \text{Ai}(-\tilde{E}_n). \quad (\text{A.11})$$

Both sides and their difference can be seen in figure A.2.

A.5 Overlap with partial derivative

The overlap $\langle \psi_n | \partial_z | \psi_m \rangle$ can be calculated with the aid of:

$$\int \text{Ai}(z + \text{AiZero}(i)) \text{Ai}'(z + \text{AiZero}(j)) dz = \frac{\text{Ai}'(\text{AiZero}(i)) \text{Ai}'(\text{AiZero}(j))}{\text{AiZero}(i) - \text{AiZero}(j)}$$

to be:

$$\begin{aligned} \langle \psi_n | \partial_z | \psi_m \rangle &= \int \psi_n^* \left(\frac{z}{z_0} + \text{AiZero}(n) \right) \partial_z \psi_m \left(\frac{z}{z_0} + \text{AiZero}(m) \right) dz \\ &= \frac{1}{z_0 (\text{AiZero}(n) - \text{AiZero}(m))}. \end{aligned} \quad (\text{A.12})$$

A.6 Overlap with position operator

The overlap $\langle \psi_n | z | \psi_n \rangle$ can be calculated with the aid of:

$$\begin{aligned} \int z \text{A}(\alpha(z + \beta)) \text{B}(\alpha(z + \beta)) dz &= \\ \frac{1}{3} (z^2 - z\beta - 2\beta^2) \text{A}(\alpha(z + \beta)) \text{B}(\alpha(z + \beta)) &+ \frac{2\beta - z}{3\alpha} \text{A}'(\alpha(z + \beta)) \text{B}'(\alpha(z + \beta)) \\ + \frac{1}{6\alpha^2} (\text{A}'(\alpha(z + \beta)) \text{B}(\alpha(z + \beta)) &+ \text{A}(\alpha(z + \beta)) \text{B}'(\alpha(z + \beta))) \end{aligned} \quad (\text{A.13})$$

Appendix B

Characterisation of polarisation foil

B.1 Motivation

To search for deviations from gravity which are caused by spin-dependent forces one can make use of the neutron spin. Any spin-coupling field would modify the eigen energies of the gravitational states dependent on their spin orientation. Searches for such a spin-coupling field have been carried out at the Institut Laue-Langevin (ILL) with gravity resonance spectroscopy and derived limits on axion-like particles [Jenke et al., 2014].

Experimental modifications of the setup were required to search for an additional spin-coupling. A magnetic guiding field was installed and the entrance foil of the detector was coated to ensure only one polarisation was able to enter the detector and be recorded. The resonance curve was measured for both spin polarisations by reversing the magnetic field and the polariser. Missing deviations between these measurements lead to limits on spin-coupling fields.

B.2 Characterisation of a polariser

B.2.1 Functioning of the polariser

The polariser is realised by a modification of the detector entrance foil. The entrance foil, separating the vacuum from the detector volume filled with ArCO₂ is coated on the inside with ¹⁰B to convert ultra-cold neutrons into charged particles, see chapter 3.1.5. To allow only one spin orientation to enter the detector, the outside of the foil was coated with soft iron. The coating was done by Th. Lauers group¹. When the soft iron is polarised, the potential V_{\pm} of the material V_{\pm} as seen by each orientation is given by the Fermi potential V_F modified by an additional spin-dependent part (see 2.1):

$$V_{\pm} = V_F \pm \mu B, \quad (\text{B.1})$$

where μ is the UCNs magnetic moment and B the internal magnetic field of the coating. If the neutron spin is anti-/parallel to the foil polarisation, the Fermi potential is in-/decreased. In each case, UCNs can pass the foil only if their velocity exceeds the

¹At the time of testing associated at the Institut für Physik, Universität Mainz, Germany.

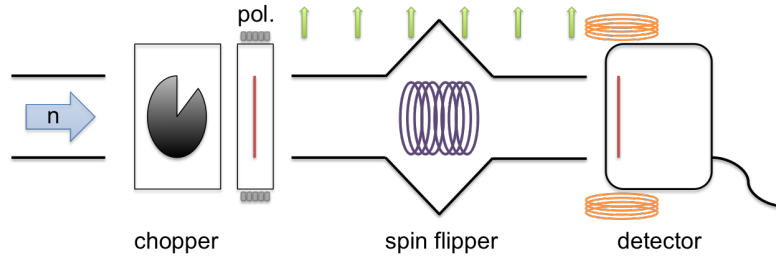


Figure B.1: The experimental setup to characterise the polariser. The neutrons pass first a chopper, which defines the beginning of the TOF distance. They then pass a known polariser. In the following path a spin flipper was placed which could flip the neutron spin. A magnetic holding field is applied over the whole flight distance to preserve the spin orientation. At the end sits the polariser with the iron-coated foil.

critical velocity which is now spin orientation dependent [Golub et al., 1991, Jenke et al., 2013]. To control the polarisation of the foil, two coils in an Helmholtz configuration were installed above and below the detector. For setting the polarisation of the foil, the coils produced a magnetic field of $\pm(5.4 \text{ to } 5.7) \text{ mT}$. During operation a magnetic field of $\pm 1.1 \text{ mT}$ was sufficient to maintain the polarisation. When reversing the polarisation of the foil, the guiding field had to be reversed as well to avoid crossing areas where the magnetic field would vanish.

The presented data were recorded at the ILL during beam time *TEST-2034* with the same detector used for the axion search, to characterise the polarisation foil.

B.2.2 Experimental setup

The experimental setup is shown in figure B.1. As the polarisation capability of the foil is only given for a specific velocity range, its transmittivity was measured as a function of the velocity for each spin orientation. For this, a time-of-flight (TOF) measurement was realised, where the neutron traverses the distance d from the chopper to the polariser in the time $t = d/v$ depending on its velocity v . A time-sensitive detection thus allows for a measurement dependent on the velocity of the neutron. The flight distance was 1643 mm, the chopper frequency was 1.2 Hz. The offset between the triggered signal obtained from the chopper and the actual opening of the slit is a characteristic of each chopper and was in this case 35 ms. A polariser in the flight path defines the neutron polarisation. It is an aluminium foil coated together with the detector foil and thus has the same magnetic properties. Its orientation was determined by conventional neodymium magnets. A static magnetic holding field ensured the conservation of the spin orientation. Additionally a spin flipper was located between the two polarisers. Switching it on and off allowed both spin orientations to arrive at the detector alternately.

B.2.3 Data evaluation

The data were recorded with a multi-channel spectrometer (MCS) which was synchronised with the chopper. The neutron counts were grouped into bins of 1 ms length, the so-called dwell time, and a time histogram was recorded as can be seen in figure B.2.

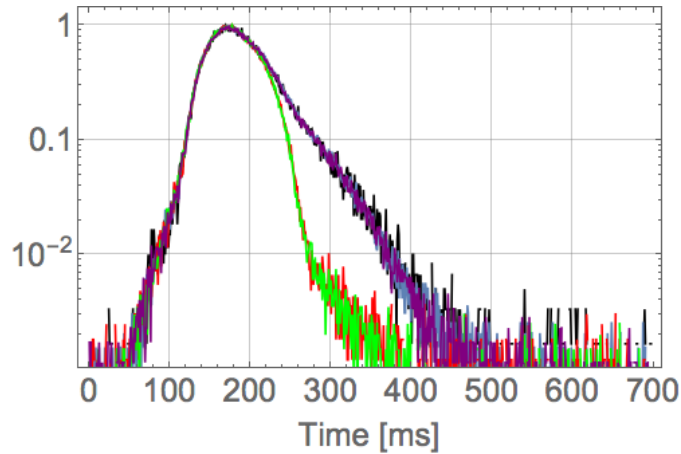


Figure B.2: Time-of-flight measurements of polarised neutrons. The two classes of measurements are visible where the polarisation of the foil was (anti-) parallel to the allowed polarisation of the foil. Switching both the polarisation of the neutron and the magnetisation of the foil does not change the measured signal as can be seen by comparing the red and green or respectively purple and blue lines. The histograms are normalised to the maximal count per bin.

The region of interest for the ArCO₂ spectrum was ROI (128-900). The errors of the bin count are Poissonian.

8 measurements and 2 background measurements were performed in total. All permutations of detector polarisation and spin flipper settings were used to exclude any systematic effects. The recorded data showed the expected behaviour, only dependent on the polarisation of the neutrons relative to detector polarisation, see figure B.2.

The polarisation P is defined by the number of neutrons passing when spin is parallel n_p and when anti parallel n_s (i.e. when the neutrons should pass or be stopped):

$$P = \sqrt{\frac{n_p - n_s}{n_p + n_s}}. \quad (\text{B.2})$$

The square root follows from the fact that in this setup the polarisation is measured twice: first at the polariser right behind the chopper and at the detector. Both foils were coated simultaneously and thus have the same properties. The equation is only valid when the same total number of neutrons is sent onto the polariser. As the neutron flux might change at the beam line, it is essential to normalise for the incoming neutrons. This is done by determining the total neutron count for a high velocity, when both spin polarisations can pass the foil. For this, the peak of the spectrum is fitted for the neutron count c for the channel number n with the parameters a and the offset o :

$$c(n) = a(n - o)^2. \quad (\text{B.3})$$

The fitted parameter are shown in table B.3. As expected, the obtained offset is the same for both polarisation configurations.

The obtained polarisation curve can be seen in figure B.4. The data is fitted with the following function to obtain an analytical form:

$$P(v) = p - \exp(k(v + v_0)). \quad (\text{B.4})$$

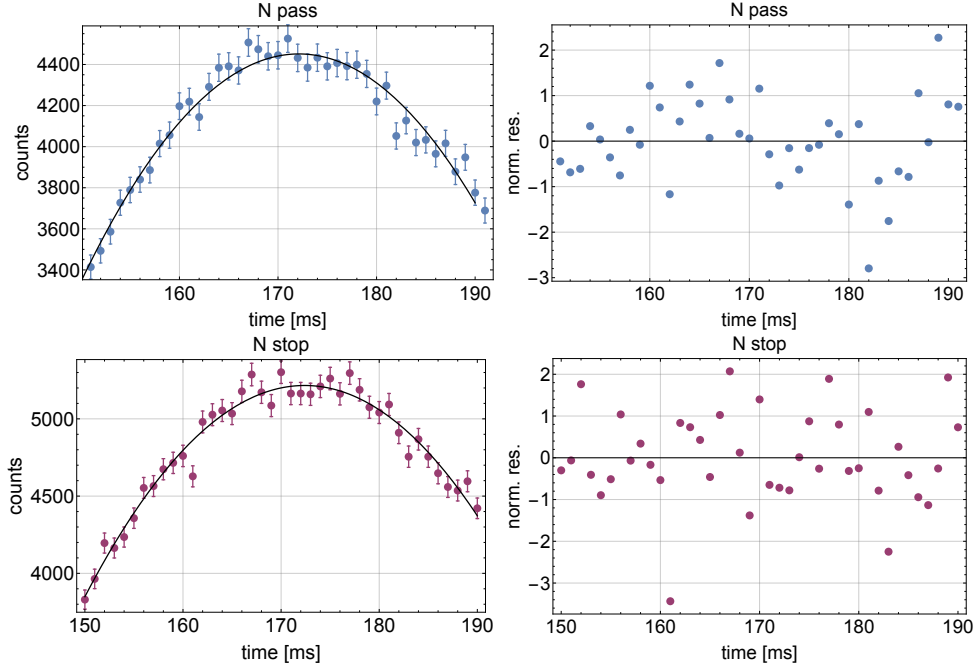


Figure B.3: Fitting of the maximum peak and their normalised residuals.

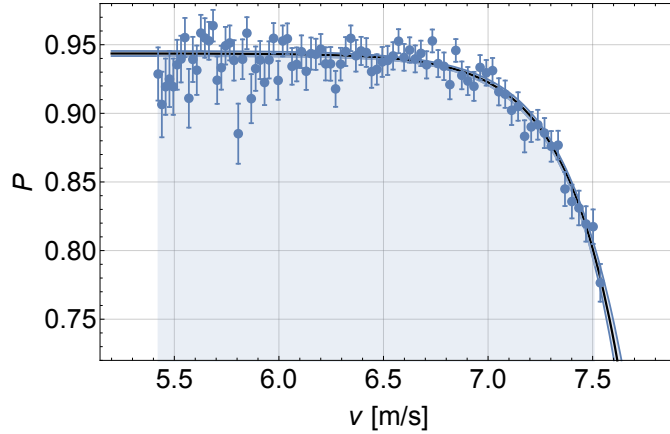


Figure B.4: The velocity dependency of the polariser. The velocity range used in the axion-like particle search are indicated by the shaded area. The analytical function derived by the fit is shown in black with error margin.

As the used velocity range used for the spin-dependent measurements was $5.42 \text{ m s}^{-1} < v_x < 7.51 \text{ m s}^{-1}$ the total polarisation for a uniform velocity distribution reads:

$$\int_{5.42 \text{ m/s}}^{7.51 \text{ m/s}} P(v) dv = 92.51 \%. \quad (\text{B.5})$$

Fit	Parameter	χ_{red}^2	pts	prob. [%]
Peak neutr. pass	$a = -2.267_{-0.078}^{+0.078} \text{ ch}^{-2}$ $c = 4451.3_{-15.3}^{+15.3}$ $o = 172.12_{-0.18}^{+0.19} \text{ ch}$	0.968	41	52.54
Peak neutr. stop	$a = -2.724_{-0.085}^{+0.085} \text{ ch}^{-2}$ $c = 5216.0_{-16.4}^{+16.4}$ $o = 172.40_{-0.18}^{+0.18} \text{ ch}$	1.288	41	11.03
Pol.	$v_0 = -8.01_{-0.04}^{+0.04} \text{ m/s}$ $k = 3.826_{-0.271}^{+0.289} \text{ s/m}$ $p = 0.944_{-0.002}^{+0.002}$	0.854	86	82.55

Table B.1: *Upper two rows:* Fit results for the normalisation. The peak height c is used to determine the incoming flux and is used as normalisation. The fitted parameter o is the peak position. It agrees for both neutron spin orientation sets. *Lower row:* The fit result for the velocity dependent polarisation curve. p is the maximum polarisation, v_0 and k describe the decline of the polarisation for higher velocities.

Appendix C

Glossary

Symbol	Meaning
Ψ	the total wave function of a neutron confined in a gravity potential
ψ_n	n -th eigenfunction of system without an additional boundary condition
ϕ_n	n -th eigenfunction of system with an additional boundary condition at height l
E_0	energy scale of a neutron confined in a gravity potential
z_0	length scale of a neutron confined in a gravity potential
t_0	time scale of a neutron confined in a gravity potential
E_n	n -th eigen energy of a neutron confined in a gravity potential
E'_n	n -th eigen energy of system with an additional boundary condition at height l

Meaning	Symbol	Value
speed of light	c	299 792 458 m s ⁻¹
inertial mass of the neutron	m_n	$1.674\,927\,351(74) \times 10^{-27}$ kg [Mohr et al., 2012]
reduced Planck constant	\hbar	1.054 571 726(47) J s
gravitational constant	G	$6.673\,84(80) \times 10^{-11}$ m ³ kg ⁻¹ s ⁻²
electron charge	e	$1.602\,176\,565(35) \times 10^{-19}$ C
mass of the Earth	M_{\oplus}	5.9737×10^{24} kg [Cox, 2000]
mass of the moon	M_{ζ}	7.3483×10^{22} kg [Cox, 2000]
unified atomic mass unit	u	$1.660\,538\,921(73) \times 10^{-27}$ kg
cosmological constant	Λ_0	≈ 2.4 meV [Planck Collaboration, 2014]
magnetic moment of the neutron	μ	-60.3077 neV T ⁻¹
local acceleration at PF2	g_{sp}	$9.805\,07(2)$ m/s ² [Weber, 1998]

Table C.1: Fundamental values used (from [Beringer et al., 2012], if not stated otherwise).

Bibliography

- [Abele, 2008] H. ABELE. The neutron. Its properties and basic interactions. *Progress in Particle and Nuclear Physics*, **60**(1):1, 2008. [cited at p. 10]
- [Abele et al., 2015] H. ABELE, A. IVANOV, T. JENKE, M. PITSCHMANN, & P. GELTENBORT. Gravity Resonance Spectroscopy and Einstein- Cartan Gravity. 2015. [cited at p. 5]
- [Abele et al., 2010] H. ABELE, T. JENKE, H. LEEB, & J. SCHMIEDMAYER. Ramseys method of separated oscillating fields and its application to gravitationally induced quantum phase shifts. *Physical Review D*, **81**(6):065019, 2010. [cited at p. 5, 10, 66]
- [Adelberger et al., 2009] E. ADELBERGER, J. GUNDLACH, B. HECKEL, S. HOEDL, & S. SCHLAMMINGER. Torsion balance experiments: A low-energy frontier of particle physics. *Progress in Particle and Nuclear Physics*, **62**(1):102, 2009. [cited at p. 62, 63]
- [Adelberger et al., 1990] E. G. ADELBERGER, B. R. HECKEL, G. SMITH, Y. SU, & H. E. SWANSON. Eötvös experiments, lunar ranging and the strong equivalence principle. *Nature*, **347**(6290):261, 1990. [cited at p. 2]
- [Airy, 1856] G. B. AIRY. Account of Pendulum Experiments Undertaken in the Harton Colliery, for the Purpose of Determining the Mean Density of the Earth. *Philosophical Transactions of the Royal Society of London*, **146**(January):297, 1856. [cited at p. 9]
- [Altarev et al., 2015] I. ALTAREV, M. BALES, D. H. BECK, T. CHUPP, K. FIERLINGER, P. FIERLINGER, F. KUCHLER, ET AL. A large-scale magnetic shield with 106 damping at millihertz frequencies. *Journal of Applied Physics*, **117**(18):183903, 2015. [cited at p. 8]
- [Amaro-Seoane et al., 2012] P. AMARO-SEOANE, S. AODUIA, S. BABAK, P. BINÉTRUY, E. BERTI, A. BOHÉ, C. CAPRINI, ET AL. Low-frequency gravitational-wave science with eLISA/NGO. *Classical and Quantum Gravity*, **29**(12):124016, 2012. [cited at p. 2]
- [Anghel et al., 2009] A. ANGHEL, F. ATCHISON, B. BLAU, B. VAN DEN BRANDT, M. DAUM, R. DOELLING, M. DUBS, ET AL. The PSI ultra-cold neutron source. *Nuclear Instruments and Methods in Physics Research, Section A: Accelerators, Spectrometers, Detectors and Associated Equipment*, **611**(2-3):272, 2009. [cited at p. 7]
- [Antoniadis et al., 2011] I. ANTONIADIS, S. BAESSLER, M. BÜCHNER, V. V. FEDOROV, S. HOEDL, A. LAMBRECHT, V. V. NESVIZHEVSKY, ET AL. Short-range fundamental forces. *Comptes Rendus Physique*, **12**(8):755, 2011. [cited at p. 58]
- [Arkani-Hamed et al., 1998] N. ARKANI-HAMED, S. DIMOPOULOS, & G. DVALI. The hierarchy problem and new dimensions at a millimeter. *Physics Letters B*, **429**(3-4):263, 1998. [cited at p. 57]
- [Arkani-Hamed et al., 1999] N. ARKANI-HAMED, S. DIMOPOULOS, & G. DVALI. Phenomenology, astrophysics, and cosmology of theories with submillimeter dimensions and TeV scale quantum gravity. *Physical Review D*, **59**(8):086004, 1999. [cited at p. 57]

- [Baker et al., 2011] C. BAKER, G. BAN, K. BODEK, M. BURGHOFF, Z. CHOWDHURI, M. DAUM, M. FERTL, ET AL. The search for the neutron electric dipole moment at the Paul Scherrer Institute. *Physics Procedia*, **17**:159, 2011. [cited at p. 8]
- [Baker et al., 2006] C. A. BAKER, D. D. DOYLE, P. GELTENBORT, K. GREEN, M. G. D. VAN DER GRINTEN, P. G. HARRIS, P. IAYDJIEV, ET AL. Improved Experimental Limit on the Electric Dipole Moment of the Neutron. *Physical Review Letters*, **97**(13):1, 2006. [cited at p. 8]
- [Bender et al., 1973] P. L. BENDER, D. G. CURRIE, S. K. POULTNEY, C. O. ALLEY, R. H. DICKE, D. T. WILKINSON, D. H. ECKHARDT, ET AL. The Lunar Laser Ranging Experiment. *Science (New York, N.Y.)*, **182**(4109):229, 1973. [cited at p. 2]
- [Beringer et al., 2012] J. BERINGER, J. F. ARGUIN, R. M. BARNETT, & K. COPIC. Review of Particle Physics. *Physical Review D*, **86**(1):010001, 2012. [cited at p. 8, 10, 79]
- [BICEP2/Keck and Planck Collaborations, 2015] BICEP2/KECK AND PLANCK COLLABORATIONS. Joint Analysis of BICEP2/ Keck Array and Planck Data. *Physical Review Letters*, **114**(10):1, 2015. [cited at p. 2]
- [Bittner, 2013] T. BITTNER. *Entwicklung eines Blendensystems zur Geschwindigkeitsselektion für das qBounce Experiment*. Diplomarbeit, Technische Universität Wien, 2013. [cited at p. 41]
- [Bod et al., 1991] L. BOD, E. FISCHBACH, G. MARX, & M. NÁRAY-ZIEGLER. One hundred years of the Eötvös experiment. *Acta Physica Hungarica*, **69**(3-4):335, 1991. [cited at p. 2]
- [Brax & Burrage, 2010] P. BRAX & C. BURRAGE. Chameleon induced atomic afterglow. *Physical Review D - Particles, Fields, Gravitation and Cosmology*, **82**:13, 2010. [cited at p. 62]
- [Brax & Burrage, 2011] P. BRAX & C. BURRAGE. Atomic precision tests and light scalar couplings. *Physical Review D - Particles, Fields, Gravitation and Cosmology*, **83**(3):1, 2011. [cited at p. 62, 63]
- [Brax & Pignol, 2011] P. BRAX & G. PIGNOL. Strongly Coupled Chameleons and the Neutronic Quantum Bouncer. *Physical Review Letters*, **107**(11):111301, 2011. [cited at p. 60]
- [Brax et al., 2013] P. BRAX, G. PIGNOL, & D. ROULIER. Probing strongly coupled chameleons with slow neutrons. *Physical Review D*, **88**(8):083004, 2013. [cited at p. 62]
- [Carroll, 2001] S. M. CARROLL. The Cosmological Constant. *Living Reviews in Relativity*, **4**(December 1999):50, 2001. [cited at p. 59]
- [Chiu et al., 2011] S. W. CHIU, T. KOVACHY, H. C. CHIEN, & M. A. KASEVICH. 102 k Large Area Atom Interferometers. *Physical Review Letters*, **107**(13):1, 2011. [cited at p. 3]
- [Chizhova et al., 2014] L. A. CHIZHOVA, S. ROTTER, T. JENKE, G. CRONENBERG, P. GELTENBORT, G. WAUTISCHER, H. FILTER, ET AL. Vectorial velocity filter for ultracold neutrons based on a surface-disordered mirror system. *Physical Review E*, **89**(3):032907, 2014. [cited at p. 20, 24]
- [Colella et al., 1975] R. COLELLA, A. OVERHAUSER, & S. WERNER. Observation of gravitationally induced quantum interference. *Physical Review Letters*, **34**(23):1472, 1975. [cited at p. 3, 4, 54]
- [Cox, 2000] A. N. COX (ed.). *Allen's Astrophysical Quantities*. Springer, New York, 2000. ISBN 978-0-387-95189-8. [cited at p. 79]
- [Decca et al., 2007] R. S. DECCA, D. LÓPEZ, E. FISCHBACH, G. L. KLIMCHITSKAYA, D. E. KRAUSE, & V. M. MOSTEPANENKO. Tests of new physics from precise measurements of the Casimir pressure between two gold-coated plates. *Physical Review D - Particles, Fields, Gravitation and Cosmology*, **75**(7):7, 2007. [cited at p. 58]
- [Dubbers & Schmidt, 2011] D. DUBBERS & M. G. SCHMIDT. The neutron and its role in cosmology and particle physics. *Reviews of Modern Physics*, **83**(4):1111, 2011. [cited at p. 8]
- [Durstberger-Rennhofer et al., 2011] K. DURSTBERGER-RENNHOFER, T. JENKE, & H. ABELE. Probing the neutrons electric neutrality with Ramsey spectroscopy of gravitational quantum states of ultracold neutrons. *Physical Review D*, **84**(3):5, 2011. [cited at p. 66]

-
- [Einstein, 1915] A. EINSTEIN. Die Feldgleichungen der Gravitation. *Preuss. Akad. Wiss. Berlin, Sitzungsber.*, pp. 844–847, 1915. [cited at p. 1]
- [Fellinger, 2012] J. FELLINGER. *Einrichten der Experimentieroberfläche des q-Bounce Experiments senkrecht zum Erdmittelpunkt*. Bachelor thesis, Technische Universität Wien, 2012. [cited at p. 30]
- [Fortier et al., 2007] T. FORTIER, N. ASHBY, J. BERGQUIST, M. DELANEY, S. DIDDAMS, T. HEAVNER, L. HOLLBERG, ET AL. Precision Atomic Spectroscopy for Improved Limits on Variation of the Fine Structure Constant and Local Position Invariance. *Physical Review Letters*, **98**(7):070801, 2007. [cited at p. 54]
- [Fox, 2006] M. FOX. *Quantum Optics*. Oxford University Press, Oxford, 2006. [cited at p. 13]
- [Frank et al., 2009] A. FRANK, P. GELTENBORT, M. JENTSCHHEL, G. KULIN, D. KUSTOV, V. NOSOV, & A. STREPETOV. New test of the weak equivalence principle for neutrons. *Nuclear Instruments and Methods in Physics Research Section A: Accelerators, Spectrometers, Detectors and Associated Equipment*, **611**(2-3):314, 2009. [cited at p. 3]
- [Geraci et al., 2008] A. GERACI, S. SMULLIN, D. WELD, J. CHIAVERINI, & A. KAPITULNIK. Improved constraints on non-Newtonian forces at 10 microns. *Physical Review D*, **78**(2):12, 2008. [cited at p. 58]
- [Gibbs, 1975] R. L. GIBBS. The quantum bouncer. *American Journal of Physics*, **43**(1):25, 1975. [cited at p. 8]
- [Giulini, 2012] D. GIULINI. Equivalence Principle, Quantum Mechanics, and Atom-Interferometric Tests. In *Quantum Field Theory and Gravity*, pp. 345–370. Springer Basel, Basel, 2012. doi:10.1007/978-3-0348-0043-3_{_}16. [cited at p. 54]
- [Golub et al., 1991] R. GOLUB, D. RICHARDSON, & S. K. LAMOREAUX. *Ultra-Cold Neutrons*. Inst. of Physics Pub., New York, 1991. ISBN 978-0750301152. [cited at p. 7, 74]
- [Greenberger, 1968] D. GREENBERGER. The role of equivalence in Quantum Mechanics. *Annals of Physics*, **47**(1):116, 1968. [cited at p. 3, 54]
- [Hamilton et al., 2015a] P. HAMILTON, M. JAFFE, J. M. BROWN, L. MAISENBACHER, B. ESTEY, & H. MÜLLER. Atom Interferometry in an Optical Cavity. *Physical Review Letters*, **114**(10):100405, 2015a. [cited at p. 3]
- [Hamilton et al., 2015b] P. HAMILTON, M. JAFFE, P. HASLINGER, Q. SIMMONS, H. MULLER, & J. KHOURY. Atom-interferometry constraints on dark energy. *Science*, **349**(6250):849, 2015b. [cited at p. 63]
- [Harry, 2010] G. M. HARRY. Advanced LIGO: the next generation of gravitational wave detectors. *Classical and Quantum Gravity*, **27**(8):084006, 2010. [cited at p. 2]
- [Herrmann et al., 2005] S. HERRMANN, A. SENGER, E. KOVALCHUK, H. MÜLLER, & A. PETERS. Test of the Isotropy of the Speed of Light Using a Continuously Rotating Optical Resonator. *Physical Review Letters*, **95**(15):150401, 2005. [cited at p. 54]
- [Iocco et al., 2015] F. IOCCO, M. PATO, & G. BERTONE. Evidence for dark matter in the inner Milky Way. *Nature Physics*, **11**(February):245, 2015. [cited at p. 1]
- [Ivanov et al., 2013] A. N. IVANOV, R. HÖLLWIESER, T. JENKE, M. WELLENZOHN, & H. ABELE. Influence of the chameleon field potential on transition frequencies of gravitationally bound quantum states of ultracold neutrons. *Physical Review D*, **87**(10):105013, 2013. [cited at p. 61]
- [Jenke, 2008] T. JENKE. *Weiterentwicklung eines Experiments zur Realisierung eines Quantum Bouncing Balls und Suche nach Extradimensionen der Raumzeit*. Diplomarbeit, Ruprecht-Karls-Universität Heidelberg, 2008. [cited at p. 18, 58]
- [Jenke, 2011] T. JENKE. *qBounce - vom Quantum Bouncer zur Gravitationsresonanzspektroskopie*. Ph.D. thesis, Technische Universität Wien, 2011. [cited at p. 13, 27, 35]
- [Jenke et al., 2014] T. JENKE, G. CRONENBERG, J. BURGDÖRFER, L. A. CHIZHOVA, P. GELTENBORT, A. N. IVANOV, T. LAUER, ET AL. Gravity Resonance Spectroscopy Constrains Dark Energy and Dark Matter Scenarios. *Physical Review Letters*, **112**(15):151105, 2014. [cited at p. 5, 10, 27, 57, 73]

- [Jenke et al., 2013] T. JENKE, G. CRONENBERG, H. FILTER, P. GELTENBORT, M. KLEIN, T. LAUER, K. MITSCH, ET AL. Ultracold neutron detectors based on 10B converters used in the qBounce experiments. *Nuclear Instruments and Methods in Physics Research Section A: Accelerators, Spectrometers, Detectors and Associated Equipment*, **732**:1, 2013. [cited at p. 25, 35, 74]
- [Jenke et al., 2012] T. JENKE, G. CRONENBERG, P. GELTENBORT, A. N. IVANOV, T. LAUER, T. LINS, U. SCHMIDT, ET AL. A quantized frequency reference in the short-ranged gravity potential and its application for dark matter and dark energy searches. p. 18, 2012. [cited at p. 62, 63]
- [Jenke et al., 2011] T. JENKE, P. GELTENBORT, H. LEMMEL, & H. ABELE. Realization of a gravity-resonance-spectroscopy technique. *Nature Physics*, **7**(6):468, 2011. [cited at p. 4, 10, 48]
- [Jenke et al., 2009] T. JENKE, D. STADLER, H. ABELE, & P. GELTENBORT. Q-BOUNCE - Experiments with quantum bouncing ultracold neutrons. *Nuclear Instruments and Methods in Physics Research Section A: Accelerators, Spectrometers, Detectors and Associated Equipment*, **611**(2-3):318, 2009. [cited at p. 55]
- [Jung, 2013] J. JUNG. *Aufbau und Betreuung des qBounce-Versuchsaufbaus*. Projektarbeit, Vienna University of Technology, 2013. [cited at p. 23, 41]
- [Kajari et al., 2010] E. KAJARI, N. L. HARSHMAN, E. M. RASEL, S. STENHOLM, G. SÜSSMANN, & W. P. SCHLEICH. Inertial and gravitational mass in quantum mechanics. *Applied Physics B*, **100**(1):43, 2010. [cited at p. 55]
- [Kapner et al., 2007] D. KAPNER, T. COOK, E. ADELBERGER, J. GUNDLACH, B. HECKEL, C. HOYLE, & H. SWANSON. Tests of the Gravitational Inverse-Square Law below the Dark-Energy Length Scale. *Physical Review Letters*, **98**(2):1, 2007. [cited at p. 57]
- [Khoury & Weltman, 2004] J. KHOURY & A. WELTMAN. Chameleon cosmology. *Physical Review D*, **69**(4):1, 2004. [cited at p. 60]
- [Klein, 2000] M. KLEIN. *Experimente zur Quantenmechanik mit ultrakalten Neutronen und Entwicklung eines neuen Detektors zum ortsaufgelosten Nachweis von thermischen Neutronen auf großen Flächen*. Ph.D. thesis, Ruprecht-Karls-Universität Heidelberg, 2000. [cited at p. 25]
- [Koester, 1976] L. KOESTER. Verification of the equivalence of gravitational and inertial mass for the neutron. *Physical Review D*, **14**(4):4, 1976. [cited at p. 3, 4, 54]
- [Lamoreaux, 1997] S. K. LAMOREAUX. Demonstration of the Casimir Force in the 0.6 to 6 μm Range. *Physical Review Letters*, **78**(1):5, 1997. [cited at p. 58]
- [Langhoff, 1971] P. W. LANGHOFF. Schrodinger Particle in a Gravitational Well. *American Journal of Physics*, **39**(8):954, 1971. [cited at p. 8]
- [Lemmel et al., 2015] H. LEMMEL, P. BRAX, A.N. IVANOV, T. JENKE, G. PIGNOL, M. PITSCHMANN, T. POTOVAR, ET AL. Neutron interferometry constrains dark energy chameleon fields. *Physics Letters B*, **743**:310, 2015. [cited at p. 62, 63]
- [Lins, 2011] T. LINS. *Quantenzustände im Gravitationsfeld der Erde*. Diplomarbeit, Technische Universität München, 2011. [cited at p. 31]
- [Lushchikov & Frank, 1978] V. I. LUSCHIKOV & A. I. FRANK. Quantum effects occuring when ultracold neutrons are stored on a plane. *JETP Lett*, **28**(9), 1978. [cited at p. 8]
- [Lushchikov et al., 1969] V. I. LUSHCHIKOV, Y. N. POKOTILOVSKII, A. V. STRELKOV, & F. L. SHAPIRO. Observation of Ultracold Neutrons. *JETP Letters*, **9**(1):23, 1969. [cited at p. 7]
- [Marson & Faller, 1986] I. MARSON & J. E. FALLER. g-the acceleration of gravity: its measurement and its importance. *Journal of Physics E: Scientific Instruments*, **19**(1):22, 1986. [cited at p. 56]
- [Mohr et al., 2012] P. J. MOHR, B. N. TAYLOR, & D. B. NEWELL. CODATA Recommended Values of the Fundamental Physical Constants: 2010. *Journal of Physical and Chemical Reference Data*, **41**(4):043109, 2012. [cited at p. 56, 57, 79]

-
- [Nesvizhevsky et al., 2002] V. V. NESVIZHEVSKY, H. G. BÖRNER, A. K. PETUKHOV, H. ABELE, S. BAESSLER, F. J. RUESS, T. STÖFERLE, ET AL. Quantum states of neutrons in the Earth's gravitational field. *Nature*, **415**(6869):297, 2002. [cited at p. 9, 24, 25]
- [Nico et al., 2005] J. S. NICO, M. S. DEWEY, D. M. GILLIAM, F. E. WIETFELDT, X. FEI, W. M. SNOW, G. L. GREENE, ET AL. Measurement of the neutron lifetime by counting trapped protons in a cold neutron beam. *Physical Review C*, **71**(5):055502, 2005. [cited at p. 8]
- [Panda & Panda, 2001] S. PANDA & B. K. PANDA. Analytic methods for field induced tunneling in quantum wells with arbitrary potential profiles. *Pramana*, **56**(6):809, 2001. [cited at p. 9]
- [Pendlebury et al., 2015] J. M. PENDLEBURY, S. AFACH, N. J. AYRES, C. A. BAKER, G. BAN, G. BISON, K. BODEK, ET AL. Revised experimental upper limit on the electric dipole moment of the neutron. *Physical Review D*, **92**(9):092003, 2015. [cited at p. 8]
- [Peters et al., 1999] A. PETERS, K. CHUNG, & S. CHU. Measurement of gravitational acceleration by dropping atoms. *Nature*, pp. 849–852, 1999. [cited at p. 3]
- [Pichlmaier et al., 2010] A. PICHLMAIER, V. VARLAMOV, K. SCHRECKENBACH, & P. GELTENBORT. Neutron lifetime measurement with the UCN trap-in-trap MAMBO II. *Physics Letters, Section B: Nuclear, Elementary Particle and High-Energy Physics*, **693**(3):221, 2010. [cited at p. 8]
- [Planck Collaboration, 2014] PLANCK COLLABORATION. Planck 2013 results. XVI. Cosmological parameters. *Astronomy & Astrophysics*, **16**:69, 2014. [cited at p. 2, 79]
- [Rabi et al., 1939] I. RABI, S. MILLMAN, P. KUSCH, & J. ZACHARIAS. The Molecular Beam Resonance Method for Measuring Nuclear Magnetic Moments. The Magnetic Moments of Li63, Li73 and F199. *Physical Review*, **55**(6):526, 1939. [cited at p. 10, 11]
- [Rabinowitz, 2007] M. RABINOWITZ. Falling Bodies: the Obvious, the Subtle, and the Wrong. **31**:27, 2007. [cited at p. 53]
- [Ramsey, 1956] N. F. RAMSEY. *Molecular Beams*. Clarendon Press, 1956. [cited at p. 66]
- [Saul, 2011] H. SAUL. *Weiterentwicklung des Detektor- und Auslesekonzepts für das Gravitationsexperiment qBounce*. Diplomarbeit, Technische Universität München, 2011. [cited at p. 25, 35]
- [Schlamminger et al., 2008] S. SCHLAMMINGER, K.-Y. CHOI, T. WAGNER, J. GUNDLACH, & E. ADELBERGER. Test of the Equivalence Principle Using a Rotating Torsion Balance. *Physical Review Letters*, **100**(4):041101, 2008. [cited at p. 2, 55, 56]
- [Schlippert et al., 2014] D. SCHLIPPERT, J. HARTWIG, H. ALBERS, L. L. RICHARDSON, C. SCHUBERT, A. ROURA, W. P. SCHLEICH, ET AL. Quantum Test of the Universality of Free Fall. *Physical Review Letters*, **112**(20):203002, 2014. [cited at p. 3]
- [Schmiedmayer, 1989] J. SCHMIEDMAYER. The equivalence of the gravitational and inertial mass of the neutron. *Nuclear Instruments and Methods in Physics Research Section A: Accelerators, Spectrometers, Detectors and Associated Equipment*, **284**(1):59, 1989. [cited at p. 54]
- [Smullin et al., 2005] S. J. SMULLIN, A. A. GERACI, D. M. WELD, J. CHIAVERINI, S. HOLMES, & A. KAPITULNIK. Constraints on Yukawa-type deviations from Newtonian gravity at 20 microns. *Physical Review D - Particles, Fields, Gravitation and Cosmology*, **72**:1, 2005. [cited at p. 58]
- [Stadler, 2009] D. STADLER. *Dynamik ultrakalter Neutronen im Gravitationsfeld der Erde*. Diplomarbeit, Universität Heidelberg, 2009. [cited at p. 25]
- [Steffen et al., 2010] J. H. STEFFEN, A. UPADHYE, A. BAUMBAUGH, A. S. CHOU, P. O. MAZUR, R. TOMLIN, A. WELTMAN, ET AL. Laboratory Constraints on Chameleon Dark Energy and Power-Law Fields. *Physical Review Letters*, **105**(26):261803, 2010. [cited at p. 63]
- [Steyerl, 1969] A. STEYERL. Measurements of total cross sections for very slow neutrons with velocities from 100 m/sec to 5 m/sec. *Physics Letters B*, **29**(1):33, 1969. [cited at p. 7]
- [Steyerl, 1975] A. STEYERL. A neutron turbine as an efficient source of ultracold neutrons. *Nuclear Instruments and Methods*, **125**(3):461, 1975. [cited at p. 7]
-

- [Stubbs, 1993] C. W. STUBBS. Experimental limits on any long range nongravitational interaction between dark matter and ordinary matter. *Physical Review Letters*, **70**(2):119, 1993. [cited at p. 44]
- [Sushkov et al., 2011] A. O. SUSHKOV, W. J. KIM, D. A. R. DALVIT, & S. K. LAMOREAUX. New Experimental Limits on Non-Newtonian Forces in the Micrometer Range. *Physical Review Letters*, **107**(17):171101, 2011. [cited at p. 58]
- [Thalhammer, 2013] M. THALHAMMER. *Optimierung der Detektorsignalverarbeitung des Gravitationsexperiments qBounce*. Diplomarbeit, Vienna University of Technology, 2013. [cited at p. 36]
- [Trimble, 1987] V. TRIMBLE. Existence And Nature Of Dark Matter In The Universe. 1987. doi: 10.1146/annurev.astro.25.1.425. [cited at p. 1]
- [Uzan, 2011] J.-P. UZAN. Varying Constants, Gravitation and Cosmology. *Living Reviews in Relativity*, **14**, 2011. [cited at p. 54]
- [Vallée & Soares, 2004] O. VALLÉE & M. SOARES. *Airy Functions and Applications to Physics*. Imperial College Press, 2004. ISBN 978-1860944789. doi:10.1142/9781848165502. [cited at p. 69]
- [Vessot et al., 1980] R. VESSOT, M. LEVINE, E. MATTISON, E. BLOMBERG, T. HOFFMAN, G. NYSTROM, B. FARREL, ET AL. Test of Relativistic Gravitation with a Space-Borne Hydrogen Maser. *Physical Review Letters*, **45**(26):2081, 1980. [cited at p. 54]
- [Wautischer, 2015] G. WAUTISCHER. *Realisation of quantum transport measurements with UCNs within the qBounce project*. Diplomarbeit, Vienna University of Technology, 2015. [cited at p. 23]
- [Weber, 1998] M. WEBER. *Gravitation in der Interferometrie mit kalten Neutronen*. Ph.D. thesis, Univ. Innsbruck, 1998. [cited at p. 55, 79]
- [Wietfeldt & Greene, 2011] F. E. WIETFELDT & G. L. GREENE. Colloquium: The neutron lifetime. *Reviews of Modern Physics*, **83**(4):1173, 2011. [cited at p. 8]
- [Williams et al., 2012] J. G. WILLIAMS, S. G. TURYSHEV, & D. H. BOGGS. Lunar laser ranging tests of the equivalence principle. *Classical and Quantum Gravity*, **29**(18):184004, 2012. [cited at p. 2]
- [Zimmer et al., 2011] O. ZIMMER, F. PIEGSA, & S. IVANOV. Superthermal Source of Ultracold Neutrons for Fundamental Physics Experiments. *Physical Review Letters*, **107**(13):1, 2011. [cited at p. 7]
- [van der Zouw et al., 2000] G. VAN DER ZOUW, M. WEBER, J. FELBER, R. GÄHLER, P. GELTENBORT, & A. ZEILINGER. AharonovBohm and gravity experiments with the very-cold-neutron interferometer. *Nuclear Instruments and Methods in Physics Research Section A: Accelerators, Spectrometers, Detectors and Associated Equipment*, **440**(3):568, 2000. [cited at p. 54]
- [Zwicky, 1933] F. ZWICKY. Die Rotverschiebung von extragalaktischen Nebeln. *Helv. Phys. Acta*, **II**(6):110, 1933. [cited at p. 1]

Acknowledgements

This thesis would have been impossible without the help of many people. I want to express my gratitude and warmest thanks to

Prof. Hartmut Abele for giving me the possibility to pursue this intriguing experiment and to study gravitation with quantum objects. I am grateful for his guidance, continuous support and advice which allowed this thesis.

Prof. Klaus Kirch for accepting to be the second referee.

Tobias Jenke for continued help as well as his experience and insight regarding the q BOUNCE experiment.

Peter Geltenbort for his support both inside and outside the ILL and introducing me to the ways of the PF2.

Dr. Ulrich Schmidt, Dr. Thorsten Lauer, Prof. Rotter and Larisa Chizhova as our collaborators.

Mario Pitschmann for many insightful discussions and comments.

Hanno Filter and Martin Thalhammer for their support and comradeship especially during the beam times.

Herbert Hartmann as well as Roman Gergen, Miklos Horvath and the mechanical workshop who always managed to realise the most impossible ideas when they were, as always, most urgent.

Thomas Brenner and his crucial emergency fixes which were always needed in an untimely manner.

the many students who contributed with their parts and efforts to the experiment.

Tobias Rechberger in general and especially for his comments.

Jaqueline Erhart and many other colleagues at the Atominstitut, who contributed to a nice environment.

Thomas Haschka, Stefan Heiss and Wernfried Mayr-Schmölzer for your comments.

And of course, I also owe many thanks to my parents for their continuous support!

List of Figures

1.1 Gravity experiments with neutrons	4
2.1 Gravity states	9
2.2 Original Rabi setup	11
2.3 The Rabi-like setup	11
2.4 Wave functions between two mirrors	12
2.5 Applicability of 2-level assumption	13
3.1 Velocity selection setup	18
3.2 Slit height dependence on velocity selection	19
3.3 Measurement for velocity spectrum	21
3.4 Comparison of velocity spectra	22
3.5 Velocity attributed smearing of transmission signal	22
3.6 Profile and waviness of neutron scatterer	23
3.7 Scanning electron microscope picture of the rough surface	24
3.8 Dependence of the transmission rate on the slit height.	25
3.9 Track detector L9	26
3.10 Stability during track detector measurement L9	26
3.11 Spatial probability distribution of track measurement	27
3.12 Position of capacitive sensors	28
3.13 Matrix elements with step	29
3.14 Alignment stability	30
3.15 Alignment sensitivity	31
3.16 Oscillation as seen by capacitive sensors	32
3.17 Measuring oscillation strength and phase	33
3.18 Measured frequency spectrum	33
3.19 Measured amplitude	34
3.20 Beam monitor and detector spectra	36
3.21 Signal-to-noise ratio for beam monitor and detector	37
3.22 Beam monitor and detector spectra comparisons	37
3.23 Time stability of beam monitor	38
3.24 (Corrected) Beam monitor (background) rate over time	38
3.25 Linearity of beam monitor signal	39

3.26	Detector background signal	39
3.27	Vacuum chamber	40
3.28	Magnetic field measurements	42
3.29	Null rate stability	44
4.1	χ^2 -environment of parameters	49
4.2	Correlation of fit parameters	49
4.3	Overview of measurement points	50
5.1	Gravitational mass of the neutron	57
5.2	Yukawa layout	58
5.3	Correlations of fit parameters for Yukawa potential	59
5.4	Yukawa exclusion plot	60
5.5	The effective chameleon potential	61
5.6	Correlations of fit parameters for chameleon potential	61
5.7	Chameleon exclusion plot	62
A.1	Airy functions	69
A.2	Energy solutions with additional boundary condition	71
B.1	Polariser characterisation setup	74
B.2	TOF signal for polarising foil	75
B.3	Fitting of the maximum peak and their normalised residuals.	76
B.4	Velocity dependency of polariser	76

List of Tables

1.1	Accessible parameters of GRS	6
2.1	Properties of UCNs	8
3.1	Parameters of the setup used during beam time <i>3-14-305</i>	21
3.2	Results of the track detector analysis	27
3.3	Systematic effects	44
3.4	Compatibility of time-dependent corrections	46
4.1	Fit parameters	48
4.2	Compatibility of fit models	51
5.1	Overlap with Yukawa-like potential	59
5.2	Limits on a Yukawa-like force	59
5.3	Limits on the chameleon field	63
B.1	Polarisation fit results	77
C.1	Fundamental values	79

Lebenslauf

Zur Person:

Name: Gunther Cronenberg
Adresse: Alpenlandstraße 2, 2380 Perchtoldsdorf
Telefon: +43 699 17131912
E-Mail: gunther@cronenberg.cc
Geboren: 31.08.1983 in Wien
Familienstand: ledig
Nationalität: Österreich

Werdegang:

seit 04/2010	Doktorarbeit am Atominstitut TU Wien
09/2009	Diplom in Technischer Physik der Technischen Universität Wien
10/2002-09/2009	Studium Technische Physik an der Technischen Universität Wien
06/2007-08/2007	Mitarbeit am ATLAS Projekt, CERN als Summer Student
08/2004-06/2005	Erasmus Auslandsjahr an der Uppsala University, Schweden
02/2001	Matura am BRG Perchtoldsdorf, Österreich

Publikationen:

7. T. Jenke, [G. Cronenberg](#), J. Burgdörfer, L.A. Chizhova, P. Geltenbort, A.N. Ivanov, T. Lauer, T. Lins, S. Rotter, H. Saul, U. Schmidt and H. Abele, *Phys. Rev. Lett.* **112**, 151105 (2014)
6. L. A. Chizhova, S. Rotter, T. Jenke, [G. Cronenberg](#), P. Geltenbort, G. Wautischer, H. Filter, H. Abele, and J. Burgdörfer, *Phys. Rev. E* **89**, 032907 (2014)
5. T. Jenke, [G. Cronenberg](#), H. Filter, P. Geltenbort, M. Klein, Th. Lauer, K. Mitsch, H. Saul, D. Seiler, D. Stadler, M. Thalhammer and H. Abele, *Nucl. Instr. and Meth. A* **732**, 1-8 (2013)
4. [G. Cronenberg](#), K. Durstberger-Rennhofer, P. Geltenbort, T. Jenke, H. Lemmel and H. Abele, *Journal of Physics: Conference Series*, **340**, 012045 (2012)
3. H. Abele, [G. Cronenberg](#), P. Geltenbort, T. Jenke, T. Lins, H. Saul, *Physics Procedia* **17**, 4-9 (2011)
2. St. Barz, [G. Cronenberg](#), A. Zeilinger, Ph. Walther, *Nature Photonics* **4**, 553-556 (2010)
1. R. Prevedel, [G. Cronenberg](#), M. S. Tame, M. Paternostro, P. Walther, M. S. Kim and A. Zeilinger, *Phys. Rev. Lett.* **103**, 020503 (2009)

Diplomarbeit: G. Cronenberg, *Experimental realisation and investigation of a six-photon symmetric Dicke state*, Technische Universität Wien (2009)